A&A 539, A48 (2012)
DOI: 10.1051/0004-6361/201117562

Astronomy & Astrophysics

The optical-UV spectral energy distribution of the unabsorbed AGN population in the *XMM-Newton* Bright Serendipitous Survey⋆,⋆⋆

E. Marchese[1], R. Della Ceca[1], A. Caccianiga[1], P. Severgnini[1], A. Corral[1], and R. Fanali[2]

[1] INAF-Osservatorio Astronomico di Brera, via Brera 28, 20121 Milano, Italy
e-mail: [elena.marchese;roberto.dellaceca]@brera.inaf.it
[2] Università Milano Bicocca, Dipartimento di Fisica G. Occhialini, Piazza della Scienza 3, 20126 Milano, Italy

Received 24 June 2011 / Accepted 17 November 2011

ABSTRACT

Context. Active galactic nuclei (AGN) emit radiation over a wide range of wavelengths, with a peak of emission in the far-UV region of the electromagnetic spectrum, a spectral region that is historically difficult to observe.
Aims. Using optical, GALEX UV, and *XMM-Newton* data we derive the spectral energy distribution (SED) from the optical/UV to X-ray regime of a sizeable sample of AGN. The principal motivation is to investigate the relationship between the optical/UV emission and the X-ray emission and provide bolometric corrections to the hard X-ray (2–10 keV) energy range, $k_{\rm bol}$, the latter being a fundamental parameter in current physical cosmology.
Methods. We construct and study the X-ray to optical SED of a sample of 195 X-ray selected Type 1 AGN belonging to the *XMM-Newton* bright serendipitous survey (XBS). The optical-UV luminosity was computed using data from the Sloan Digital Sky Survey (SDSS), from our own dedicated optical spectroscopy and the satellite GALaxy evolution EXplorer (GALEX), while the X-ray luminosity was computed using *XMM-Newton* data. Because it covers a wide range of redshift ($0.03 < z \lesssim 2.2$), X-ray luminosities ($41.8 < \log L_{[2-10]\ \rm keV} < 45.5$ erg/s) and because it is composed of "bright objects", this sample is ideal for this kind of investigation.
Results. We confirm a highly significant correlation between the accretion disc luminosity $L_{\rm disc}$ and the hard X-ray luminosity $L_{[2-10]\ \rm keV}$, in the form $L_{\rm disc} \propto L^{\beta}_{[2-10]\ \rm keV}$, where $\beta = 1.18 \pm 0.05$. We find a very shallow dependence of $k_{\rm bol}$ on the X-ray luminosity with respect to the broad distribution of values of $k_{\rm bol}$. We find a correlation between $k_{\rm bol}$ and the hard X-ray photon index $\Gamma_{2-10\ \rm keV}$ and a tight correlation between the optical-to-X-ray spectral index $\alpha_{\rm ox}$ and $k_{\rm bol}$, so we conclude that both $\Gamma_{2-10\ \rm keV}$ and $\alpha_{\rm ox}$ can be used as a proxy for $k_{\rm bol}$.

Key words. galaxies: active – galaxies: nuclei – accretion, accretion disks – cosmology: observations – methods: statistical

1. Introduction

A large fraction of the active galactic nuclei (AGN) bolometric luminosity is emitted in a strong, broad feature that begins to dominate the spectral energy distribution (SED) at the bluest optical wavelengths, and appears to extend short-wards of the current limits of UV satellite data (∼100 Å). This feature of the continuum, also known as the Big Blue Bump (Sanders et al. 1989), is most likely thermal emission arising from a geometrically thin, optically thick accretion disc (Shields 1978; Malkan & Sargent 1982; Ward et al. 1987). Another large fraction of the total luminosity in AGN is also emitted in the X-ray band, which is more likely arising from the inverse Compton scattering of the disc's photons by a corona of hot plasma surrounding the central regions of the disc, therefore X-ray and optical/UV observations are critical probes of the physics of the innermost regions of AGN, and investigating the relationship between the UV and X-ray emission is an important step towards better understanding the physics involved. Indeed the study of the correlation between X-ray and UV luminosities has in the past been the subject of many works on optically or X-ray selected samples of AGN (see Sect. 5).

In this paper we investigate the SEDs of a sample of 195 AGNs belonging to the *XMM-Newton* Bright Serendipitous Survey (XBS, Della Ceca et al. 2001) having UV observations from the satellite GALaxy evolution EXplorer (GALEX), optical magnitudes from the Sloan Digital Sky Survey (SDSS, complemented with optical data reported in Caccianiga et al. 2008) and X-ray observations from *XMM-Newton* (see Corral et al. 2011, hereafter referred as C11). The main goals of this work are:

a) to derive accretion disc luminosities for a significant and representative sample of AGN;
b) to investigate the correlations between the accretion disc and the X-ray luminosity;
c) to evaluate the bolometric luminosity (computed as the contribution of X-ray, UV and optical emission) and thus the bolometric correction to the hard X-ray (2–10 keV), defined as

$$k_{\rm bol} = \frac{L_{\rm bol}}{L_{[2-10]\ \rm keV}} \quad (1)$$

for a sample of AGN spanning a wide range in X-ray luminosities and redshifts. We stress that the infrared emission is not taken into account in the computation of the bolometric luminosity, since it is known to be re-processed emission

⋆ The *XMM-Newton* Bright Serendipitous Survey is part of the follow-up program being conducted by the *XMM-Newton* Survey Science Centre (SSC), http://xmmssc-www.star.le.ac.uk/
⋆⋆ Table 2 and Appendix A are available in electronic form at http://www.aanda.org

mainly from the ultraviolet (see Antonucci et al. 1993); indeed its inclusion would mean counting part of the emission twice, overestimating the derived bolometric luminosities.

The paper is organised as follows: in Sect. 2 we discuss the sample selection and the procedure used in cross-matching the sources in the XBS database with the GALEX and SDSS catalogues; Sect. 3 covers the construction of reliable SEDs for each source in the sample, taking into account intrinsic extinction and host galaxy contamination to the observed emission, as well as the emission lines contribution and absorption from Lyman α systems along the line of sight. In Sect. 4 we describe the results obtained in this work, focusing on the correlation analysis between the accretion disc luminosity and the X-ray luminosity, and the relation between bolometric correction and the X-ray luminosity. Our results are discussed within the context of previous works in Sect. 5 while in Sect. 6 summary and conclusions are presented. As done for other papers on the XBS survey we assume here the cosmological model $H_0 = 65\ \mathrm{km\,s^{-1}\,Mpc^{-1}}$, $\Omega_\lambda = 0.7$ and $\Omega_\mathrm{M} = 0.3$ throughout this paper.

2. Data sources

2.1. XMM-Newton bright serendipitous survey

The *XMM-Newton* bright serendipitous survey (XBS survey) is a wide-angle (∼28 sq. deg) high Galactic latitude ($|b| > 20°$) survey based on the *XMM-Newton* archival data. It is composed of two flux-limited serendipitous samples of X-ray selected sources: the XMM bright source sample (BSS, 0.5–4.5 keV band, 389 sources) and the XMM Hard bright source sample (HBSS, 4.5–7.5 keV band, 67 sources, with 56 sources in common with the BSS sample), having a flux limit of $\sim 7 \times 10^{-14}$ erg cm^{-2} s^{-1} in both energy selection bands. The details on the *XMM-Newton* fields selection strategy and the source selection criteria of the XMM BSS and HBSS samples are discussed in Della Ceca et al. (2004) and Della Ceca et al. (2008).

To date, the spectroscopic identification level has reached 93% and 97% for the BSS and the HBSS samples, respectively. The current classification of the XBS sample is as follows: 305 AGN (including 5 BL Lacs), 8 clusters of galaxies, 2 normal galaxies and 58 X-ray emitting stars (Caccianiga et al. 2008; Corral et al. 2011). The large majority of the still unidentified objects are expected to be absorbed AGN and BL Lac objects, so the sample of Type 1 AGN in the XBS can be considered complete at a confidence level approaching 100%. The analysis of the optical data, along with the relevant classification scheme and the optical properties of the extragalactic sources are presented in Caccianiga et al. (2007) and Caccianiga et al. (2008); the optical and X-ray properties of the galactic population are discussed in Lopez-Santiago et al. (2007).

The availability of good *XMM-Newton* data for the sources in the XBS sample, spanning the energy range between ∼0.3 and ∼10 keV, allowed us to perform a reliable X-ray spectral analysis for almost every AGN of the sample. The X-ray spectral analysis of the complete XBS AGN sample is presented in C11, which provide reliable X-ray photon indices, intrinsic column densities N_H, and X-ray luminosities, which are necessary to derive bolometric luminosities.

The following work is focused on Type 1 AGN, in order to limit uncertainties due to obscuration in the determination of the intrinsic SED shape. Furthermore, in the source selection, we applied a cut in intrinsic column density N_H, selecting only Type 1 AGN with $N_\mathrm{H} < 4 \times 10^{21}$ cm^{-2}, resulting in a sample of 262 sources (7 AGN have been excluded). From this sample we excluded 14 sources, classified as radio loud AGN (Galbiati et al. 2005), because we do not know the orientation of the relativistic jet respect to the line of sight, and thus we can not quantify its contamination on the X-ray observed spectrum (Zamorani et al. 1981; Wilkes & Elvis 1987; Galbiati et al. 2005). We note that selecting X-ray unabsorbed ($N_\mathrm{H} < 4 \times 10^{21}$ cm^{-2}) AGN also mitigate the possible "contamination" due to broad absorption line quasars (BALQSOs). Indeed BALQSOs seem to be characterised by the same intrinsic underlying X-ray continuum as the majority of the AGN population but their X-ray emission is often depressed by large amounts of intrinsic absorption (Streblyanska et al. 2010; Giustini et al. 2008; Gallagher et al. 2006). An X-ray to optical investigation of optically selected samples of Type 1 AGN without taking into account this contamination could lead to misleading results, since BALQSOs can cause an "artificial" steepening of the optical to X-ray correlation. To our knowledge there are no BALQSOs in our Type 1 AGN sample.

Thus the starting sample of our analysis is composed of 248 X-ray selected Type 1 AGN. We remark that the exclusion of obscured sources from our analysis does not necessarily mean that the conclusions we will outline further on are valid for unobscured sources only. Our results are still applicable to obscured AGNs if the obscuration is a line-of-sight orientation effect and does not affect the emission process at work in AGN.

2.2. Cross correlation with GALEX

The GALEX satellite is performing the first large-scale UV imaging survey (Martin et al. 2005; Morrisey et al. 2007). Most images are taken simultaneously in two broad bands, the near UV (NUV, ∼1770–2850 Å) and the far UV (FUV, ∼1350–1780 Å) at a resolution of ∼5″ full width at half maximum (FWHM). Three nested GALEX imaging surveys have been defined: the All-Sky Survey (AIS) expected to cover a large fraction (∼85%) of the high Galactic latitude ($|b| > 20°$) sky to $m_\mathrm{AB} \sim 21$, the Medium Imaging Survey (MIS) reaching $m_\mathrm{AB} \sim 23$ on 1000 deg^2, and the Deep Imaging Survey (DIS) extending to $m_\mathrm{AB} \sim 25$ on 80 deg^2. These main surveys are complemented by guest investigator programs.

Here we used the GALEX data from the officially distributed Data Release 4 (GR4), which has been homogeneously reduced and analysed by a dedicated software pipeline. A previous version of this pipeline used for the earlier GR3 data release is described in detail by Morrisey et al. (2007). For details about the changes between GR3 and GR4 and on the GALEX mission see respectively `http://galex.stsci.edu/GR4/` and `http://www.galex.caltech.edu/`.

2.2.1. GALEX detections

The cross correlation of the 248 Type 1 XBS AGN with the GALEX catalogue GR4 was performed by using the coordinates of the optical counterparts of the X-ray sources (reported in Caccianiga et al. 2008), with an impact parameter of 2.6″. This latter value was derived by Trammell et al. (2007) cross-correlating a sample of 6371 quasar from the SDSS with GALEX; they find that 99% of the matches is recovered with a search radius of 2.6″.

The cross-correlation produced (multiple or single) matches for 182 X-ray sources. We now describe how these matches were analysed. In the case of multiple matches (115 X-ray

sources) the duplicates were removed with the following procedure. If two GALEX sources were within 2.6″, but had the same "photoextractid" (i.e. they were both from the same observation) they were considered as two independent sources. In these cases (6 matches: XBSJ003418.9-115940, XBSJ012000.0-110429, XBSJ120359.1+443715, XBSJ120413.7+443149, XBSJ141809.1+250040, XBSJ163309.8+571039) the brightest source was selected as the best candidate to be the counterpart of the XBS source. Otherwise, if the multiple matches were from different observations, they were assumed to be multiple observations of the same source. In these cases the observation with the longest exposure time was retained. In the cases of almost equal exposure times we chose the observation where the source was closer to the centre of the field of view (that is the source with the smallest "fov-radius" from the "photoobjall" table), as generally the photometric quality is better in the central part of the field (Bianchi et al. 2011). All the selected sources, with the exception of two (XBSJ210355.3-121858, XBSJ165406.6+142123) have photometric errors (based on Poissonian source counts statistics, see also Sect. 3.3.1) on the UV magnitudes lower than 0.5 mag, in agreement with the selection procedure used by Bianchi et al. (2011). The two exceptions reported above, having respectively errors on NUV magnitudes of 0.56 mag and 0.58 mag, were still considered in our analysis.

From this sample of 182 Type 1 AGN we excluded two sources (XBSJ031851.9-441815 and XBSJ062134.8-643150) from the analysis, due to huge (up to a factor 1000) uncertainties in the estimate of the UV-optical fluxes, once the corrections discussed in Sect. 3 were taken into account. This procedure allowed us to define 180 X-ray/UV matches, from the original sample of 248 AGN; about 98% of the sources have at least a NUV detection, ∼2% were detected in the FUV band only, and about 75% of these sources were detected both in the NUV and in the FUV band.

In order to estimate the reliability of these matches we computed the expected number of random matches within 2.6″. This was done by performing the same cross-correlation after shifting the X-ray catalogue (along the right ascension and the declination) so that only chance coincidences are expected. To account for the non-uniform distribution of the sources in the sky we repeated several times the cross-correlation with different offsets and computed the average number of random sources found in each cross-correlation. Thus we derived that the probability of finding a GALEX UV spurious source within 2.6″ is 0.015, which correspond to ∼4 chance matches over the original sample of 248 sources.

2.2.2. Upper limits on GALEX fluxes

In this section we will discuss how the remaining 66 sources (for which we do not have GALEX photometric data) were treated. Forty six of these 66 sources (∼18.5% of the original sample of 248 sources) do not fall in the area of sky covered by GALEX (Data Release 4), thus the lack of UV data does not depend on the properties of the sources in this sub-sample. It is worth noting that, as the sources contained in the XBS catalogue have a serendipitous distribution in the sky (at $|b| > 20°$), we expect that a fraction of them will be "not covered" with GALEX data since the AIS survey is not covering the whole sky. Indeed, the total sky area at $|b| > 20°$ covered from AIS (GALEX DR4) is ∼23 000 square degrees (Karl Forster, mission planner, private communication), i.e. ∼85% of the sky at $|b| > 20°$. Therefore the fact that 18.5% of the original sample of sources is not covered by GALEX is fully consistent with the "missing" GALEX coverage of the $|b| > 20°$ sky (∼15%).

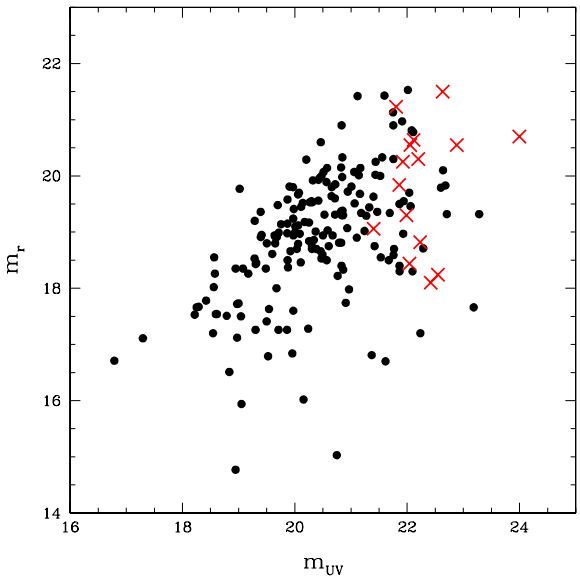

Fig. 1. Distribution in the $m_{UV} - m_r$ plane of the final sample of Type 1 AGN analysed. The red crosses represent the sources with UV upper limits, the black circles are the sources detected by GALEX.

The remaining 20 sources are indeed located in sky regions covered by GALEX observations. A visual inspection of the regions near these sources lead to the following conclusions: 3 sources (XBSJ002707.5+170748, XBSJ022253.0-044515, XBSJ220320.8+184930) were not detected since each of them lies in the wings of a very bright UV source in the sky, while 17 sources were simply too faint to be detected with the exposure time of the GALEX data along their line of sight. The former three sources were removed from the sample, while for the latter 17 sources we decided to use as an upper limit on the NUV flux (since 98% of the sources have at least a NUV detection) the one corresponding to the faintest detected source (with photometric error <0.5 mag, see Bianchi et al. 2011) within ∼2 arcmin from the position of our undetected target. In order to investigate if these sources have different properties from the detected ones we compare (see Fig. 1) the optical r magnitude against the magnitude in the NUV band for the final sample of GALEX detected sources (black circles) and the sources with GALEX upper limits (red crosses, in the electronic form only); as expected, the latter ones are on average fainter than the detections in the r magnitude too. We also investigated the distribution in the $L_{[2-10]\ keV} - z$ plane of these two samples (see Fig. 2). It is evident that the undetected sources do not show any difference in the X-ray luminosity distribution as compared to the detected ones.

From this sub-sample of 17 source we excluded from the following analysis 2 sources (XBSJ014109.9-675639 and XBSJ050453.4-284532): the reason is that only one optical flux (in the red band) is available and it corresponds to an intrinsic rest-frame $\lambda > 5000$ Å, a wavelength range we did not consider in the SED fitting (see Sect. 3.1 for further details). At this stage, the sample is composed of 195 sources: 180 GALEX detections and 15 sources with GALEX upper limits.

2.3. Cross correlation with the Sloan Digital Sky Survey

All the sources of the XBS sample have a measured optical magnitude (mainly in the red optical band, Caccianiga et al. 2008).

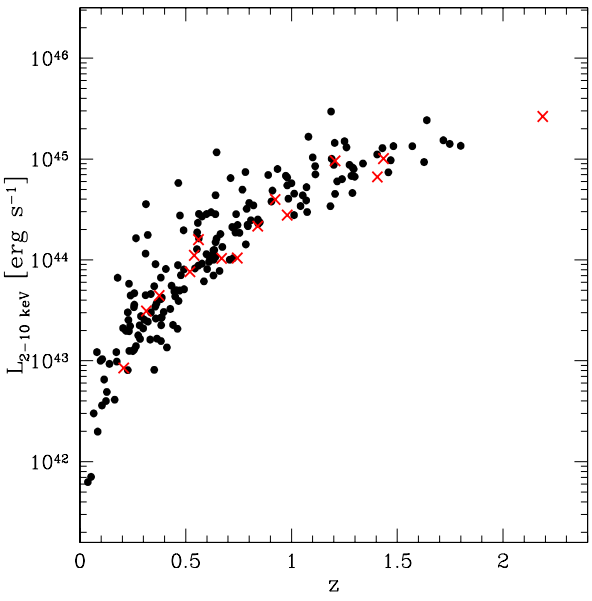

Fig. 2. Distribution in the $L_X - z$ plane of the final sample of Type 1 AGN. Black circles: GALEX detections; red crosses: upper limits.

In order to have more reliable SEDs we need more than one optical point, preferably of the same epoch, to avoid variability effects. Thus we searched for optical information from the SDSS. This is one of the most ambitious surveys, which over eight years of operations (SDSS-I, 2000–2005; SDSS-II, 2005–2008) obtained deep, multi-colour images covering more than a quarter of the sky and created three-dimensional maps containing more than 930 000 galaxies and more than 120 000 quasars. The SDSS uses a dedicated 2.5-m wide-angle optical telescope at Apache Point Observatory (New Mexico), and takes images using photometric system of five filters (named u, g, r, i and z). For more information see `http://www.sdss.org`).

We cross-matched the optical positions of the resulting sample of 195 sources (including both the 180 XBS-GALEX detected sources and the 15 sources with GALEX upper limits) with the *SDSS* DR7 catalogue. This has produced 101 matches, i.e. 101 sources with a measured fluxes in the X-ray, UV (detection or upper limit) and at least one of the optical SDSS (u, g, r, i, z) bands; for the remaining 94 sources we used the optical magnitudes reported in Caccianiga et al. (2008).

To summarise, the final sample of Type 1 unabsorbed AGN ($N_H < 4 \times 10^{21}$ cm^{-2}) used in the analysis reported here is composed of 195 sources; their distribution in the $L_X - z$ and in the $m_{UV} - m_r$ planes are shown in Figs. 1 and 2. The sample covers a range of redshift between 0.03 and ~2 and a wide range of X-ray luminosities, i.e. from 6×10^{41} to 3×10^{45} erg/s. Besides the X-ray information (e.g. spectral slope, flux), which are available for all the sources, we have a) optical magnitudes (from SDSS and/or from the XBS project) for all the 195 sources analysed and b) GALEX detections for 180 sources and GALEX upper limits for 15 sources.

3. Construction of SEDs

3.1. Exclusion of data at $\lambda_{rest} > 5000$ Å

In order to study the intrinsic emission produced by the accretion disc it is necessary to consider wavelength ranges which are free from contamination due to different spectral components (e.g. stellar emission from the host galaxy). Vanden Berk et al. (2001), studying the composite spectra of a sample of SDSS quasars, showed that the slope of the continuum changes abruptly at a rest-frame wavelength of about 5000 Å, becoming steeper (optical spectral index α_ν changing from −0.44 to −2.45) at longer rest-frame wavelengths (see Fig. 5 in Vanden Berk et al. 2001). The authors hypothesise that this behaviour can be partly due to the host-galaxy starlight contamination, as suggested from the presence of stellar absorption lines in the composite spectrum. Nevertheless, they also theorise that this contribution of emission at wavelengths beyond 5000 Å could be caused by an intrinsic change in the quasar continuum (e.g. emission from hot dust). As the emission from the accretion disc is concentrated at wavelengths lower than 5000 Å (we expect a peak of emission in the Far-UV), we did not consider in the fit of the accretion disc emission the rest-frame wavelengths longer than 5000 Å. For this reason two sources (XBSJ014109.9-675639 and XBSJ050453.4-284532) having only GALEX upper limits and optical magnitudes corresponding to a rest-frame wavelength $\lambda > 5000$ Å were already from our analysis (see Sect. 2.2.2). However, since a contamination from the host-galaxy (although weaker) is expected also for wavelength below 5000 Å we have developed a method (see Sect. 3.2.2) to take into account this possible contamination.

3.2. Corrections to measured fluxes

The radiation emitted from an astronomical source has obviously undergone various interactions during its journey, depending on different factors (redshift, environment, etc.). For this reason, in order to reliably study the intrinsic luminosity of our sources, the potential effects on the primary radiation have to be considered. First of all, Galactic reddening: for our sample this effect was estimated from the extinction law computed by Allen (1976), with $R_V = 3.1$, adopting the values of the Galactic colour excess E_{B-V} available for each source in the GALEX database.

3.2.1. Lyman α forest

Even if the large majority (97%) of the sources in our sample lies at $z < 1.6$, we decided to account for the potential attenuation given by absorption of neutral hydrogen in intervening Lyman-α absorption systems. For our sample this is possible only adopting a statistical approach, to produce an estimate of the attenuation $\tau_{eff} = -\ln\langle e^{-\tau}\rangle$, where the average is taken over all possible lines of sights. In order to account for this effect we considered the results reported in Ghisellini et al. (2010), where a relation between the attenuation and redshift has been estimated for the six central wavelengths of the UV filters of the instrument UVOT on board of the satellite *Swift*. We extrapolated the average attenuation corresponding to the effective wavelengths of the GALEX filters FUV and NUV and we found that for $z < 1$ (~75% of the sources) the attenuation produces a flux reduction lower than 15% (5%) in the FUV (NUV) band while, for $1 < z < 1.6$ (~22% of the sources) the reduction in flux is between 15–50% (5–20%) in the FUV (NUV) band. Only 3% of our sources have $1.6 < z < 2.3$, implying corrections between 50–80% (20–70%) in the FUV (NUV). We applied these corrections to the UV fluxes of the whole sample of 195 sources with GALEX detections, even if they are negligible for ~75% of them.

3.2.2. Host Galaxy contamination

A first look at the SEDs obtained after these first corrections to the observed fluxes highlighted out that ~20% of the sources

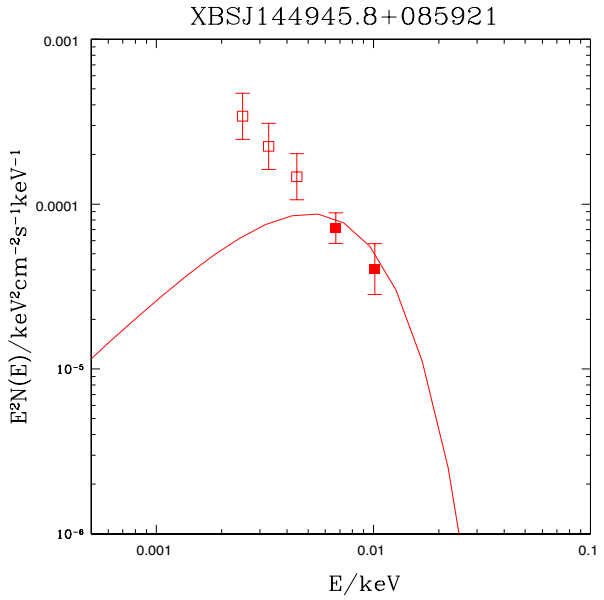

Fig. 3. Example of the rest-frame SED of one source showing the optical fluxes (empty squares) contaminated by the emission contribution of the host galaxy. The solid line represents the accretion disc emission model described in Sect. 3.4.

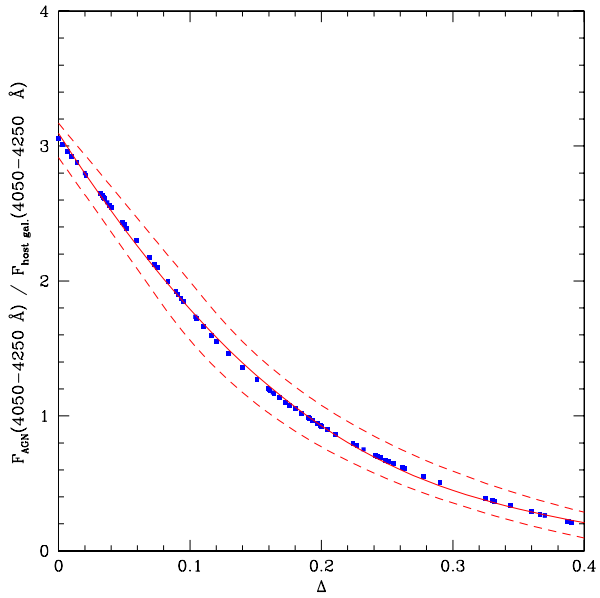

Fig. 4. Plot of the ratio between the fluxes of AGN and host galaxy in the wavelength range 4050–4250 Å as a function of the intensity of the calcium break Δ for the sources in our sample. The relations obtained assuming a host galaxy calcium break of respectively 45% or 55% are shown as dashed lines.

shows a steepening of the SED at the optical wavelengths, in evident disagreement with the expected accretion disc emission continuum (see Fig. 3).

We also noted that all these sources are characterised by a value of the 4000 Å break[1] (also known as *calcium break* Δ) higher than ∼17%. This strongly suggests a not negligible contribution of the stellar emission of the host galaxy to the total observed continuum.

In order to subtract this contribution and to constrain the SED shape at optical wavelengths, we assumed a first approximation model of a host galaxy composed by a step function having a *calcium break* of 50%. This value was chosen as an intermediate value between 45% and 55%, enclosing the 4000 Å breaks computed using the templates reported in Polletta et al. (2007), for elliptical galaxies and spirals S0, Sa, Sb. The AGN is instead represented by a power law with a mean spectral index $\alpha_\nu = -0.44$ in the wavelength region 1500–5000 Å (Vanden Berk et al. 2001). Superimposing these two components we derived an empirical relation between the observed 4000 Å break and the relative normalization of the AGN component with respect to the host galaxy component. This procedure allowed us to derive an empirical correction for the contamination of the host-galaxy for all the sources with measured values of the 4000 Å break.

In Fig. 4 we report the ratio between the fluxes of AGN and host galaxy in the wavelength range 4050–4250 Å as a function of the intensity of the calcium break Δ measured for the sources in our sample (blue points).

The data points have been fitted by a best fit relation described by the polynomial:

$$y = a + bx + cx^2 + dx^3 + ex^4 \quad (2)$$

where $y = \frac{\mathrm{Flux_{AGN}(4050-4250\ \text{Å})}}{\mathrm{Flux_{gal}(4050-4250\ \text{Å})}}$, $x = \Delta$, $a = 3.09$, $b = -15.23$, $c = 20.96$, $d = 12.34$ and $e = -36.64$. This plot and the relative best fit relation represent a tool to derive an estimate of the contribution of the host galaxy to the AGN emission, once the intensity of the 4000 Å break is known. We also show the expected relation when the intensity of the host-galaxy 4000 Å break takes values in the range between 45% (lower dashed line) and 55% (upper dashed line). A variation from 45% to 55% of the assumed host-galaxy calcium break implies a variation on the accretion disc luminosity of ∼45% at 2σ, with a mean variation of ∼14%. Observing the empirical relations plotted in Fig. 4 we can infer that the relative optical flux ratio AGN/host galaxy changes from ∼15% (for observed Δ less than ∼15%) up to a maximum of 60% (for observed Δ ∼ 40%). We also tested that the results obtained in this work (discussed in Sect. 4) were not statistically affected by a change in the range 45–55% of our assumed $\Delta_{\mathrm{galaxy}} = 50\%$.

Furthermore we also checked if a variation of the AGN spectral index could lead to different results: considering the uncertainty of ≈0.1 on the spectral index, reported by Vanden Berk et al. (2001), we found that the accretion disc luminosities are affected by less then 1%.

3.2.3. Intrinsic extinction

The shape of the Big Blue Bump in the optical-UV region of AGN spectra is notoriously prone to effects of reddening: it is thus of great importance to account for intrinsic extinction (at the source redshift) at these wavelengths, in order to constrain the effective energy output. The effect is stronger in type 2 objects but a weaker effect is likely to be present in Type 1 objects as well. These corrections are not trivial, as the exact shape of the extinction curve in the far-UV for AGN is still a matter of debate.

We adopted the results of Gaskell & Benker (2007), who derived a mean extinction curve for 17 AGN with data from *FUSE* and *HST*.

[1] The 4000 Å break is defined as $\Delta = \frac{F^+ - F^-}{F^+}$ where F^+ and F^- represent the mean value of the flux density (expressed per unit frequency) in the region 4050–4250 Å and 3750–3950 Å (in the source's rest frame) respectively.

We also verified "a posteriori" that these corrections are in good agreement with the expected SED shapes.

The extinction curve obtained by Gaskell & Benker (2007) is only valid in the range 1216 Å–6565 Å. To apply the intrinsic absorption correction below 1216 Å, we extrapolated this curve by preserving the flat trend that characterises the UV emission at short wavelengths.

The intrinsic colour excess E_{B-V} for each source was derived from the values of intrinsic column density $N_{\rm H}$ measured from the X-ray spectral analysis, assuming a Galactic gas-to-dust ratio $N_{\rm H}/E_{B-V} = 4.8 \times 10^{21}$ cm^{-2} mag^{-1} (Bohlin et al. 1978). We recall that there are claims in the literature of a non-Galactic gas-to-dust ratio for some AGN (e.g. Maiolino et al. 2001), thus there could be objects where this assumption cannot be fulfilled. However, from the analysis of the optical and X-ray spectra of the AGN of the XBS sample, we found good consistency between the optical and the X-ray classifications, with very few exceptions (Caccianiga et al. 2004; Corral et al. 2011) thus supporting the idea of using the Galactic gas-to-dust ratio. Despite having reliable X-ray spectral information, we only have upper limits on $N_{\rm H}$ for ∼68% of the sources in the sample.

To derive the best guess for the intrinsic $N_{\rm H}$ for each source we made use of the survival analysis, an efficient tool to work with censored data (Isobe et al. 1986, 1990). By using this statistical approach we could estimate a cumulative and a differential distribution of $N_{\rm H}$ for the whole sample of AGN.

The differential distribution was then fitted with a gaussian curve, deriving values for the mean and the sigma of the $N_{\rm H}$ distribution. Thus, for each source with $N_{\rm H}$ upper limits, we produced a series of 100 random values between the minimum $N_{\rm H}^{\rm min}$ of the distribution and the upper limit relative to the individual source. Finally, we adopted the average of these 100 values as the estimated $N_{\rm H}^{\rm estim}$ of the source; the 1σ confidence interval on this average encloses the 68% of the values of $N_{\rm H}$ computed for each source around $N_{\rm H}^{\rm estim}$. The derived $N_{\rm H}^{\rm estim}$ (and the relative 68% confidence error) for each source was used to derive the corresponding E_{B-V} using the equation reported above.

3.2.4. Emission lines contribution

The presence of broad emission lines within the bandpass of a given filter contributes significantly to the observed photometric magnitudes.

It is thus important to correct for the presence of the emission lines to obtain magnitudes closer to the continuum emission alone.

The "redshift dependent" magnitude correction is given by ("Allen's Astrophysical Quantities", 1990):

$$\Delta m = 2.5 \log_{10}\left(1 + (EW)_{\rm e}(1+z)\frac{R_m(\lambda)}{\int R_m(\lambda){\rm d}\lambda}\right) \quad (3)$$

where $(EW)_{\rm e}$ is the rest-frame equivalent width of the emission line, $\lambda = \lambda_{\rm e}(1+z)$ is the observed wavelength of the line and R_m is the response of the filter (Å^{-1})[2].

Only the most prominent AGN emission lines in the wavelengths of interest were considered: Lyα+NV, CIV, MgII, OIV+Lyβ and CIII+SiIII. The rest frame equivalent widths assumed to derive these corrections were taken from Telfer et al. (2002), and these equivalent widths were based on the investigations of 184 QSOs at $z > 0.33$ having *HST* spectra. The line that produces the higher contamination to the measured continuum is the Lyα emission line. This line contribution to the computed magnitudes can amount to 0.4–0.5 mag in the FUV, for objects in the 0.1–0.4 redshift range, and to 0.2–0.3 mag in the NUV, for objects in the 0.6–1.2 redshift range. The equivalent width of the Lyα line used here is in very good agreement with the average one computed from the composite quasar spectra of the SDSS (Vanden Berk et al. 2001). Another significant contribution is produced by the CIV emission line (e.g. ∼0.2 mag for sources at $1.1 < z < 1.5$ in the u band of the SDSS). In this case the equivalent width of the CIV emission line considered here (54 Å) is quite different from the one computed by Vanden Berk et al. (2001) (24 Å); we stress that in the last case the variation in magnitude would be ∼0.1 mag.

3.3. Errors on fluxes

3.3.1. GALEX Photometric errors

The GR4 UV source extractor of the GALEX image processing pipeline reports photometric uncertainties for each object by assuming the observations are limited by Poisson noise. Therefore, the magnitude errors given in the GR4 object tables do not take additional sources of noise into account, including unknown variances of the detector background level and flat-field maps, or any other systematic errors present in the data. To account for these errors we referred to the work of Trammell et al. (2007). Assuming that the bulk of the stars observed in a GALEX field are non-variable, Trammell et al. (2007) used fields with multi-epoch observations as a tool for analysing the repeatability of the GALEX UV photometry for the same objects, using a large number of objects to empirically estimate the true photometric uncertainties. They derived an empirical relation between the NUV (FUV) magnitude and the corresponding true photometric error for both the AIS and DIS surveys. Applying this empirical relation to the GALEX magnitudes of our sources we find that the actual photometric errors are on average ∼0.2 mag (in the FUV band) and ∼0.11 (in the NUV band) larger than the Poissonian errors quoted in the GR4 tables.

3.3.2. Errors due to long-term variability

To account for the the lack of simultaneity in the optical and UV data it is necessary to have an estimate of the average uncertainties on optical and UV fluxes, due to long term variability. De Vries et al. (2005), in a study on optical long term variability of a sample of 41 391 quasars, derived a distribution of the quasar variability as a function of the time-lag between observations. In this work De Vries et al. (2005) found that in a time-lag of years the magnitude difference given by long term variability is ∼0.35 mag; consequently, we associated this value to the long term variability for each source.

3.3.3. Total errors

The asymmetric 1σ total errors on the corrected fluxes that were adopted hereafter are given by the quadratic sum of the 1σ errors due to long term variability, the 1σ errors due to the photometric errors, and 1σ errors related to the corrections for the intrinsic extinction.

[2] http://svo.cab.inta-csic.es/theory/filters/

3.4. The accretion disc emission model

We described the optical-UV data points with a simple multi-colour disc model (DISKPN in the XSPEC12 package, Arnaud 1996). The parameters of this model are $kT_{\rm max}$ (maximum temperature of the accretion disc), $R_{\rm in}$ (inner radius of the accretion disc), and the normalization K (for details on this model see Gierlinski et al. 1999). In our study the inner radius $R_{\rm in}$ was set at 6.0 gravitational radii, and the normalization K was left as a free parameter. We created a grid of models corresponding to values of $kT_{\rm max}$ in the range between $kT \approx 1$ eV and $kT \approx 10$ eV, and we fitted these models to the photometric data with our routines.

For the 15 sources with only an upper limit from GALEX, we assumed a fixed average temperature of the accretion disc ($kT_{\rm max} \approx 4$ eV, as derived from the best-fit temperature computed for the 180 sources with detected GALEX fluxes) or a lower value of $T_{\rm max}$, in case of inconsistency of the UV upper limits with the fit with $kT_{\rm max} \approx 4$ eV. In these cases the SED normalization was determined using only the optical data.

3.5. Resulting SEDs

One example of the optical-UV-Xray spectral energy distribution obtained applying the correction discussed so far is shown in Fig. 5. The SEDs for all the remaining 194 objects are reported in the appendix. We also show the best-fit power-law model in the X-ray energy range 2–10 keV obtained from the X-ray spectral analysis (for more details see C11).

The optical/UV SED was carried out using the model and the grid of $kT_{\rm max}$ quoted in Sect. 3.4 leaving the normalization as free parameter. For each $kT_{\rm max}$ the best fit normalization was established by calculating an asymmetric weighted mean that uses the asymmetric errors as weights in the computation. Finally for each source, we chose the model whose $T_{\rm max}$ minimises the value of the reduced χ^2. Given this best fit $T_{\rm max}$, the asymmetric range of 1σ errors on the disc luminosity reported hereafter is given by the normalization range corresponding to $\chi^2_{\rm min} \pm 1$.

3.6. Bolometric luminosities

In Fig. 6 we report the distribution of the accretion disc luminosities, which were computed by integrating over the optical-UV continuum spectra of each source. The accretion disc luminosity covers a luminosity range $42.4 < \log(L_{\rm disc}) < 47.3$ erg/s with a median value $\log(L_{\rm disc})^{\rm med} \cong 45.4$ erg/s.

The bolometric luminosities were obtained as the sum of the accretion disc luminosity and the 0.1–500 keV X-ray luminosity, and the distribution is reported in Fig. 6. We computed this with the photon indices Γ available from the X-ray spectral analysis (C11) and introduced an exponential cut-off at 200 keV (Dadina 2008), $F(E) \propto E^{-\Gamma} e^{-E/200}$. The values of $L_{[2-10]\ \rm keV}$ and Γ used hereafter are reported in Table 2.

Since the largest part of the bolometric luminosity is given by the accretion disc luminosity we obtained a very similar distribution, covering the range $42.8 < \log(L_{\rm bol}) < 47.3$ erg/s with median value $\log(L_{\rm bol})^{\rm med} \cong 45.5$ erg/s.

4. Results

We derived the accretion disc luminosities, the X-ray luminosities, and the bolometric luminosities for a significant sample of Type 1 AGN covering a wide range of redshift ($0.03 < z \lesssim 2.2$) and a wide range of X-ray luminosities

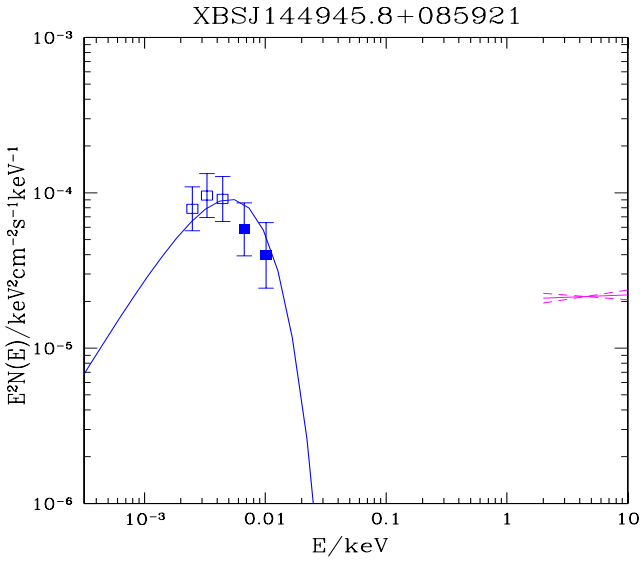

Fig. 5. Example of the optical-UV-Xray spectral energy distribution obtained by applying the correction discussed so far. The filled blue squares are the fluxes in the GALEX NUV/FUV bands, while the empty squares represent the optical data. The fit used the model quoted in Sect. 3.4 (blue curve in the electronic form). The magenta curve is the best-fit power-law model in the X-ray energy range 2–10 keV obtained from the X-ray spectral analysis (see C11) The dashed magenta lines represent the errors on the best-fit model of the X-ray data, given by the errors on the spectral index Γ.

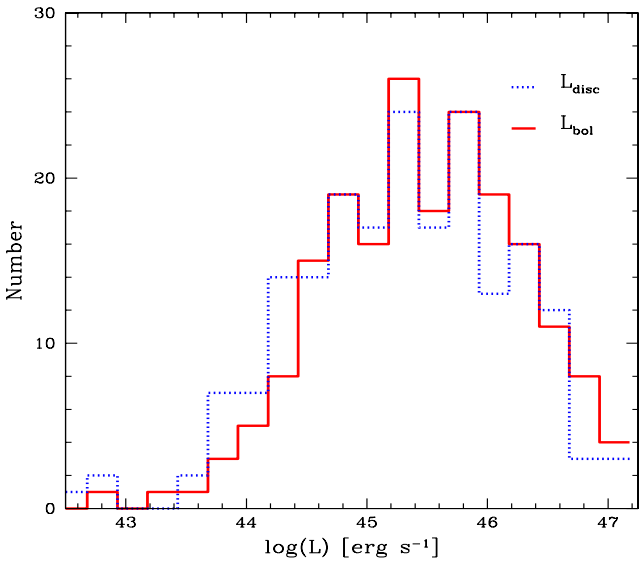

Fig. 6. Distribution of the AGN accretion disc luminosities (dotted blue line), computed by integrating over the optical-UV continuum spectra of each source and distribution of the bolometric luminosities (solid red line), obtained as a sum of the accretion disc luminosities and the 0.1–500 keV X-ray luminosities.

($41.8 < \log L_{[2-10]\ \rm keV} < 45.5$ erg/s). The next step is to investigate the correlations between $L_{\rm disc}$, $L_{[2-10]\ \rm keV}$, and the bolometric correction $k_{\rm bol} = \frac{L_{\rm bol}}{L_{[2-10]\ \rm keV}}$.

We computed the slope of the relation between two linearly correlated variables using two different methods

1. a linear least squares regression method choosing:
   a) X as independent variable (LSQ($y|x$));
   b) Y as independent variable (LSQ($x|y$));

2. a symmetric approach (i.e. without fixing one of the variables as independent and the other as dependent) that computes the bisector between the two least squares regression lines obtained by interchanging the choice of the independent variable (hereafter the "bisector method", Isobe et al. 1990).

In the following we use the bisector method in those cases where the choice of the independent variable is not obvious, and otherwise the linear least square regression of the dependent variable Y against the independent variable X (LSQ($y|x$)).

The study of correlations between outputs at different wavelengths is better done by directly comparing luminosities rather than fluxes, since any correlation in the luminosity space will be distorted in the flux space unless the luminosities are linearly correlated (Feigelson & Berg 1983; Padovani 1992). However, the use of luminosities instead of fluxes always introduces a redshift bias in flux limited samples, as luminosities are strongly correlated with redshift. It is therefore crucial to estimate the influence of this effect on the correlations in order to draw reliable conclusions on the true physical relationship between two redshift-dependent variables.

A way of dealing with this problem is via a partial-correlation analysis, i.e. computing the correlation between two variables (e.g. $L_{\rm disc}$, $L_{\rm [2-10]\ keV}$) and checking the effect of additional parameters (in this case the redshift) that the two variables depend on. The procedure used here is based on the Spearman rank-order correlation coefficient $r_{S,z}$ (and the two-sided probability of no correlation P, computed given the degrees of freedom and the t-value) as modified by Kendall & Stuart (1979) and Padovani (1992), in order to take the dependence on z into account. We assumed the correlation to be marginally significant if the probability P of no correlation is less than 10%, significant if $P \leq 5\%$, and highly significant if $P \leq 1\%$.

Finally, to check the stability of our results, the analysis was done for the main sample of 195 sources and for a sub-sample of 176 sources (*Low-err* sample hereafter) obtained by excluding the 19 sources with the highest uncertainties (i.e. those sources having an uncertainty (1σ) on $k_{\rm bol}$ of more than a factor 1.5).

4.1. $L_{[2-10]\ keV} - L_{disc}$

The of the correlation between X-ray and UV luminosities has been, in the past, the subject of many works on optically or X-ray selected samples of AGNs (see Sect. 5.1 for an account of these works). For our sources, the Spearman correlation coefficient is $r_{S,z} = 0.34$, giving a highly significant correlation ($P < 10^{-3}$) according to our criteria, and a similar highly significant correlation is obtained for the sub-sample *Low-err*.

Treating $L_{\rm [2-10]\ keV}$ as the independent variable, we found

$$\log L_{\rm disc} = (1.009 \pm 0.05) \log L_{\rm [2-10]\ keV} + 0.84, \quad (4)$$

and while treating $L_{\rm disc}$ as the independent variable we found

$$\log L_{\rm disc} = (1.38 \pm 0.06) \log L_{\rm [2-10]\ keV} - 15.71. \quad (5)$$

Computing the bisector of the two regression lines as described by Isobe et al. (1990) the best-fit relation is

$$\log L_{\rm disc} = (1.18 \pm 0.05) \log L_{\rm [2-10]\ keV} - 6.68. \quad (6)$$

In Fig. 7 we display the relations (4), (5), and (6), between $L_{\rm [2-10]\ keV}$ and $L_{\rm disc}$.

A similar relation was obtained for the *Low err* sub-sample. Using the "bisector method" we obtain $\log L_{\rm disc} = (1.20 \pm 0.05) \log L_{\rm [2-10]\ keV} - 7.65$.

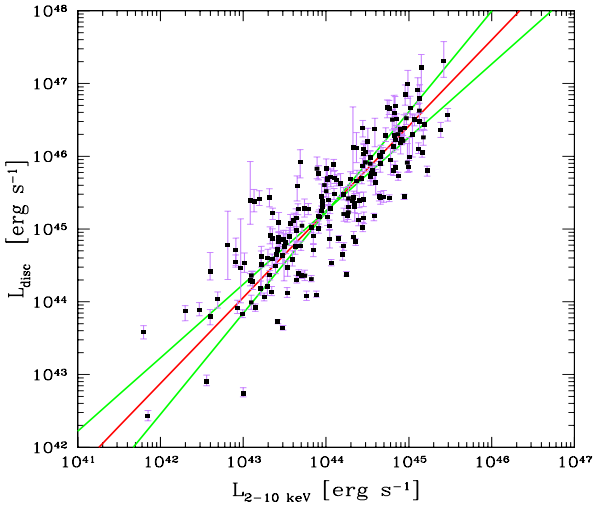

Fig. 7. Plot of $L_{\rm disc}$ vs. X-ray luminosity $L_{\rm [2-10]\ keV}$ for our sample of sources. The two green lines represent the best-fit regression lines, given by Eqs. (4) and (5), obtained by interchanging the independent and dependent variable; the red line is the bisector of these two lines, parametrised by Eq. (6).

It is worth noting that the correlation between the disc and the X-ray luminosity has often been studied in the literature by using the monochromatic optical luminosity, $L_{2500\ \text{Å}}$, and the monochromatic X-ray luminosity at 2 keV, $L_{2\ \rm keV}$. For completeness, we also adopted this approach. For each source, $L_{2500\ \text{Å}}$ was computed using the intrinsic best-fit SED discussed in Sect. 3.5, while $L_{2\ \rm keV}$ was derived from the intrinsic X-ray spectrum (C11). If we use these two quantities for our sample we obtain

$$\log L_{2500\ \text{Å}} = (1.05 \pm 0.05) \log L_{2\ \rm keV} + 2.20 \quad (7)$$

if treating $L_{2\ \rm keV}$ as the independent variable,

$$\log L_{2500\ \text{Å}} = (1.33 \pm 0.05) \log L_{2\ \rm keV} - 5.09 \quad (8)$$

when treating $L_{2500\ \text{Å}}$ as the independent variable, and

$$\log L_{2500\ \text{Å}} = (1.18 \pm 0.05) \log L_{2\ \rm keV} - 1.20 \quad (9)$$

using the "bisector" method. The derived slopes are in very good agreement with those derived using $\log L_{\rm disc}$ and $\log L_{\rm [2-10]\ keV}$, confirming the equivalence of the two approaches.

Finally, we also tried to evaluate whether β ($L_{\rm disc} \propto L^{\beta}_{\rm [2-10]\ keV}$) could change as a function of the redshift, by splitting the sample in two sub-samples containing almost the same number of sources (having z above and below 0.6, respectively). We found marginal (2σ) evidence of an evolution of the slope with redshift, because it is steeper for the high z sub-sample.

4.2. $k_{bol} - L_{[2-10]\ keV}$

A fundamental parameter for cosmological studies of AGN is the bolometric correction to the hard X-ray (2–10 keV), $k_{\rm bol}$, defined in Eq. (1). In Fig. 8 we display $k_{\rm bol}$ against the 2–10 keV X-ray luminosity. Since the dependence of $L_{\rm disc}$ from $L_{\rm [2-10]\ keV}$ is very close to (although statistically different from) linear, the "slope" in the correlation between $k_{\rm bol}$ and $L_{\rm [2-10]\ keV}$ (that was found to be highly significant when the redshift is considered) is expected to be close to 0. Indeed, using the data shown in Fig. 8 we derived a best fit relation (assuming this time $L_{\rm [2-10]\ keV}$ as

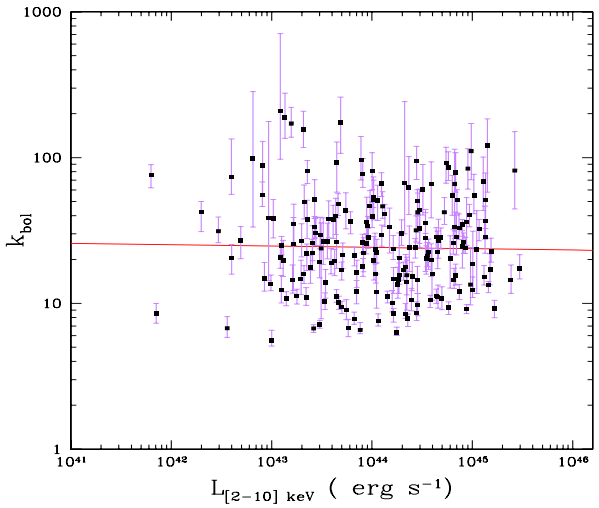

Fig. 8. Plot of bolometric correction vs. X-ray luminosity $L_{[2-10]\mathrm{keV}}$ for our sample of sources. The red line represents the best fit relation obtained assuming $L_{[2-10]\ \mathrm{keV}}$ as independent variable.

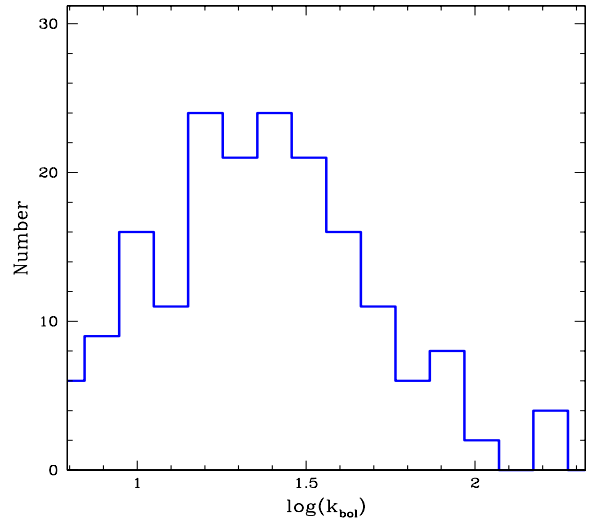

Fig. 9. Histogram of the bolometric corrections for the AGN population (obtained using the *Low-err* sample composed of 176 objects).

the independent variable since k_{bol} and $L_{[2-10]\ \mathrm{keV}}$ are related, see Eq. (1)) with a flat slope[3], $\log k_{\mathrm{bol}} \propto -(0.01 \pm 0.04) \times \log L_{\mathrm{X}}$.

This flat slope (Fig. 8) implies a variation of less than 10% in k_{bol} over about five order of magnitude in luminosities. This said, and given the very large dispersion observed, k_{bol} could be therefore considered practically independent from $L_{[2-10]\ \mathrm{keV}}$. It is worth noting that the bulk of this large dispersion is intrinsic; i.e., the measurement errors do not constitute the dominant source of dispersion. In Fig. 9 we report the histogram of the bolometric corrections derived using the *Low-err* sample (176 objects), in order to give a "representative" distribution of k_{bol} for the AGN population.

[3] This slope is very close to what is expected from the relationship $L_{\mathrm{disc}} \propto L^{\beta}_{[2-10]\ \mathrm{keV}}$ when we apply the *same* fitting method (i.e. assuming $L_{[2-10]\ \mathrm{keV}}$ as the independent variable) as requested from a statistical point of view (see Andreon & Hurn 2010, for a discussion of this point). In this case, if $\beta = 1.009$ (see Eq. (4)), and if we assume that $L_{\mathrm{bol}} \sim L_{\mathrm{disc}}$, we expect $\log k_{\mathrm{bol}} \propto 0.01 \times \log L_{\mathrm{X}}$, well within the errors (0.04) on the slope derived from the fit ($\beta = -0.01$).

Table 1. Spearman rank correlation coefficients ($r_{S,z}$) and probabilities of null correlation (P) for the samples considered in this work.

sample	Correlation	$r_{S,z}$	P
Main sample(195)	$L_{\mathrm{disc}} - L_{[2-10]\ \mathrm{keV}}$	0.34	$<10^{-3}$
	$k_{\mathrm{bol}} - L_{[2-10]\ \mathrm{keV}}$	−0.29	$<10^{-6}$
Low − err(176)	$L_{\mathrm{disc}} - L_{[2-10]\ \mathrm{keV}}$	0.35	$<10^{-4}$
	$k_{\mathrm{bol}} - L_{[2-10]\ \mathrm{keV}}$	−0.23	$<10^{-3}$

Notes. In parenthesis the number of sources in each sample.

5. Discussion

5.1. The X-ray to optical/UV correlation

The study of the correlation between X-ray and UV luminosities has been subject of many works on optically or X-ray selected samples of AGNs. This correlation is found to be $L_{\mathrm{UV}} \propto L^{\beta}_{\mathrm{X}}$, with β ranging, in most studies, from 1.2 to 1.6 (Avni & Tananbaum 1982, 1986; Kriss & Canizares 1985; Anderson & Margon 1987; Wilkes et al. 1994; Yuan et al. 1998; Vignali et al. 2003; Strateva et al. 2005; Steffen et al. 2006; Just et al. 2007; Young et al. 2009; Lusso et al. 2010; Grupe et al. 2010; Stalin et al. 2010). This correlation provides a strong constraint on the physical processes at work, since it tells us that the fraction of power in the accretion disc corona, emitted in the X-rays, decreases/increases as a function of the accretion disc power (mainly emitted in the UV).

A direct comparison between our results and previous works is not very straightforward since different samples (each one with its selection effects that should be carefully evaluated) and different fitting methods (LSQ($y|x$)), LSQ($x|y$), or else the bisector method, have been used in the past. Furthermore, as also stressed by Green et al. (2009), different regression methods can yield very different results in samples with large dispersions.

As discussed in Isobe et al. (1990) when the physics (or the question to be solved) does not clearly indicate which variable depends on the other, a symmetric approach (such as the bisector method) should provide the best guess for the *intrinsic* relationship between the two variables (e.g. the X-ray and the disc luminosities in this case). Using the bisector method we found a slope that is different from linear at $\sim 3.6\sigma$, i.e. $L_{\mathrm{disc}} \propto L^{(1.18 \pm 0.05)}_{[2-10]\ \mathrm{keV}}$, and this result can now be compared with those obtained from other authors using a similar symmetric approach.

Statistically we found that our best-fit slope differs $\sim 2.8\sigma$ from the slope obtained by Lusso et al. (2010, $\beta = 1.32 \pm 0.04$), 4.6σ from Just et al. (2007, $\beta = 1.41 \pm 0.01$), and 5.6σ from Green et al. (2009, $\beta = 0.90 \pm 0.02$). However, there are a number of differences between our analysis and those reported above that can alleviate these differences.

First of all, as mentioned above, we are dealing with a statistically representative sample of X-ray selected, *spectroscopically confirmed*, Type 1 AGN. For all the studied objects we have an X-ray spectrum allowing us to measure the intrinsic X-ray luminosity; UV data from GALEX are available for about 93% of the sample. Finally we also tried to account for the factors contaminating or absorbing the primary radiation emitted from the AGN.

For the optically selected sample of SDSS AGN used in Green et al. (2009), the result quoted above refers to what is obtained with their "Main" sample (~2300 sources) having an X-ray detection fraction of only about 50%. When using their "zLxBox" sample, with a detection fraction of 100%,

Green et al. (2009) obtain $\beta = 1.19 \pm 0.02$, in excellent agreement with our results. Just et al. (2007) combine a sample of 26 optically selected, X-ray-observed AGN, at high z (between 1.5 and 4.5) with an homogeneous sample of 333 optically selected AGN from Steffen et al. (2006). Most of the Type 1 unabsorbed AGN have been classified as such using only photometric data. Finally Lusso et al. (2010) use a sample of X-ray selected Type 1 AGN from the COSMOS survey (545 objects) with about 40% of the objects with a photometric redshift and a classification based on their multi-band SED. All considered, it is difficult to say whether these differences in sample selections have any influence on the best-fit relationship. We aimed at obtaining the most accurate result by adopting a new large (195 objects), statistically complete sample of X-ray selected Type 1 AGN, spanning a wide range of redshift ($0.03 < z \lesssim 2.2$) and X-ray luminosities ($41.8 < \log L_{[2-10]\,\mathrm{keV}} < 45.5$ erg/s), with complete spectroscopic identifications and accurate X-ray spectral analysis (C11); furthermore, we also accounted for the factors contaminating or absorbing the primary radiation emitted from the AGN. Because statistically representative and composed of "X-ray bright" sources, this sample is ideal for this kind of investigation.

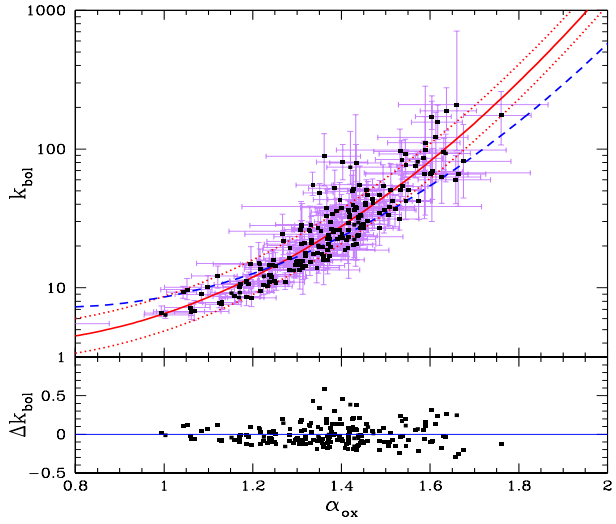

Fig. 10. *Upper panel*: plot of k_{bol} against α_{ox} for our sample of Type 1 AGN. The solid line and dotted lines represent our best fit and the range of variation with respect to the best-fit, including 68% of the sources. The dashed line represent the best fit relation computed by Lusso et al. (2010); in the *bottom panel* we show the residuals with respect to our best-fit relationship.

5.2. The bolometric correction, k_{bol}

The bolometric correction k_{bol}, used to derive the bolometric luminosities (laborious to obtain) from the measured X-ray luminosity, is a fundamental parameter for much important research in current physical cosmology, including the study of the accretion rate (e.g., Marconi et al. 2004), measurement of SMBH densities in the universe (e.g., Marconi et al. 2004), estimation of the active accretion lifetimes or duty cycles (e.g., Hopkins et al. 2005; Adelberger & Steidel 2005), and the conversion the energy density of the X-ray background (which is produced by the integrated X-ray emission of AGN) into a mass density of SMBHs in the local Universe (Soltan 1982).

In Sect. 4.2 we discussed our k_{bol} values, where we had a very shallow dependence with the X-ray luminosity if compared with its very broad distribution (ranging from $k_{bol} \sim 5$ up to $k_{bol} \sim$ few hundred). Similar results were obtained by Vasudevan & Fabian (2007) with a sample of 54 nearby AGN, where they also found a significant spread in k_{bol} (ranging from ∼5 up to ∼100 when Radio Loud objects are removed). It is clear that this rather broad and "flat" distribution implies a very large distribution in the SED of AGN, preventing the use of a single value for the total population. Given the importance of k_{bol} in a cosmological context, many authors investigated the possibility of deriving it from correlations with other simpler observables to compute. After already showing that we cannot use the X-ray luminosities, we discuss below two other observables recently proposed in literature.

In a recent paper, Lusso et al. (2010) have reported a very tight correlation between k_{bol} and the X-ray to optical-UV luminosity ratio α_{ox}[4], which is expected since both quantities are sensitive to the strength of the optical/UV part of the AGN spectrum compared with the X-ray part . However, to compute α_{ox} ideally, only two measurements are needed, one in a proximity of 2500 Å and another of 2 keV (both rest frame). Because of the good correlation between k_{bol} and α_{ox}, Lusso et al. (2010) state that α_{ox} can be used as an accurate estimate (∼20% at 1σ) of k_{bol}. After studying an independent sample of Type 1 AGN using a different analysis to derive the bolometric output, we can now test the validity of this suggestion.

In Fig. 10 we show k_{bol} against α_{ox} for our sample of sources, where a tight correlation is clearly present. However we found a steeper correlation with respect to the best fit in Lusso et al. (2010). Fitting our data with a quadratic polynomial we found the following best-fit relation:

$$\log k_{bol} = 1.05 - 1.52\alpha_{ox} + 1.29\alpha_{ox}^2 \quad (11)$$

(see Fig. 10 upper panel). In the bottom panel we also show the residual Δk_{bol} from our best-fit relation: about 68% ($\simeq 1\sigma$) of the objects are contained within 14% of the best-fit relationship while the maximum deviation of the data points from the expected relation is ∼60%. Provided that measurements around 2500 Å and around 2 keV (rest frame) are available and *that all the discussed corrections to these measurements are applied*, we confirm that α_{ox} could be used as a proxy of k_{bol}. In particular, using the relation (11) the value of k_{bol} can be estimated with a mean accuracy of 0.14 dex (∼30%).

A correlation between the hard X-ray photon index $\Gamma_{2-10\mathrm{keV}}$ and the bolometric correction has been recently proposed by Zhou & Zhao (2010) based on the data on 29 optically selected low-redshift ($z < 0.33$) AGN. They propose that the rest frame $\Gamma_{2-10\mathrm{keV}}$ can be used as a proxy for the bolometric correction with a mean uncertainty of a factor 2–3. The AGN sample discussed here is ideal for testing this correlation, since a detailed X-ray spectral analysis was carried out for all the sources in the sample (see C11). In Fig. 11 we report the relation between the hard X-ray photon index $\Gamma_{2-10\mathrm{keV}}$ and the bolometric correction for our sample of AGN.

A highly significant correlation between the two quantities is clearly present ($r_S = 0.37, P < 10^{-6}$), confirming the results of Zhou & Zhao (2010); for comparison, we also show

[4] Usually the X-ray to optical-UV luminosity ratio in AGN is parametrised by the optical-to-X-ray spectral index

$$\alpha_{ox} = -0.384 \log \left[\frac{L_{2\,\mathrm{keV}}}{L_{2500\,\text{Å}}} \right]. \quad (10)$$

For each source $L_{2500\,\text{Å}}$ was computed using the intrinsic best-fit SED discussed in Sect. 3.5, while $L_{2\,\mathrm{keV}}$ was derived from the intrinsic X-ray spectrum (C11).

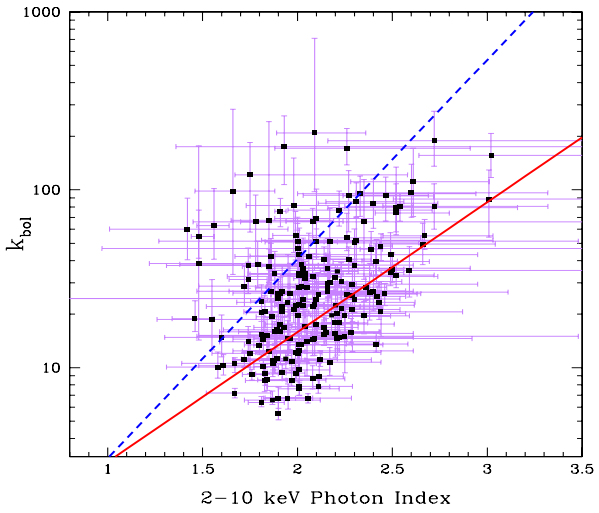

Fig. 11. Plot of $k_{\rm bol}$ vs. the 2–10 keV photon index $\Gamma_{2-10{\rm keV}}$. We show our best-fit relation (red solid line) and the best-fit relation computed by Zhou & Zhao (2010) (blue dashed line).

in Fig. 11 the best-fit relationship reported by Zhou & Zhao (2010), obtained using a symmetric approach ($\log k_{\rm bol} = (1.12 \pm 0.30)\Gamma_{2-10\ {\rm keV}} - (0.63 \pm 0.53)$). For our sample, the best-fit relation, obtained assuming $\Gamma_{2-10\ {\rm keV}}$ as independent variable, is

$$\log k_{\rm bol} = (0.73 \pm 0.04)\Gamma_{2-10\ {\rm keV}} - (0.26 \pm 0.07). \quad (12)$$

The divergence between the best-fit relation derived for our data set and the Zhou & Zhao (2010) relationship can be attributed to the different statistical approach and to selection effects arising when comparing X-ray and optically selected samples. We conclude that Eq. (12) can be adopted to derive $k_{\rm bol}$ from $\Gamma_{2-10\ {\rm keV}}$ with a mean error of ∼0.34 dex (i.e. ∼80%).

The physical justification of the observed $k_{\rm bol} - \Gamma_{2-10{\rm keV}}$ relation could be related to the common dependence of these two quantities to the same physical parameter, namely the Eddington ratio ($\lambda_{\rm Edd}$). Indeed, evidence for a direct dependence of both $k_{\rm bol}$ and Γ on $\lambda_{\rm Edd}$ have recently been found by different authors (e.g. Vasudevan 2009; Risaliti et al. 2009; Lusso et al. 2010; Shemmer et al. 2009; Grupe et al. 2010; Caccianiga et al. 2011; Grupe et al. 2011). This common dependence on $\lambda_{\rm Edd}$ may naturally lead to a mutual correlation between these two quantities. A more detailed investigation of these correlations, using the AGN of the XBS, is currently in progress.

6. Summary and conclusions

In this paper we have presented the analysis of the optical-UV-X-ray SEDs of a complete and representative sample of 195 X-ray selected, spectroscopically identified, Type 1 AGN, with intrinsic absorbing column densities $N_{\rm H} < 4\times10^{21}$ cm^{-2}. The adopted sample, spanning a wide range of redshift $0.03 < z \lesssim 2.2$ and X-ray luminosity, 6×10^{41} erg/s $< L_{[2-10]\ {\rm keV}} < 3 \times 10^{45}$ erg/s, is composed of relatively bright AGN and thus ideal for this study. The optical-UV SED was investigated using data from the SDSS, from our own dedicated optical spectroscopy and photometry and from the satellite GALEX, while the X-ray part was studied using data from *XMM-Newton*.

While the X-ray spectra was presented and discussed in C11, we derived here the intrinsic optical-UV SED, trying to take all the factors contaminating or absorbing the primary optical-UV radiation emitted from the AGN into account. In particular we applied correction for

- the Galactic extinction;
- the potential attenuation given by absorption of neutral hydrogen in intervening Lyman-α absorption systems;
- the contamination from the stellar emission of the host galaxy of the AGN;
- the intrinsic extinction, using the mean extinction curve computed by Gaskell & Benker (2007), a galactic gas-to-dust ratio, and the measured values (or upper limits) of intrinsic column density $N_{\rm H}$ available from the X-ray spectral analysis;
- the contribution of the emission lines Lyman α+NV, CIV, MgII, OIV+Lyβ and CIII+SiIII.

The intrinsic optical-UV radiation was thus fitted using an accretion disc emission model.

We investigated here the correlations between the physical parameters inferred from the optical to X-ray SEDs, such as accretion disc luminosity, bolometric luminosity, bolometric correction, and X-ray photon index. We recall that our results are also applicable to Type 2 (obscured) AGNs if the obscuration is a line-of-sight orientation effect and does not affect the intrinsic energy generation mechanisms within AGNs (i.e. if the unified model of AGNs is valid). The main results of this work are the following

1. Using a symmetric fitting approach (the bisector method) we found a highly significant *intrinsic* correlation between the accretion disc luminosity $L_{\rm disc}$ and the X-ray luminosity $L_{[2-10]\ {\rm keV}}$, in the form $L_{\rm disc} \propto L^{\beta}_{[2-10]\ {\rm keV}}$, where $\beta = 1.18 \pm 0.05$. The non-linearity of this relation implies that the fraction of X-ray emission decreases with increasing accretion disc luminosity. We also found marginal evidence that this relationship depends on redshift;
2. We found a very shallow dependence of the bolometric correction on the X-ray luminosity if compared with its very broad distribution (ranging from $k_{\rm bol} \sim 5$ up to $k_{\rm bol} \sim$ few hundred). This rather broad and "flat" distribution (mainly intrinsic, i.e. it is not caused by the measurement errors) implies a very large distribution of the SED in AGN, preventing the use of a single value for the total AGN family. Furthermore, this implies that the X-ray luminosities are not a useful proxy to derive bolometric corrections.
3. We confirm a tight correlation between $k_{\rm bol}$ and α_{ox} and a correlation between $k_{\rm bol}$ and the hard-X-ray photon index. The first correlation could be used to derive a relatively good estimate of $k_{\rm bol}$, with a mean error of ∼30% (providing that all the main corrections discussed here are applied). The second correlation, despite its higher dispersion, can also be adopted (with a mean error of ∼80%) to estimate $k_{\rm bol}$ once the photon index is known.

A correlation analysis of $L_{\rm disc}$, $L_{[2-10]\ {\rm keV}}$, and $k_{\rm bol}$ with the physical parameters of the central supermassive black-hole (e.g. black hole mass and Eddington ratio) for the AGN sample belonging to the XBS survey will be reported in a forthcoming paper. Expanding the analysis to include these parameters may provide a fundamental tool for constraining AGN models (see e.g. Sobolewska et al. 2004a,b).

Acknowledgements. We thank Luciana Bianchi for help with the GALEX data, Stefano Andreon for the useful suggestions about the statistical issues, Valentina Braito, Cristian Vignali and the anonymous referee for many useful suggestions and comments that significantly improved the paper. The authors acknowledge financial support from ASI (grant No. I/088/06/0, COFIS contract and ASI-INAF grant No. I/009/10/0).

References

Adelberger, K. L., & Steidel, C. C. 2005, ApJ, 630, 50
Allen, C. W. 1976, Astrophysical Quantities, Univ. of London (The Athlone Press), 264
Andreon, S., & Hurn, M. A. 2010, MNRAS, 404, 1922
Anderson, S. F., & Margon, B. 1987, ApJ, 314, 111
Antonucci, R. 1993, ARA&A, 31, 473
Arnaud, K. A. 1996, Astronomical Data Analysis Software and Systems V, ed. G. Jacoby, & J. Barnes, ASP Conf. Ser., 101, 17
Avni, Y., & Tananbaum, H. 1982, ApJ, 262, L17
Avni, Y., & Tananbaum, H. 1986, ApJ, 305, 83
Bianchi, L., Efremova, B., Herald, J., et al. 2011, MNRAS, 411, 2770
Bohlin, R. C., Savage, B. D., & Drake, J. F. 1978, ApJ, 224, 132
Buckley, J., & James, I. 1979, Biometrika, 66, 429
Caccianiga, A., Severgnini, P., Braito, V., et al. 2004, A&A, 416, 901
Caccianiga, A., Severgnini, P., Della Ceca, R., et al. 2007, A&A, 470, 557
Caccianiga, A., Severgnini, P., Della Ceca, R., et al. 2008, A&A, 477, 735
Caccianiga, A., Severgnini, P., Della Ceca, R., et al. 2011, Narrow-Line Seyfert 1 Galaxies and their Place in the Universe, Milano, Italy
Corral, A., Della Ceca, R., Caccianiga, A., et al. 2011, A&A, 530, A42
Dadina, M. 2008, A&A, 485, 417
Dempster, A. P., Laird, N. M., & Rubin, D. B. 1977, J. Roy. Stat. Soc. Ser. B, 39, 1
Della Ceca, R., Pellegrini, S., Bassani, L., et al. 2001, A&A, 375, 781
Della Ceca, R., Maccacaro, T., Caccianiga, A., et al. 2004, A&A, 428, 383
Della Ceca, R., Caccianiga, A., Severgnini, P., et al. 2008, A&A, 487, 119
De Vries, W. H., Becker, R. H., White, R. L., & Loomis, C. 2005, AJ, 129, 615
Elvis, M. S., Wilkes, B. J., McDowell, J. C., et al. 1994, ApJS, 95, 1
Feigelson, E. D., & Berg, C. J. 1983, ApJ, 269, 400
Galbiati, E., Caccianiga, A., Maccacaro, T., et al. 2005, A&A, 430, 927
Gallagher, S. C., Brandt, W. N., Chartas, G., et al. 2006, ApJ, 644, 709
Gaskell, C. M., & Benker, A. J. 2007 [arXiv:0711.1013]
Ghisellini, G., Della Ceca, R., Volonteri, M., et al. 2010, MNRAS, 405, 387
Gierliński, M., Zdziarski, A. A., Poutanen, J., et al. 1999, MNRAS, 309, 496
Giustini, M., Cappi, M., & Vignali, C. 2008, A&A, 491, 425
Gunn, J. E., Siegmund, W. A., Mannery, E. J., et al. 2006, AJ, 131, 2332
Green, P. J., Aldcroft, T. L., Richards, G. T., et al. 2009, ApJ, 690, 644
Grupe, D., Komossa, S., Leighly, K. M., & Page, K. L. 2010, ApJS, 187, 64
Grupe, D., Komossa, S., Leighly, K., & Gallo, L. 2011, Narrow-Line Seyfert 1 Galaxies and their Place in the Universe, Milano, Italy
Haardt, F., Maraschi, L., & Ghisellini, G. 1994, ApJ, 432, L95
Hopkins, P. F., Hernquist, L., Martini, P., et al. 2005, ApJ, 625, L71
Hopkins, P. F., Richards, G. T., & Hernquist, L. 2007, ApJ, 654, 731
Isobe, T., Feigelson, E. D., & Nelson, P. I. 1986, ApJ, 306, 490
Isobe, T., Feigelson, E. D., Akritas, M. G., & Babu, G. J. 1990, ApJ, 364, 104
Just, D., Brandt, W. N., Shemmer, O., et al. 2007, ApJ, 665, 1004
Kelly, B. C., Bechtold, J., Trump, J. R., Vestergaard, M., & Siemiginowska, A. 2008, ApJS, 176, 355
Kendall, M., & Stuart, A. 1979, The advanced theory of statistics, Vol. 2, Griffin, London, 4th edition
Kriss G. A., & Canizares C. R. 1985, ApJ, 297, 177
Lavalley, M., Isobe, T., & Feigelson, E. 1992, Astronomical Data Analysis Software and Systems I, ASP Conf. Ser., 25, 1, 245
Lopez-Santiago, J., Micela, G., Sciortino, S., et al. 2007, A&A, 463, 165
Lusso, E., Comastri, A., Vignali, C., et al. 2010, A&A, 512, A34
Maiolino, R., Marconi, A., Salvati, M., et al. 2001, A&A, 365, 28
Malkan, M. A., & Sargent, W. L. W. 1982, ApJ, 254, 22
Marconi, A., Risaliti, G., Gilli, R., et al. 2004, MNRAS, 351, 169
Martin, D. C., Fanson, J., Schiminovich, D., et al. 2005, ApJ, 619, L1
Morrissey, P., Conrow, T., Barlow, T. A., et al. 2007, ApJS, 173, 682
Padovani, P. 1992, A&A, 256, 399
Polletta, M., Tajer, M., Maraschi, L., et al. 2007, ApJ, 663, 81
Risaliti, G., Young, M., & Elvis, M. 2009, ApJ, 700, L6
Sanders, D. B., Phinney, E. S., Neugebauer, G., Soifer, B. T., & Matthews, K. 1989, ApJ, 347, 29
Severgnini, P., Caccianiga, A., Braito, V., et al. 2003, A&A, 406, 483
Shemmer, O., Brandt, W. N., Anderson, S. F., et al. 2009, ApJ, 696, 580
Shields, G. A. 1978, Nature, 272, 706
Sobolewska, M. A., Siemiginowska, A., & Zycki, P. T. 2004a, ApJ, 608, 80
Sobolewska, M. A., Siemiginowska, A., & Zycki, P. T. 2004b, ApJ, 617, 102
Stalin, C. S., Petitjean, P., Srianand, R., et al. 2006, AJ, 131, 2826
Steffen, A. T., Strateva, I., Brandt, W. N., et al. 2006, AJ, 131, 2826
Strateva, I. V., Brandt, W. N., Schneider, D. P., Vanden Berk, D. G., & Vignali, C. 2005, AJ, 130, 387
Soltan, A. 1982, MNRAS, 200, 115
Streblyanska, A., Barcons, X., Carrera, F. J., & Gil-Merino, R. 2010, A&A, 515, A2
Telfer, R. C., Zheng, W., Kriss, G. A., & Davidsen, A. F. 2002, ApJ, 565, 773
Trammell, G. B., Vanden Berk, D. E., Schneider, D. P., et al. 2007, AJ, 133, 1780
Vanden Berk, D. E., Richards, G. T., Bauer, A., et al. 2001, AJ, 122, 549
Vasudevan, R. V., & Fabian, A. C. 2007, MNRAS, 381, 1235
Vasudevan, R. V., Mushotzky, R. F., Winter, L. M., & Fabian, A. C. 2009, MNRAS, 399, 1553
Vignali, C., Brandt, W. N., & Schneider, D. P. 2003, AJ, 125, 433
Ward, M., Elvis, M., Fabbiano, G., et al. 1987, ApJ, 315, 74
Wilkes, B. J., & Elvis, M. S. 1987, ApJ, 323, 243
Wilkes, B. J., Tananbaum, H., Worrall, D. M., et al. 1994, ApJS, 92, 53
Young, M., Elvis, M., & Risaliti, G., 2009, ApJS, 185, 17
Yuan, W., Siebert, J., Tananbaum, H., Worrall, D. M., & Brinkmann, W. 1998, A&A, 334, 498
Zamorani, G., Henry, J. P., Maccacaro, T., et al. 1981, ApJ, 245, 357
Zheng, W., Kriss, G. A., Telfer, R. C., Grimes, J. P., & Davidsen, A. F. 1997, ApJ, 475, 469
Zhou, X.-L., & Zhao, Y. H. 2010, ApJ, 720, L206

Pages 13 to 41 are available in the electronic edition of the journal at http://www.aanda.org

Table 2. Main properties of the sample of 195 Type 1 AGN analysed in this work.

Name XBSJ	z	$\log L_{\rm disc}{}^{a}$	$\log L_{[2-10]\ \rm keV}{}^{a,b}$	$\log L_{\rm bol}{}^{a}$	Γ^{b}	$\alpha_{\rm ox}$	$\log k_{\rm bol}$
000027.7-250442	0.34	$44.64^{+0.09}_{-0.11}$	43.48	$44.76^{+0.09}_{-0.11}$	$1.87^{+0.09}_{-0.08}$	$1.41^{+0.04}_{-0.06}$	$1.29^{+0.09}_{-0.11}$
000031.7-245502	0.28	$44.52^{+0.18}_{-0.32}$	43.22	$44.62^{+0.18}_{-0.32}$	$2.29^{+0.14}_{-0.13}$	$1.33^{+0.09}_{-0.18}$	$1.41^{+0.18}_{-0.32}$
000102.4-245850	0.43	$44.36^{+0.08}_{-0.07}$	43.74	$44.70^{+0.07}_{-0.06}$	$2.12^{+0.13}_{-0.12}$	$1.08^{+0.06}_{-0.06}$	$0.95^{+0.07}_{-0.06}$
001831.6+162925	0.55	$45.71^{+0.10}_{-0.08}$	44.11	$45.78^{+0.10}_{-0.08}$	$2.39^{+0.06}_{-0.06}$	$1.46^{+0.04}_{-0.04}$	$1.67^{+0.10}_{-0.08}$
002618.5+105019	0.47	$45.87^{+0.10}_{-0.08}$	44.44	$45.94^{+0.10}_{-0.08}$	$2.04^{+0.06}_{-0.06}$	$1.44^{+0.04}_{-0.04}$	$1.50^{+0.10}_{-0.08}$
002637.4+165953	0.55	$45.31^{+0.08}_{-0.07}$	44.27	$45.47^{+0.08}_{-0.06}$	$2.15^{+0.07}_{-0.05}$	$1.30^{+0.04}_{-0.04}$	$1.20^{+0.08}_{-0.06}$
003315.5-120700	1.21	$45.91^{+0.26}_{-0.15}$	44.98	$46.11^{+0.25}_{-0.16}$	$2.01^{+0.28}_{-0.16}$	$1.31^{+0.14}_{-0.10}$	$1.13^{+0.25}_{-0.16}$
003316.0-120456	0.66	$45.84^{+0.16}_{-0.14}$	43.89	$45.89^{+0.16}_{-0.14}$	$2.60^{+0.72}_{-0.29}$	$1.54^{+0.07}_{-0.06}$	$2.00^{+0.16}_{-0.14}$
003418.9-115940	0.85	$45.68^{+0.15}_{-0.17}$	44.37	$45.78^{+0.15}_{-0.17}$	$2.10^{+0.44}_{-0.26}$	$1.28^{+0.07}_{-0.08}$	$1.40^{+0.15}_{-0.17}$
005009.9-515934	0.61	$45.06^{+0.08}_{-0.06}$	44.04	$45.24^{+0.08}_{-0.06}$	$2.28^{+0.15}_{-0.13}$	$1.25^{+0.04}_{-0.04}$	$1.21^{+0.08}_{-0.06}$
005031.1-520012	0.46	$45.45^{+0.17}_{-0.17}$	43.95	$45.51^{+0.17}_{-0.17}$	$2.03^{+0.35}_{-0.19}$	$1.50^{+0.07}_{-0.08}$	$1.56^{+0.17}_{-0.17}$
005032.3-521543	1.22	$45.92^{+0.16}_{-0.20}$	44.78	$46.06^{+0.16}_{-0.20}$	$2.21^{+0.36}_{-0.25}$	$1.34^{+0.08}_{-0.12}$	$1.29^{+0.16}_{-0.20}$
010421.4-061418	0.52	$44.09^{+0.06}_{-0.02}$	43.88	$44.70^{+0.05}_{-0.02}$	$1.87^{+0.25}_{-0.15}$	$0.99^{+0.07}_{-0.03}$	$0.82^{+0.05}_{-0.02}$
010432.8-583712	1.64	$46.37^{+0.11}_{-0.10}$	45.38	$46.56^{+0.10}_{-0.09}$	$1.95^{+0.08}_{-0.06}$	$1.25^{+0.06}_{-0.06}$	$1.17^{+0.10}_{-0.09}$
010701.5-172748	0.89	$46.23^{+0.15}_{-0.13}$	44.84	$46.31^{+0.15}_{-0.12}$	$2.02^{+0.35}_{-0.19}$	$1.32^{+0.07}_{-0.06}$	$1.47^{+0.15}_{-0.12}$
010747.2-172044	0.98	$46.67^{+0.11}_{-0.14}$	44.74	$46.70^{+0.11}_{-0.14}$	$2.47^{+0.25}_{-0.22}$	$1.54^{+0.04}_{-0.06}$	$1.96^{+0.11}_{-0.14}$
012000.0-110429	0.35	$44.71^{+0.16}_{-0.21}$	42.91	$44.86^{+0.16}_{-0.21}$	$3.01^{+3.62}_{-0.50}$	$1.36^{+0.08}_{-0.13}$	$1.95^{+0.16}_{-0.21}$
012025.2-105441	1.34	$46.81^{+0.14}_{-0.14}$	44.96	$46.85^{+0.14}_{-0.14}$	$2.40^{+0.34}_{-0.29}$	$1.56^{+0.06}_{-0.06}$	$1.90^{+0.14}_{-0.14}$
012119.9-110418	0.20	$44.91^{+0.12}_{-0.12}$	43.32	$45.02^{+0.12}_{-0.12}$	$2.66^{+0.38}_{-0.23}$	$1.42^{+0.06}_{-0.06}$	$1.70^{+0.12}_{-0.12}$
012540.2+015752	0.12	$43.80^{+0.09}_{-0.12}$	42.60	$43.92^{+0.09}_{-0.11}$	$1.83^{+0.13}_{-0.11}$	$1.43^{+0.04}_{-0.06}$	$1.31^{+0.09}_{-0.11}$
013204.9-400050	0.45	$45.15^{+0.12}_{-0.12}$	43.64	$45.24^{+0.12}_{-0.12}$	$2.42^{+0.28}_{-0.23}$	$1.45^{+0.06}_{-0.06}$	$1.60^{+0.12}_{-0.12}$
013944.0-674909	0.10	$42.91^{+0.08}_{-0.06}$	42.56	$43.39^{+0.08}_{-0.06}$	$1.95^{+0.13}_{-0.12}$	$1.07^{+0.08}_{-0.08}$	$0.83^{+0.08}_{-0.06}$
014227.0+133453	0.28	$44.07^{+0.05}_{-0.06}$	43.25	$44.30^{+0.05}_{-0.05}$	$1.94^{+0.27}_{-0.23}$	$1.19^{+0.03}_{-0.04}$	$1.05^{+0.05}_{-0.05}$
014251.5+133352	1.07	$46.29^{+0.10}_{-0.09}$	44.72	$46.35^{+0.10}_{-0.08}$	$1.86^{+0.24}_{-0.19}$	$1.52^{+0.04}_{-0.04}$	$1.62^{+0.10}_{-0.08}$
015957.5+003309	0.31	$44.53^{+0.05}_{-0.04}$	44.06	$44.94^{+0.05}_{-0.04}$	$2.01^{+0.21}_{-0.11}$	$1.13^{+0.04}_{-0.04}$	$0.88^{+0.05}_{-0.04}$
020029.0+002846	0.17	$43.83^{+0.06}_{-0.05}$	42.99	$44.13^{+0.06}_{-0.05}$	$2.42^{+0.17}_{-0.16}$	$1.22^{+0.04}_{-0.04}$	$1.13^{+0.06}_{-0.05}$
021808.3-045845	0.71	$46.15^{+0.10}_{-0.08}$	44.81	$46.23^{+0.10}_{-0.08}$	$1.91^{+0.07}_{-0.05}$	$1.42^{+0.04}_{-0.04}$	$1.42^{+0.09}_{-0.08}$
021817.4-045113	1.08	$45.78^{+0.06}_{-0.07}$	45.22	$46.18^{+0.05}_{-0.06}$	$1.83^{+0.07}_{-0.05}$	$1.16^{+0.05}_{-0.07}$	$0.96^{+0.05}_{-0.06}$
021820.6-050427	0.65	$45.49^{+0.07}_{-0.08}$	44.21	$45.59^{+0.06}_{-0.07}$	$1.81^{+0.07}_{-0.06}$	$1.44^{+0.03}_{-0.04}$	$1.38^{+0.06}_{-0.07}$
021923.2-045148	0.63	$45.53^{+0.10}_{-0.08}$	44.00	$45.61^{+0.10}_{-0.08}$	$2.41^{+0.12}_{-0.07}$	$1.43^{+0.04}_{-0.04}$	$1.61^{+0.10}_{-0.08}$
023459.7-294436	0.45	$45.92^{+0.17}_{-0.21}$	43.69	$45.93^{+0.17}_{-0.21}$	$1.93^{+1.83}_{-0.57}$	$1.76^{+0.07}_{-0.08}$	$2.24^{+0.17}_{-0.21}$
024200.9+000020	1.11	$46.21^{+0.07}_{-0.04}$	44.93	$46.31^{+0.07}_{-0.04}$	$2.03^{+0.08}_{-0.07}$	$1.44^{+0.03}_{-0.02}$	$1.38^{+0.07}_{-0.04}$
024204.7+000814	0.38	$45.42^{+0.11}_{-0.09}$	43.20	$45.43^{+0.11}_{-0.09}$	$2.26^{+0.65}_{-0.38}$	$1.61^{+0.04}_{-0.04}$	$2.24^{+0.11}_{-0.09}$
024207.3+000037	0.38	$44.83^{+0.06}_{-0.07}$	43.43	$44.95^{+0.06}_{-0.07}$	$2.52^{+0.20}_{-0.14}$	$1.37^{+0.03}_{-0.04}$	$1.52^{+0.06}_{-0.07}$
024325.6-000413	0.36	$44.43^{+0.11}_{-0.11}$	43.54	$44.66^{+0.10}_{-0.11}$	$1.74^{+0.28}_{-0.15}$	$1.33^{+0.06}_{-0.08}$	$1.12^{+0.10}_{-0.10}$
025606.1+001635	0.63	$45.29^{+0.09}_{-0.07}$	44.05	$45.40^{+0.09}_{-0.07}$	$2.20^{+0.41}_{-0.21}$	$1.37^{+0.04}_{-0.04}$	$1.35^{+0.09}_{-0.07}$
025645.4+000031	0.36	$43.73^{+0.03}_{-0.03}$	43.42	$44.25^{+0.03}_{-0.03}$	$2.06^{+0.23}_{-0.20}$	$1.06^{+0.03}_{-0.04}$	$0.83^{+0.03}_{-0.03}$
030206.8-000121	0.64	$45.44^{+0.05}_{-0.06}$	44.64	$45.70^{+0.05}_{-0.05}$	$1.89^{+0.05}_{-0.05}$	$1.22^{+0.03}_{-0.04}$	$1.05^{+0.05}_{-0.05}$
031015.5-765131	1.19	$46.54^{+0.10}_{-0.08}$	45.47	$46.70^{+0.09}_{-0.07}$	$1.91^{+0.04}_{-0.04}$	$1.35^{+0.05}_{-0.04}$	$1.23^{+0.09}_{-0.07}$
031311.7-765428	1.27	$46.37^{+0.18}_{-0.18}$	44.94	$46.49^{+0.16}_{-0.16}$	$2.16^{+0.75}_{-0.16}$	$1.42^{+0.08}_{-0.08}$	$1.54^{+0.16}_{-0.16}$
031401.3-545959	0.84	$45.41^{+0.11}_{-0.10}$	44.40	$45.59^{+0.10}_{-0.10}$	$1.84^{+0.35}_{-0.36}$	$1.31^{+0.06}_{-0.06}$	$1.19^{+0.10}_{-0.10}$
031549.4-551811	0.81	$45.15^{+0.09}_{-0.08}$	44.39	$45.43^{+0.08}_{-0.07}$	$1.87^{+0.23}_{-0.21}$	$1.23^{+0.06}_{-0.06}$	$1.03^{+0.08}_{-0.07}$
031859.2-441627	0.14	$44.46^{+0.68}_{-0.47}$	42.97	$44.56^{+0.66}_{-0.43}$	$1.48^{+0.31}_{-0.26}$	$1.43^{+0.28}_{-0.26}$	$1.59^{+0.66}_{-0.43}$
033208.7-274735	0.54	$45.17^{+0.10}_{-0.14}$	43.92	$45.27^{+0.10}_{-0.13}$	$1.99^{+0.15}_{-0.11}$	$1.43^{+0.05}_{-0.07}$	$1.35^{+0.10}_{-0.13}$
033506.0-255619	1.43	$46.92^{+0.17}_{-0.20}$	45.11	$46.95^{+0.17}_{-0.20}$	$2.10^{+0.30}_{-0.22}$	$1.61^{+0.07}_{-0.08}$	$1.85^{+0.17}_{-0.20}$
033851.4-352646	1.07	$46.33^{+0.15}_{-0.24}$	44.59	$46.37^{+0.15}_{-0.23}$	$1.78^{+0.08}_{-0.08}$	$1.62^{+0.06}_{-0.10}$	$1.79^{+0.15}_{-0.23}$
033912.1-352813	0.47	$44.58^{+0.12}_{-0.09}$	43.59	$44.87^{+0.10}_{-0.07}$	$1.46^{+0.10}_{-0.12}$	$1.41^{+0.07}_{-0.06}$	$1.28^{+0.10}_{-0.07}$
033942.8-352411	1.04	$45.97^{+0.09}_{-0.07}$	44.53	$46.08^{+0.09}_{-0.07}$	$2.50^{+0.06}_{-0.07}$	$1.38^{+0.04}_{-0.04}$	$1.54^{+0.09}_{-0.07}$
041108.1-711341	0.92	$45.64^{+0.18}_{-0.17}$	44.60	$45.80^{+0.18}_{-0.18}$	$1.91^{+0.52}_{-0.32}$	$1.36^{+0.09}_{-0.10}$	$1.20^{+0.18}_{-0.18}$
043448.3-775329	0.10	$42.73^{+0.08}_{-0.04}$	43.00	$43.74^{+0.07}_{-0.04}$	1.90^{c}	$0.70^{+0.18}_{-0.27}$	$0.74^{+0.07}_{-0.04}$
050446.3-283821	0.84	$44.89^{+0.07}_{-0.02}$	44.33	$45.26^{+0.07}_{-0.02}$	$1.97^{+0.18}_{-0.14}$	$1.17^{+0.06}_{-0.01}$	$0.93^{+0.07}_{-0.02}$
050501.8-284149	0.26	$44.28^{+0.14}_{-0.11}$	43.11	$44.41^{+0.14}_{-0.11}$	$2.18^{+0.09}_{-0.09}$	$1.35^{+0.07}_{-0.06}$	$1.29^{+0.14}_{-0.11}$
051651.9+794314	0.56	$46.13^{+0.22}_{-0.20}$	44.37	$46.18^{+0.21}_{-0.19}$	$1.56^{+0.08}_{-0.09}$	$1.63^{+0.09}_{-0.08}$	$1.81^{+0.21}_{-0.19}$
051822.6+793208	0.05	$42.43^{+0.07}_{-0.07}$	41.85	$42.78^{+0.07}_{-0.06}$	$1.83^{+0.12}_{-0.10}$	$1.20^{+0.06}_{-0.06}$	$0.93^{+0.07}_{-0.06}$
051955.5-455727	0.56	$45.22^{+0.08}_{-0.10}$	44.21	$45.39^{+0.08}_{-0.10}$	$2.09^{+0.06}_{-0.06}$	$1.24^{+0.04}_{-0.06}$	$1.18^{+0.08}_{-0.10}$
052022.0-252309	0.75	$45.33^{+0.16}_{-0.20}$	44.35	$45.50^{+0.15}_{-0.20}$	$2.05^{+0.38}_{-0.17}$	$1.32^{+0.08}_{-0.13}$	$1.16^{+0.15}_{-0.20}$
052116.2-252957	0.33	$44.18^{+0.10}_{-0.09}$	43.21	$44.37^{+0.10}_{-0.09}$	$2.21^{+0.71}_{-0.44}$	$1.30^{+0.06}_{-0.06}$	$1.16^{+0.10}_{-0.09}$

Table 2. continued.

Name XBSJ	z	$\log L_{\rm disc}{}^{a}$	$\log L_{[2-10]\ \rm keV}{}^{a,b}$	$\log L_{\rm bol}{}^{a}$	Γ^{b}	$\alpha_{\rm ox}$	$\log k_{\rm bol}$
052144.1-251518	0.32	$44.49^{+0.09}_{-0.11}$	43.39	$44.63^{+0.09}_{-0.11}$	$2.10^{+0.41}_{-0.27}$	$1.34^{+0.04}_{-0.06}$	$1.25^{+0.09}_{-0.11}$
052543.6-334856	0.73	$45.44^{+0.17}_{-0.14}$	44.27	$45.60^{+0.17}_{-0.14}$	$2.44^{+0.43}_{-0.45}$	$1.32^{+0.09}_{-0.08}$	$1.33^{+0.17}_{-0.14}$
065214.1+743230	0.62	$46.07^{+0.15}_{-0.23}$	44.47	$46.12^{+0.15}_{-0.23}$	$2.01^{+0.16}_{-0.15}$	$1.48^{+0.06}_{-0.10}$	$1.65^{+0.15}_{-0.23}$
065400.0+742045	0.36	$45.07^{+0.13}_{-0.13}$	43.57	$45.15^{+0.13}_{-0.13}$	$2.30^{+0.31}_{-0.19}$	$1.43^{+0.06}_{-0.06}$	$1.58^{+0.13}_{-0.13}$
074202.7+742625	0.60	$44.98^{+0.07}_{-0.06}$	44.46	$45.36^{+0.07}_{-0.06}$	$2.01^{+0.16}_{-0.14}$	$1.06^{+0.06}_{-0.06}$	$0.91^{+0.07}_{-0.06}$
074312.1+742937	0.31	$45.77^{+0.09}_{-0.08}$	44.55	$45.88^{+0.09}_{-0.07}$	$1.98^{+0.07}_{-0.07}$	$1.33^{+0.04}_{-0.04}$	$1.33^{+0.09}_{-0.07}$
074352.0+744258	0.80	$45.82^{+0.09}_{-0.12}$	44.56	$45.93^{+0.09}_{-0.12}$	$2.03^{+0.11}_{-0.10}$	$1.38^{+0.04}_{-0.06}$	$1.36^{+0.09}_{-0.12}$
075117.9+180856	0.25	$44.22^{+0.08}_{-0.07}$	43.53	$44.58^{+0.07}_{-0.06}$	$1.61^{+0.13}_{-0.13}$	$1.24^{+0.06}_{-0.06}$	$1.05^{+0.07}_{-0.06}$
080504.6+245156	0.98	$45.02^{+0.08}_{-0.05}$	44.44	$45.38^{+0.07}_{-0.06}$	$2.08^{+0.17}_{-0.16}$	$1.16^{+0.06}_{-0.05}$	$0.94^{+0.07}_{-0.06}$
080608.1+244420	0.36	$45.38^{+0.06}_{-0.07}$	43.96	$45.49^{+0.06}_{-0.07}$	$2.49^{+0.07}_{-0.05}$	$1.38^{+0.03}_{-0.04}$	$1.53^{+0.06}_{-0.07}$
083049.8+524908	1.20	$45.45^{+0.04}_{-0.04}$	44.94	$45.90^{+0.03}_{-0.03}$	$1.76^{+0.06}_{-0.05}$	$1.15^{+0.03}_{-0.04}$	$0.96^{+0.03}_{-0.03}$
083737.0+255151	0.11	$44.54^{+0.13}_{-0.13}$	43.02	$44.60^{+0.13}_{-0.13}$	$1.79^{+0.48}_{-0.41}$	$1.51^{+0.06}_{-0.06}$	$1.58^{+0.13}_{-0.13}$
083737.1+254751	0.08	$44.29^{+0.09}_{-0.08}$	43.09	$44.40^{+0.09}_{-0.07}$	$1.92^{+0.14}_{-0.12}$	$1.37^{+0.04}_{-0.04}$	$1.31^{+0.09}_{-0.07}$
083838.6+253616	0.60	$45.68^{+0.11}_{-0.09}$	43.91	$45.72^{+0.11}_{-0.09}$	$2.22^{+0.49}_{-0.27}$	$1.55^{+0.04}_{-0.04}$	$1.81^{+0.11}_{-0.09}$
083905.9+255010	0.25	$43.99^{+0.10}_{-0.09}$	43.10	$44.19^{+0.10}_{-0.09}$	$2.01^{+0.60}_{-0.35}$	$1.24^{+0.06}_{-0.06}$	$1.09^{+0.10}_{-0.09}$
085530.7+585129	0.91	$45.18^{+0.04}_{-0.06}$	44.58	$45.60^{+0.03}_{-0.05}$	$1.67^{+0.29}_{-0.28}$	$1.17^{+0.03}_{-0.06}$	$1.02^{+0.03}_{-0.05}$
094526.2-085006	0.31	$44.48^{+0.15}_{-0.20}$	43.49	$44.67^{+0.15}_{-0.21}$	$2.25^{+1.23}_{-0.78}$	$1.21^{+0.08}_{-0.14}$	$1.18^{+0.15}_{-0.21}$
094548.3-084824	1.75	$47.22^{+0.18}_{-0.32}$	45.15	$47.24^{+0.18}_{-0.32}$	$1.75^{+0.83}_{-0.08}$	$1.62^{+0.07}_{-0.13}$	$2.09^{+0.18}_{-0.32}$
095054.5+393924	1.30	$46.28^{+0.10}_{-0.08}$	44.83	$46.35^{+0.10}_{-0.08}$	$2.01^{+0.38}_{-0.26}$	$1.42^{+0.04}_{-0.04}$	$1.53^{+0.10}_{-0.08}$
095309.7+013558	0.48	$45.05^{+0.09}_{-0.12}$	43.85	$45.17^{+0.09}_{-0.11}$	$1.89^{+0.40}_{-0.28}$	$1.26^{+0.04}_{-0.06}$	$1.32^{+0.09}_{-0.11}$
095509.6+174124	1.29	$46.24^{+0.07}_{-0.08}$	44.91	$46.33^{+0.06}_{-0.08}$	$1.90^{+0.14}_{-0.09}$	$1.31^{+0.03}_{-0.04}$	$1.42^{+0.06}_{-0.08}$
100100.0+252103	0.79	$45.44^{+0.08}_{-0.07}$	44.33	$45.59^{+0.08}_{-0.07}$	$2.20^{+0.12}_{-0.07}$	$1.35^{+0.04}_{-0.04}$	$1.25^{+0.08}_{-0.07}$
100309.4+554135	0.67	$45.67^{+0.07}_{-0.08}$	44.13	$45.74^{+0.07}_{-0.08}$	$2.27^{+0.12}_{-0.10}$	$1.45^{+0.03}_{-0.04}$	$1.61^{+0.07}_{-0.08}$
100828.8+535408	0.38	$44.85^{+0.07}_{-0.08}$	43.43	$44.92^{+0.07}_{-0.08}$	$2.04^{+0.20}_{-0.15}$	$1.49^{+0.03}_{-0.04}$	$1.49^{+0.07}_{-0.08}$
100921.7+534926	0.39	$44.75^{+0.08}_{-0.10}$	43.63	$44.92^{+0.08}_{-0.10}$	$2.35^{+0.14}_{-0.08}$	$1.28^{+0.04}_{-0.06}$	$1.29^{+0.08}_{-0.10}$
100926.5+533426	1.72	$46.43^{+0.09}_{-0.08}$	45.19	$46.54^{+0.09}_{-0.07}$	$2.01^{+0.13}_{-0.12}$	$1.40^{+0.04}_{-0.04}$	$1.36^{+0.09}_{-0.07}$
101506.0+520157	0.61	$45.60^{+0.10}_{-0.09}$	43.98	$45.65^{+0.10}_{-0.09}$	$2.00^{+1.57}_{-1.03}$	$1.49^{+0.04}_{-0.04}$	$1.67^{+0.10}_{-0.09}$
101838.0+411635	0.58	$45.30^{+0.06}_{-0.07}$	43.96	$45.41^{+0.06}_{-0.07}$	$2.36^{+0.11}_{-0.10}$	$1.33^{+0.03}_{-0.04}$	$1.45^{+0.06}_{-0.07}$
101843.0+413515	0.08	$43.88^{+0.07}_{-0.14}$	42.30	$43.93^{+0.07}_{-0.13}$	$1.86^{+0.20}_{-0.11}$	$1.57^{+0.03}_{-0.06}$	$1.63^{+0.07}_{-0.13}$
101850.5+411506	0.58	$45.70^{+0.06}_{-0.07}$	44.43	$45.81^{+0.06}_{-0.07}$	$2.30^{+0.08}_{-0.05}$	$1.37^{+0.03}_{-0.04}$	$1.38^{+0.06}_{-0.07}$
101922.6+412049	0.24	$44.30^{+0.06}_{-0.05}$	43.65	$44.69^{+0.05}_{-0.04}$	$2.12^{+0.27}_{-0.08}$	$1.19^{+0.04}_{-0.04}$	$1.04^{+0.05}_{-0.04}$
102412.3+042023	1.46	$46.30^{+0.10}_{-0.08}$	44.87	$46.38^{+0.10}_{-0.08}$	$2.01^{+0.16}_{-0.10}$	$1.44^{+0.04}_{-0.04}$	$1.52^{+0.10}_{-0.08}$
103120.0+311404	1.19	$45.85^{+0.10}_{-0.06}$	45.00	$46.09^{+0.09}_{-0.05}$	$1.85^{+0.19}_{-0.14}$	$1.24^{+0.06}_{-0.04}$	$1.09^{+0.09}_{-0.05}$
103154.1+310732	0.30	$44.37^{+0.06}_{-0.07}$	43.32	$44.52^{+0.06}_{-0.07}$	$1.88^{+0.22}_{-0.19}$	$1.37^{+0.03}_{-0.04}$	$1.20^{+0.06}_{-0.07}$
103909.4+205222	0.98	$45.80^{+0.08}_{-0.06}$	44.82	$45.98^{+0.08}_{-0.06}$	$1.96^{+0.26}_{-0.16}$	$1.31^{+0.04}_{-0.04}$	$1.16^{+0.08}_{-0.06}$
103932.7+205426	0.24	$44.14^{+0.07}_{-0.06}$	43.34	$44.38^{+0.07}_{-0.05}$	$1.87^{+0.18}_{-0.15}$	$1.27^{+0.04}_{-0.04}$	$1.04^{+0.07}_{-0.05}$
103935.8+533036	0.23	$44.65^{+0.09}_{-0.12}$	43.40	$44.75^{+0.09}_{-0.12}$	$2.08^{+0.25}_{-0.16}$	$1.33^{+0.04}_{-0.06}$	$1.34^{+0.09}_{-0.12}$
104026.9+204542	0.47	$45.43^{+0.04}_{-0.05}$	44.76	$45.73^{+0.04}_{-0.05}$	$1.99^{+0.05}_{-0.05}$	$1.04^{+0.03}_{-0.04}$	$0.97^{+0.04}_{-0.05}$
104034.3+205110	0.67	$45.70^{+0.14}_{-0.03}$	44.01	$45.75^{+0.14}_{-0.05}$	$2.26^{+0.39}_{-0.18}$	$1.54^{+0.06}_{-0.01}$	$1.73^{+0.14}_{-0.05}$
104425.0-013521	1.57	$46.63^{+0.10}_{-0.13}$	45.13	$46.70^{+0.10}_{-0.13}$	$1.85^{+0.16}_{-0.14}$	$1.52^{+0.04}_{-0.06}$	$1.58^{+0.10}_{-0.13}$
104509.3-012442	0.47	$44.72^{+0.06}_{-0.06}$	43.70	$44.89^{+0.06}_{-0.06}$	$2.14^{+0.18}_{-0.10}$	$1.30^{+0.03}_{-0.04}$	$1.19^{+0.06}_{-0.06}$
104522.1-012843	0.78	$45.74^{+0.05}_{-0.06}$	44.87	$45.96^{+0.05}_{-0.06}$	$2.00^{+0.13}_{-0.03}$	$1.23^{+0.03}_{-0.04}$	$1.09^{+0.05}_{-0.06}$
104912.8+330459	0.23	$43.64^{+0.03}_{-0.03}$	43.48	$44.34^{+0.03}_{-0.03}$	$1.67^{+0.19}_{-0.15}$	$1.06^{+0.04}_{-0.06}$	$0.86^{+0.03}_{-0.03}$
105014.9+331013	1.01	$46.42^{+0.10}_{-0.13}$	44.44	$46.45^{+0.10}_{-0.13}$	$2.33^{+0.61}_{-0.33}$	$1.64^{+0.04}_{-0.05}$	$2.01^{+0.10}_{-0.13}$
105239.7+572431	1.11	$46.51^{+0.07}_{-0.09}$	44.85	$46.56^{+0.07}_{-0.09}$	$2.10^{+0.04}_{-0.03}$	$1.55^{+0.03}_{-0.04}$	$1.71^{+0.07}_{-0.09}$
105316.9+573551	1.20	$46.02^{+0.05}_{-0.06}$	45.16	$46.27^{+0.05}_{-0.05}$	$1.80^{+0.04}_{-0.03}$	$1.29^{+0.03}_{-0.04}$	$1.11^{+0.05}_{-0.05}$
105335.0+572540	0.78	$44.86^{+0.04}_{-0.05}$	44.15	$45.20^{+0.04}_{-0.04}$	$1.72^{+0.08}_{-0.06}$	$1.24^{+0.03}_{-0.04}$	$1.05^{+0.04}_{-0.04}$
105339.7+573104	0.59	$45.28^{+0.07}_{-0.08}$	43.79	$45.35^{+0.07}_{-0.08}$	$2.16^{+0.07}_{-0.07}$	$1.41^{+0.03}_{-0.04}$	$1.56^{+0.07}_{-0.08}$
105624.2-033522	0.63	$45.45^{+0.07}_{-0.08}$	44.10	$45.54^{+0.07}_{-0.08}$	$2.16^{+0.15}_{-0.10}$	$1.42^{+0.03}_{-0.04}$	$1.44^{+0.07}_{-0.08}$
110652.0-182738	1.43	$45.99^{+0.27}_{-0.21}$	45.01	$46.28^{+0.22}_{-0.17}$	$1.55^{+0.36}_{-0.29}$	$1.37^{+0.14}_{-0.15}$	$1.27^{+0.22}_{-0.17}$
111933.0+212756	0.28	$44.59^{+0.06}_{-0.12}$	43.35	$44.69^{+0.06}_{-0.12}$	$1.92^{+0.52}_{-0.40}$	$1.41^{+0.03}_{-0.06}$	$1.34^{+0.06}_{-0.12}$
111942.1+211516	1.29	$46.04^{+0.12}_{-0.16}$	44.66	$46.13^{+0.11}_{-0.15}$	$1.92^{+0.40}_{-0.28}$	$1.46^{+0.05}_{-0.08}$	$1.46^{+0.11}_{-0.15}$
112022.3+125252	0.41	$45.03^{+0.06}_{-0.07}$	43.91	$45.17^{+0.06}_{-0.07}$	$2.22^{+0.15}_{-0.13}$	$1.30^{+0.03}_{-0.04}$	$1.26^{+0.06}_{-0.07}$
112046.7+125429	0.38	$45.02^{+0.06}_{-0.07}$	43.83	$45.15^{+0.06}_{-0.07}$	$2.29^{+0.25}_{-0.15}$	$1.32^{+0.03}_{-0.04}$	$1.33^{+0.06}_{-0.07}$
113106.9+312518	1.48	$46.47^{+0.12}_{-0.12}$	45.13	$46.59^{+0.12}_{-0.11}$	$1.72^{+0.27}_{-0.24}$	$1.45^{+0.06}_{-0.06}$	$1.46^{+0.12}_{-0.11}$
115317.9+364712	0.72	$45.64^{+0.13}_{-0.14}$	44.02	$45.69^{+0.13}_{-0.14}$	$2.00^{+1.48}_{-0.73}$	$1.41^{+0.06}_{-0.06}$	$1.67^{+0.13}_{-0.14}$
120359.1+443715	0.64	$45.40^{+0.09}_{-0.07}$	44.03	$45.40^{+0.11}_{-0.10}$	$2.43^{+0.19}_{-0.19}$	$1.40^{+0.04}_{-0.04}$	$1.37^{+0.11}_{-0.10}$

Table 2. continued.

Name XBSJ	z	$\log L_{\rm disc}{}^{a}$	$\log L_{[2-10]\ \rm keV}{}^{a,b}$	$\log L_{\rm bol}{}^{a}$	Γ^{b}	$\alpha_{\rm ox}$	$\log k_{\rm bol}$
120413.7+443149	0.49	$45.04^{+0.07}_{-0.08}$	43.71	$45.04^{+0.08}_{-0.10}$	$2.23^{+0.22}_{-0.14}$	$1.27^{+0.03}_{-0.04}$	$1.33^{+0.08}_{-0.10}$
123036.2+642531	0.74	$45.16^{+0.17}_{-0.11}$	44.02	$45.31^{+0.17}_{-0.12}$	$2.25^{+0.34}_{-0.21}$	$1.35^{+0.08}_{-0.06}$	$1.29^{+0.17}_{-0.12}$
123116.5+641115	0.45	$44.37^{+0.04}_{-0.05}$	43.70	$44.67^{+0.04}_{-0.04}$	$1.92^{+0.09}_{-0.08}$	$1.22^{+0.03}_{-0.04}$	$0.98^{+0.04}_{-0.05}$
123218.5+640311	1.01	$45.43^{+0.09}_{-0.08}$	44.66	$45.70^{+0.08}_{-0.08}$	$1.88^{+0.25}_{-0.22}$	$1.24^{+0.06}_{-0.06}$	$1.04^{+0.08}_{-0.08}$
123759.6+621102	0.91	$46.05^{+0.07}_{-0.08}$	44.69	$46.14^{+0.07}_{-0.08}$	$2.05^{+0.06}_{-0.06}$	$1.44^{+0.03}_{-0.04}$	$1.45^{+0.07}_{-0.08}$
123800.9+621338	0.44	$45.22^{+0.07}_{-0.09}$	43.36	$45.26^{+0.07}_{-0.09}$	$2.54^{+0.07}_{-0.09}$	$1.57^{+0.03}_{-0.04}$	$1.91^{+0.07}_{-0.09}$
124214.1-112512	0.82	$45.73^{+0.06}_{-0.12}$	44.54	$45.86^{+0.06}_{-0.11}$	$1.81^{+0.09}_{-0.08}$	$1.43^{+0.03}_{-0.06}$	$1.32^{+0.06}_{-0.11}$
124557.6+022659	0.71	$45.81^{+0.13}_{-0.13}$	44.00	$45.89^{+0.13}_{-0.13}$	$2.72^{+0.60}_{-0.47}$	$1.39^{+0.06}_{-0.06}$	$1.89^{+0.13}_{-0.13}$
124607.6+022153	0.49	$45.18^{+0.06}_{-0.07}$	43.90	$45.32^{+0.06}_{-0.07}$	$2.46^{+0.19}_{-0.14}$	$1.32^{+0.03}_{-0.04}$	$1.41^{+0.06}_{-0.07}$
124641.8+022412	0.93	$46.37^{+0.04}_{-0.08}$	44.90	$46.44^{+0.04}_{-0.08}$	$2.21^{+0.11}_{-0.09}$	$1.49^{+0.02}_{-0.04}$	$1.54^{+0.04}_{-0.08}$
124647.9+020955	1.07	$45.89^{+0.13}_{-0.13}$	44.47	$45.96^{+0.13}_{-0.13}$	$2.08^{+0.66}_{-0.45}$	$1.43^{+0.06}_{-0.06}$	$1.49^{+0.13}_{-0.13}$
124914.6-060910	1.63	$46.51^{+0.07}_{-0.08}$	44.97	$46.57^{+0.07}_{-0.08}$	$2.14^{+0.13}_{-0.12}$	$1.47^{+0.03}_{-0.04}$	$1.60^{+0.07}_{-0.08}$
124949.4-060722	1.05	$45.99^{+0.07}_{-0.08}$	44.64	$46.08^{+0.07}_{-0.08}$	$2.16^{+0.11}_{-0.10}$	$1.42^{+0.03}_{-0.04}$	$1.44^{+0.07}_{-0.08}$
130619.7-233857	0.35	$45.29^{+0.12}_{-0.12}$	43.74	$45.37^{+0.12}_{-0.12}$	$2.49^{+0.46}_{-0.34}$	$1.40^{+0.06}_{-0.06}$	$1.63^{+0.12}_{-0.12}$
130658.1-234849	0.38	$44.98^{+0.17}_{-0.17}$	43.65	$45.07^{+0.17}_{-0.18}$	$1.96^{+0.40}_{-0.30}$	$1.38^{+0.08}_{-0.08}$	$1.42^{+0.17}_{-0.18}$
132038.0+341124	0.06	$43.89^{+0.10}_{-0.08}$	42.47	$43.97^{+0.10}_{-0.08}$	$1.74^{+0.10}_{-0.10}$	$1.53^{+0.04}_{-0.04}$	$1.50^{+0.10}_{-0.08}$
132101.6+340656	0.34	$45.28^{+0.07}_{-0.08}$	43.66	$45.35^{+0.07}_{-0.08}$	$2.44^{+0.06}_{-0.06}$	$1.35^{+0.03}_{-0.04}$	$1.68^{+0.07}_{-0.08}$
133807.5+242411	0.63	$45.88^{+0.07}_{-0.09}$	44.09	$45.92^{+0.07}_{-0.09}$	$2.08^{+0.16}_{-0.14}$	$1.60^{+0.03}_{-0.04}$	$1.82^{+0.07}_{-0.09}$
133942.6-315004	0.11	$44.78^{+0.46}_{-0.48}$	42.81	$44.81^{+0.46}_{-0.47}$	$1.66^{+0.22}_{-0.20}$	$1.59^{+0.18}_{-0.20}$	$1.99^{+0.46}_{-0.47}$
134749.9+582111	0.65	$46.50^{+0.07}_{-0.08}$	45.07	$46.58^{+0.07}_{-0.08}$	$2.20^{+0.03}_{-0.03}$	$1.42^{+0.03}_{-0.04}$	$1.51^{+0.07}_{-0.08}$
140100.0-110942	0.16	$44.42^{+0.26}_{-0.12}$	42.60	$44.47^{+0.26}_{-0.12}$	$2.52^{+0.28}_{-0.11}$	$1.42^{+0.11}_{-0.05}$	$1.87^{+0.26}_{-0.12}$
140102.0-111224	0.04	$43.59^{+0.08}_{-0.10}$	41.80	$43.68^{+0.07}_{-0.09}$	$1.91^{+0.03}_{-0.03}$	$1.57^{+0.03}_{-0.04}$	$1.88^{+0.07}_{-0.09}$
140113.4+024016	0.63	$44.69^{+0.07}_{-0.09}$	43.85	$44.92^{+0.07}_{-0.08}$	$1.99^{+0.45}_{-0.21}$	$1.11^{+0.04}_{-0.06}$	$1.07^{+0.07}_{-0.08}$
140127.7+025605	0.26	$44.77^{+0.04}_{-0.06}$	44.22	$45.15^{+0.04}_{-0.06}$	$1.84^{+0.10}_{-0.05}$	$1.19^{+0.03}_{-0.06}$	$0.93^{+0.04}_{-0.06}$
140921.1+261336	1.10	$46.66^{+0.16}_{-0.13}$	45.02	$46.75^{+0.15}_{-0.12}$	$1.48^{+0.08}_{-0.04}$	$1.49^{+0.07}_{-0.06}$	$1.74^{+0.15}_{-0.12}$
141531.5+113156	0.26	$44.40^{+0.05}_{-0.05}$	43.67	$44.68^{+0.04}_{-0.05}$	$1.82^{+0.06}_{-0.05}$	$1.17^{+0.03}_{-0.04}$	$1.01^{+0.04}_{-0.05}$
141722.6+251335	0.56	$45.26^{+0.06}_{-0.08}$	43.94	$45.36^{+0.06}_{-0.07}$	$2.26^{+0.37}_{-0.17}$	$1.40^{+0.03}_{-0.04}$	$1.42^{+0.06}_{-0.07}$
141736.3+523028	0.99	$45.75^{+0.12}_{-0.11}$	44.59	$45.88^{+0.11}_{-0.11}$	$2.00^{+0.07}_{-0.07}$	$1.37^{+0.06}_{-0.06}$	$1.29^{+0.11}_{-0.11}$
141809.1+250040	0.73	$45.39^{+0.06}_{-0.07}$	44.31	$45.54^{+0.06}_{-0.07}$	$1.93^{+0.19}_{-0.16}$	$1.37^{+0.03}_{-0.04}$	$1.22^{+0.06}_{-0.07}$
144937.5+090826	1.26	$46.11^{+0.08}_{-0.06}$	45.12	$46.30^{+0.08}_{-0.06}$	$1.81^{+0.11}_{-0.07}$	$1.33^{+0.04}_{-0.04}$	$1.19^{+0.08}_{-0.06}$
144945.8+085921	0.26	$43.89^{+0.05}_{-0.05}$	43.15	$44.16^{+0.04}_{-0.05}$	$1.97^{+0.09}_{-0.09}$	$1.24^{+0.03}_{-0.04}$	$1.02^{+0.04}_{-0.05}$
150428.3+101856	1.00	$46.66^{+0.11}_{-0.09}$	44.76	$46.69^{+0.11}_{-0.09}$	$2.31^{+0.25}_{-0.16}$	$1.59^{+0.04}_{-0.04}$	$1.93^{+0.11}_{-0.09}$
151815.0+060851	1.29	$46.18^{+0.11}_{-0.15}$	44.90	$46.29^{+0.11}_{-0.15}$	1.90^{c}	$1.40^{+0.05}_{-0.08}$	$1.39^{+0.11}_{-0.15}$
153205.7-082952	1.24	$46.48^{+0.14}_{-0.14}$	44.80	$46.53^{+0.13}_{-0.14}$	$1.99^{+0.13}_{-0.12}$	$1.43^{+0.06}_{-0.06}$	$1.73^{+0.13}_{-0.14}$
153419.0+011808	1.28	$46.66^{+0.13}_{-0.14}$	44.83	$46.71^{+0.13}_{-0.14}$	$2.52^{+0.64}_{-0.36}$	$1.42^{+0.06}_{-0.06}$	$1.88^{+0.13}_{-0.14}$
153456.1+013033	0.31	$45.58^{+0.19}_{-0.14}$	43.65	$45.61^{+0.19}_{-0.14}$	$2.27^{+0.42}_{-0.24}$	$1.57^{+0.08}_{-0.06}$	$1.96^{+0.19}_{-0.14}$
160706.6+075709	0.23	$44.36^{+0.06}_{-0.07}$	43.10	$44.50^{+0.06}_{-0.07}$	$2.42^{+0.15}_{-0.14}$	$1.38^{+0.03}_{-0.04}$	$1.40^{+0.06}_{-0.07}$
160731.5+081202	0.23	$44.55^{+0.09}_{-0.08}$	42.91	$44.65^{+0.09}_{-0.08}$	$2.67^{+0.36}_{-0.22}$	$1.33^{+0.04}_{-0.04}$	$1.74^{+0.09}_{-0.08}$
161544.2+121708	0.21	$43.91^{+0.11}_{-0.07}$	42.93	$44.10^{+0.11}_{-0.09}$	$2.22^{+0.39}_{-0.19}$	$1.22^{+0.06}_{-0.04}$	$1.17^{+0.11}_{-0.09}$
161615.1+121353	0.84	$44.82^{+0.03}_{-0.06}$	44.36	$45.25^{+0.03}_{-0.05}$	$2.01^{+0.28}_{-0.17}$	$1.13^{+0.03}_{-0.06}$	$0.89^{+0.03}_{-0.05}$
161825.4+124145	0.40	$44.86^{+0.12}_{-0.08}$	43.48	$44.96^{+0.12}_{-0.08}$	$2.29^{+0.66}_{-0.45}$	$1.42^{+0.06}_{-0.04}$	$1.47^{+0.12}_{-0.08}$
162813.9+780342	0.64	$46.23^{+0.11}_{-0.09}$	44.45	$46.27^{+0.10}_{-0.09}$	$2.30^{+0.34}_{-0.29}$	$1.43^{+0.04}_{-0.04}$	$1.82^{+0.10}_{-0.09}$
163309.8+571039	0.29	$44.84^{+0.07}_{-0.08}$	43.44	$44.93^{+0.07}_{-0.08}$	$2.23^{+0.32}_{-0.18}$	$1.46^{+0.03}_{-0.04}$	$1.48^{+0.07}_{-0.08}$
163332.3+570520	0.39	$45.03^{+0.13}_{-0.13}$	43.43	$45.09^{+0.13}_{-0.13}$	$2.31^{+0.72}_{-0.50}$	$1.36^{+0.06}_{-0.06}$	$1.66^{+0.13}_{-0.13}$
165406.6+142123	0.64	$45.66^{+0.13}_{-0.13}$	44.18	$45.72^{+0.13}_{-0.13}$	$1.88^{+0.20}_{-0.14}$	$1.45^{+0.06}_{-0.06}$	$1.55^{+0.13}_{-0.13}$
165425.3+142159	0.18	$44.31^{+0.05}_{-0.04}$	43.82	$44.72^{+0.05}_{-0.04}$	$2.11^{+0.06}_{-0.03}$	$1.12^{+0.04}_{-0.04}$	$0.89^{+0.05}_{-0.04}$
165448.5+141311	0.32	$44.41^{+0.02}_{-0.02}$	44.25	$45.06^{+0.02}_{-0.02}$	$1.81^{+0.12}_{-0.07}$	$1.02^{+0.03}_{-0.04}$	$0.81^{+0.02}_{-0.02}$
165800.7+352333	0.13	$44.04^{+0.10}_{-0.13}$	42.69	$44.12^{+0.10}_{-0.12}$	$1.86^{+0.75}_{-0.39}$	$1.49^{+0.04}_{-0.06}$	$1.43^{+0.10}_{-0.12}$
185518.7-462504	0.79	$46.21^{+0.19}_{-0.19}$	44.51	$46.30^{+0.17}_{-0.17}$	$1.42^{+0.53}_{-0.41}$	$1.66^{+0.08}_{-0.08}$	$1.79^{+0.17}_{-0.17}$
185613.7-462239	0.77	$45.46^{+0.09}_{-0.08}$	44.70	$45.74^{+0.08}_{-0.08}$	$2.17^{+0.27}_{-0.23}$	$1.20^{+0.06}_{-0.06}$	$1.04^{+0.08}_{-0.08}$
204159.2-321439	0.74	$45.42^{+0.10}_{-0.10}$	44.45	$45.62^{+0.10}_{-0.09}$	$2.08^{+0.18}_{-0.11}$	$1.26^{+0.06}_{-0.06}$	$1.17^{+0.10}_{-0.09}$
204204.1-321601	0.38	$44.87^{+0.13}_{-0.13}$	43.35	$44.93^{+0.13}_{-0.13}$	$2.02^{+0.38}_{-0.21}$	$1.37^{+0.06}_{-0.06}$	$1.58^{+0.13}_{-0.13}$
204208.2-323523	1.18	$45.87^{+0.18}_{-0.23}$	44.53	$45.96^{+0.17}_{-0.23}$	$2.01^{+0.37}_{-0.23}$	$1.30^{+0.08}_{-0.12}$	$1.43^{+0.17}_{-0.23}$
204548.4-025234	2.19	$47.31^{+0.27}_{-0.22}$	45.42	$47.33^{+0.27}_{-0.27}$	$1.98^{+0.24}_{-0.25}$	$1.68^{+0.11}_{-0.09}$	$1.91^{+0.27}_{-0.27}$
205635.7-044717	0.22	$44.61^{+0.11}_{-0.11}$	43.30	$44.73^{+0.11}_{-0.11}$	$2.40^{+0.17}_{-0.14}$	$1.35^{+0.06}_{-0.06}$	$1.43^{+0.11}_{-0.11}$
205829.9-423634	0.23	$44.08^{+0.07}_{-0.06}$	43.76	$44.59^{+0.06}_{-0.06}$	$1.90^{+0.09}_{-0.08}$	$1.06^{+0.07}_{-0.08}$	$0.83^{+0.06}_{-0.06}$
210325.4-112011	0.72	$46.14^{+0.57}_{-0.36}$	44.33	$46.18^{+0.57}_{-0.35}$	$1.85^{+0.34}_{-0.20}$	$1.61^{+0.23}_{-0.15}$	$1.85^{+0.57}_{-0.35}$

Table 2. continued.

Name XBSJ	z	$\log L_{\rm disc}{}^{a}$	$\log L_{[2-10]\ \rm keV}{}^{a,b}$	$\log L_{\rm bol}{}^{a}$	Γ^{b}	$\alpha_{\rm ox}$	$\log k_{\rm bol}$
210355.3-121858	0.79	$45.39^{+0.13}_{-0.14}$	44.35	$45.56^{+0.13}_{-0.14}$	$2.20^{+0.41}_{-0.15}$	$1.32^{+0.07}_{-0.08}$	$1.21^{+0.13}_{-0.14}$
213002.3-153414	0.56	$46.04^{+0.13}_{-0.14}$	44.46	$46.09^{+0.13}_{-0.13}$	$2.06^{+0.21}_{-0.19}$	$1.55^{+0.06}_{-0.06}$	$1.64^{+0.13}_{-0.13}$
213729.7-423601	0.66	$45.21^{+0.13}_{-0.10}$	44.26	$45.40^{+0.12}_{-0.09}$	$2.02^{+0.43}_{-0.30}$	$1.29^{+0.07}_{-0.06}$	$1.14^{+0.12}_{-0.09}$
213733.2-434800	0.43	$44.82^{+0.16}_{-0.16}$	43.51	$44.94^{+0.16}_{-0.16}$	$2.38^{+0.73}_{-0.50}$	$1.38^{+0.08}_{-0.08}$	$1.42^{+0.16}_{-0.16}$
213757.6-422334	0.36	$44.63^{+0.14}_{-0.15}$	43.22	$44.77^{+0.13}_{-0.15}$	$2.59^{+2.19}_{-0.72}$	$1.42^{+0.07}_{-0.08}$	$1.55^{+0.13}_{-0.15}$
213824.0-423019	0.26	$44.89^{+0.12}_{-0.12}$	43.56	$44.98^{+0.12}_{-0.12}$	$2.16^{+0.11}_{-0.16}$	$1.44^{+0.06}_{-0.06}$	$1.43^{+0.12}_{-0.12}$
213829.8-423958	1.47	$47.00^{+0.19}_{-0.20}$	44.99	$47.04^{+0.19}_{-0.20}$	$2.61^{+0.40}_{-0.33}$	$1.59^{+0.08}_{-0.08}$	$2.06^{+0.19}_{-0.20}$
213852.2-434714	0.46	$45.43^{+0.12}_{-0.12}$	43.32	$45.51^{+0.12}_{-0.12}$	$3.02^{+0.59}_{-0.38}$	$1.62^{+0.06}_{-0.06}$	$2.19^{+0.12}_{-0.12}$
214041.4-234720	0.49	$45.69^{+0.10}_{-0.08}$	44.29	$45.77^{+0.10}_{-0.08}$	$2.17^{+0.09}_{-0.08}$	$1.38^{+0.04}_{-0.04}$	$1.48^{+0.10}_{-0.08}$
220446.8-014535	0.54	$44.86^{+0.13}_{-0.11}$	44.04	$45.13^{+0.12}_{-0.11}$	$1.75^{+0.25}_{-0.20}$	$1.24^{+0.08}_{-0.08}$	$1.08^{+0.12}_{-0.11}$
221623.3-174317	0.75	$45.29^{+0.14}_{-0.13}$	44.27	$45.47^{+0.13}_{-0.12}$	$1.82^{+0.25}_{-0.16}$	$1.34^{+0.07}_{-0.08}$	$1.20^{+0.13}_{-0.12}$
223547.9-255836	0.30	$44.72^{+0.12}_{-0.12}$	43.41	$44.82^{+0.12}_{-0.12}$	$2.11^{+0.27}_{-0.25}$	$1.35^{+0.06}_{-0.06}$	$1.41^{+0.12}_{-0.12}$
223555.0-255833	1.80	$46.80^{+0.19}_{-0.20}$	45.13	$46.84^{+0.19}_{-0.19}$	$2.17^{+0.15}_{-0.13}$	$1.51^{+0.08}_{-0.08}$	$1.71^{+0.19}_{-0.19}$
223949.8+080926	1.41	$46.60^{+0.24}_{-0.32}$	44.82	$46.64^{+0.24}_{-0.34}$	$2.35^{+1.66}_{-0.90}$	$1.59^{+0.10}_{-0.14}$	$1.82^{+0.24}_{-0.34}$
224756.6-642721	0.60	$45.73^{+0.11}_{-0.14}$	44.06	$45.77^{+0.10}_{-0.14}$	$2.00^{+0.21}_{-0.17}$	$1.54^{+0.04}_{-0.06}$	$1.72^{+0.10}_{-0.14}$
225025.1-643225	1.21	$45.89^{+0.15}_{-0.12}$	44.65	$46.00^{+0.14}_{-0.12}$	$2.09^{+0.19}_{-0.14}$	$1.36^{+0.07}_{-0.06}$	$1.35^{+0.14}_{-0.12}$
225050.2-642900	1.25	$46.23^{+0.11}_{-0.11}$	45.18	$46.39^{+0.11}_{-0.10}$	$2.04^{+0.07}_{-0.07}$	$1.35^{+0.06}_{-0.06}$	$1.21^{+0.11}_{-0.10}$
225118.0-175951	0.17	$45.40^{+0.53}_{-0.33}$	43.09	$45.41^{+0.53}_{-0.33}$	$2.09^{+0.27}_{-0.20}$	$1.66^{+0.21}_{-0.13}$	$2.32^{+0.53}_{-0.33}$
230400.4-083755	0.41	$45.38^{+0.17}_{-0.14}$	43.13	$45.41^{+0.17}_{-0.14}$	$2.72^{+0.90}_{-0.56}$	$1.64^{+0.07}_{-0.06}$	$2.28^{+0.17}_{-0.14}$
230434.1+122728	0.23	$44.21^{+0.14}_{-0.13}$	43.29	$44.46^{+0.13}_{-0.11}$	$1.60^{+0.37}_{-0.30}$	$1.20^{+0.08}_{-0.08}$	$1.17^{+0.13}_{-0.11}$
230443.8+121636	1.40	$46.30^{+0.27}_{-0.31}$	45.04	$46.41^{+0.27}_{-0.30}$	$1.95^{+0.29}_{-0.27}$	$1.41^{+0.12}_{-0.17}$	$1.36^{+0.27}_{-0.30}$
230459.6+121205	0.56	$44.65^{+0.11}_{-0.07}$	44.20	$45.20^{+0.09}_{-0.06}$	$1.58^{+0.32}_{-0.27}$	$1.10^{+0.10}_{-0.09}$	$1.00^{+0.09}_{-0.06}$
231342.5-423210	0.97	$45.85^{+0.08}_{-0.06}$	44.83	$46.02^{+0.08}_{-0.06}$	$2.14^{+0.13}_{-0.07}$	$1.30^{+0.04}_{-0.04}$	$1.19^{+0.08}_{-0.06}$
231601.7-424038	0.38	$45.12^{+0.10}_{-0.13}$	43.61	$45.19^{+0.10}_{-0.13}$	$1.74^{+0.42}_{-0.43}$	$1.40^{+0.04}_{-0.06}$	$1.57^{+0.10}_{-0.13}$

Notes. [(a)] The luminosity is expressed in units of erg s^{-1}. [(b)] For a detailed account of the X-ray properties of all the sources see Corral et al. (2011). [(c)] Fixed parameter. We assume the cosmological model $H_0 = 65$ km s^{-1} Mpc^{-1}, $\Omega_\lambda = 0.7$ and $\Omega_{\rm M} = 0.3$ throughout this paper.

Appendix A

We present here the optical-UV-X-ray SEDs obtained applying the correction discussed in Sect. 3.2, for all the 195 sources analysed in this paper. The filled blue squares represent the fluxes in the GALEX NUV/FUV bands, while the empty squares represent the optical data. The upper limits on the NUV/FUV fluxes are represented as downward arrays. The fit has been done using the model quoted in Sect. 3.4 (blue curve). We also show the slope of the best-fit model in the rest-frame energy range 1–10 keV (magenta curve) obtained from the X-ray spectral analysis (for further details see Corral et al. 2011). The dashed magenta lines represent the errors on the best-fit model of the X-ray data, given by the errors on the spectral index Γ.

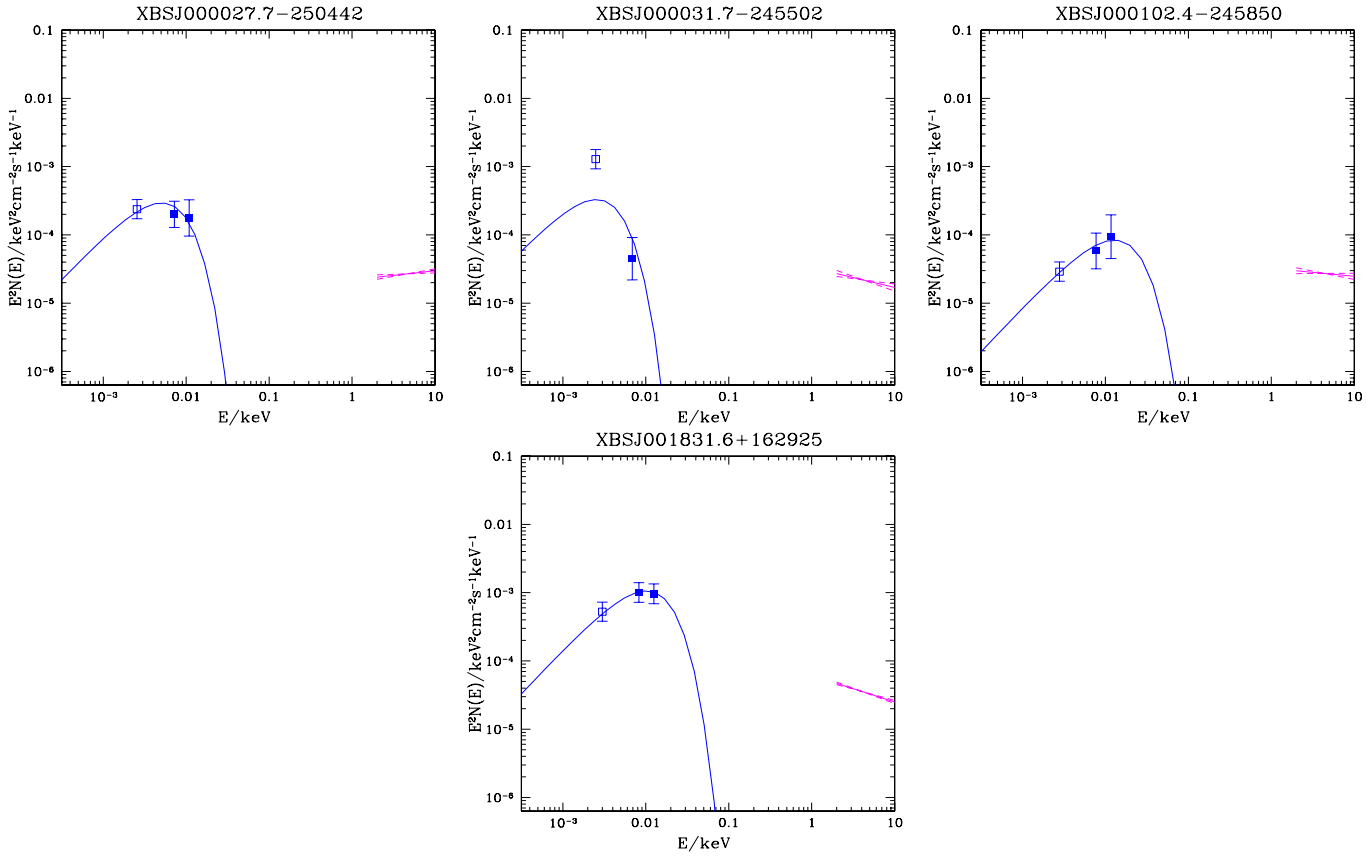

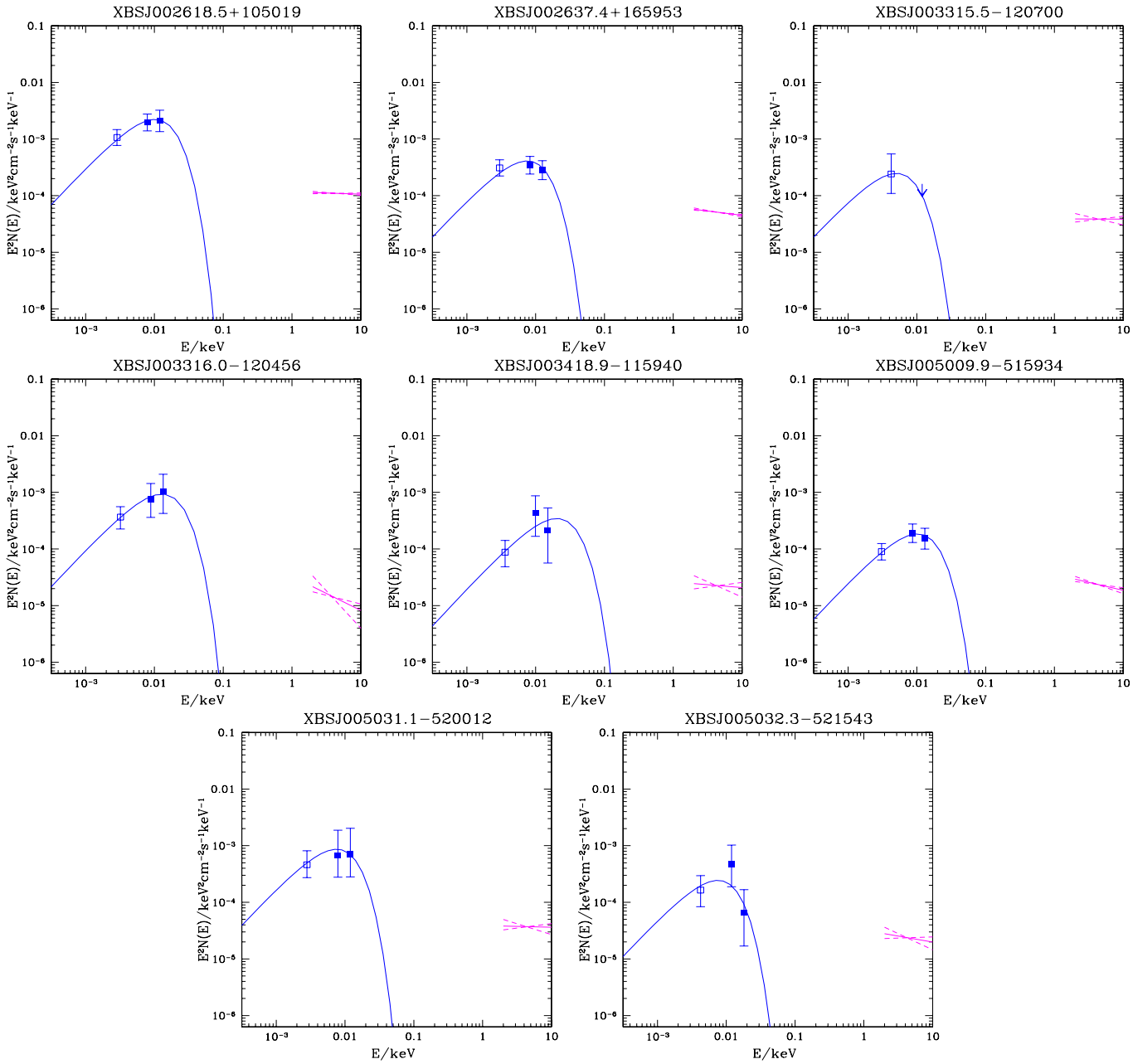
XBSJ002618.5+105019
XBSJ002637.4+165953
XBSJ003315.5−120700
XBSJ003316.0−120456
XBSJ003418.9−115940
XBSJ005009.9−515934
XBSJ005031.1−520012
XBSJ005032.3−521543
E²N(E)/keV²cm⁻²s⁻¹keV⁻¹
E/keV

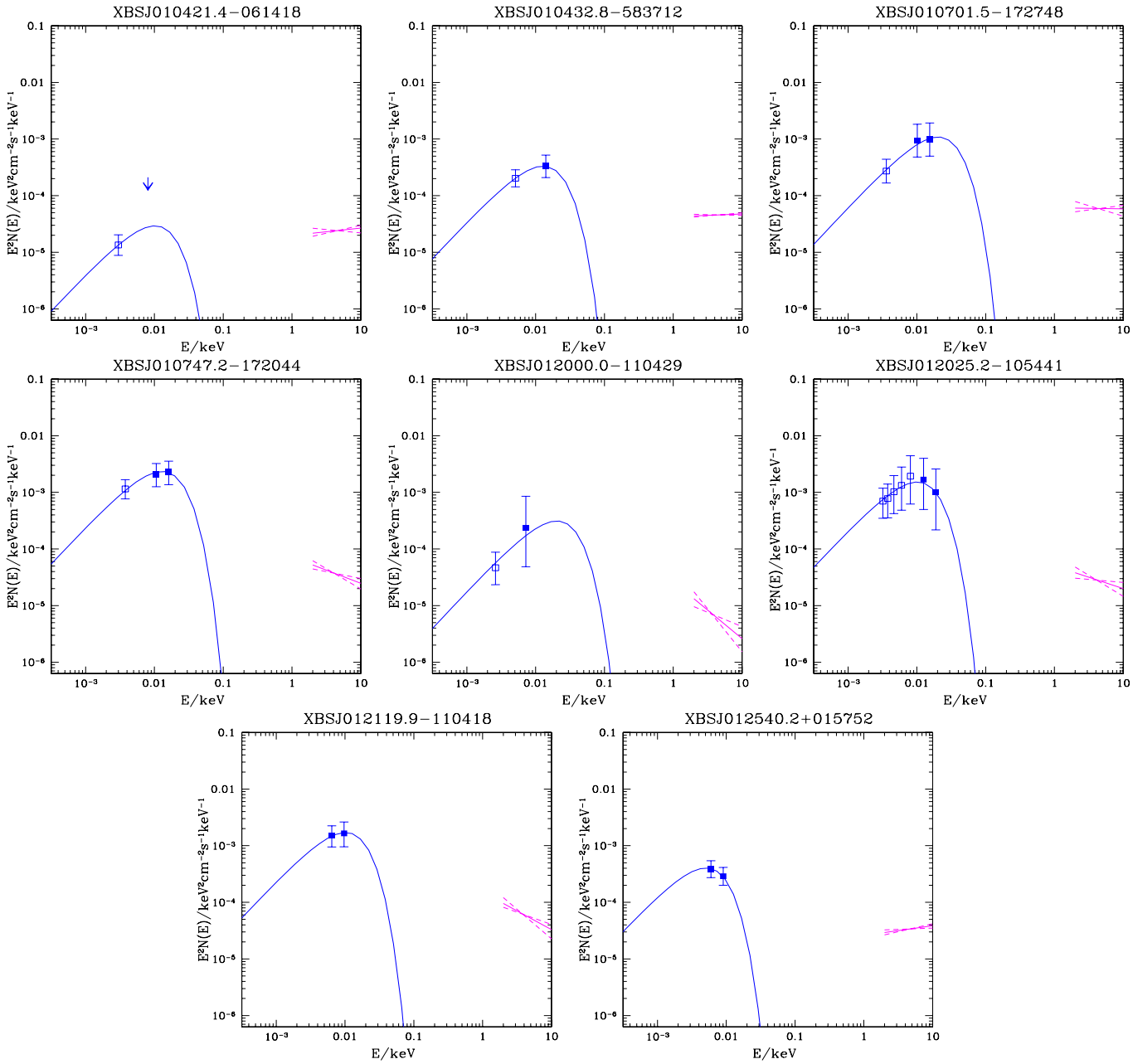
XBSJ010421.4−061418
XBSJ010432.8−583712
XBSJ010701.5−172748
XBSJ010747.2−172044
XBSJ012000.0−110429
XBSJ012025.2−105441
XBSJ012119.9−110418
XBSJ012540.2+015752
E²N(E)/keV²cm⁻²s⁻¹keV⁻¹
E/keV

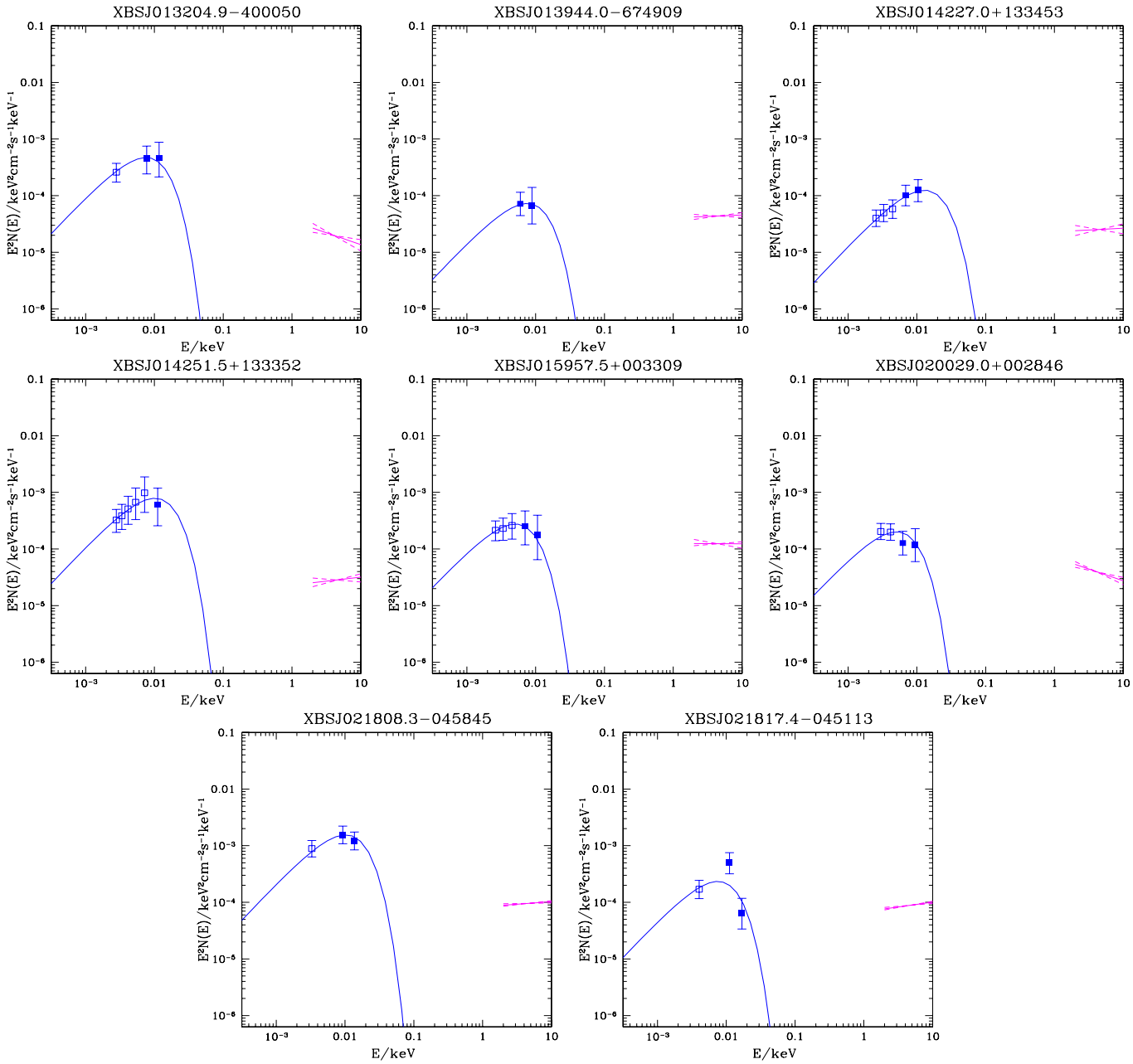
XBSJ013204.9−400050
XBSJ013944.0−674909
XBSJ014227.0+133453
XBSJ014251.5+133352
XBSJ015957.5+003309
XBSJ020029.0+002846
XBSJ021808.3−045845
XBSJ021817.4−045113
E²N(E)/keV²cm⁻²s⁻¹keV⁻¹
E/keV

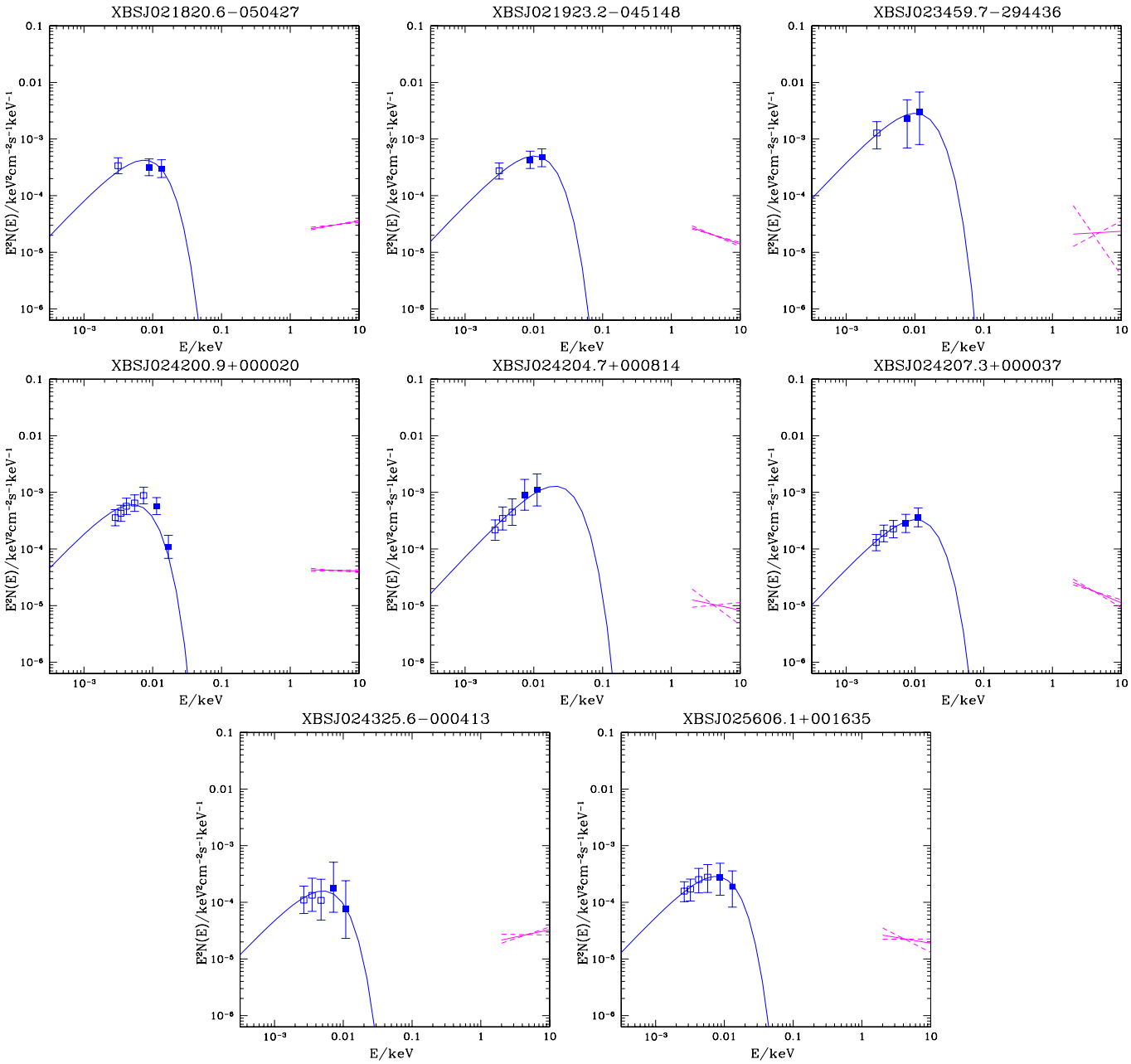
XBSJ021820.6−050427
XBSJ021923.2−045148
XBSJ023459.7−294436
XBSJ024200.9+000020
XBSJ024204.7+000814
XBSJ024207.3+000037
XBSJ024325.6−000413
XBSJ025606.1+001635
E²N(E)/keV²cm⁻²s⁻¹keV⁻¹
E/keV

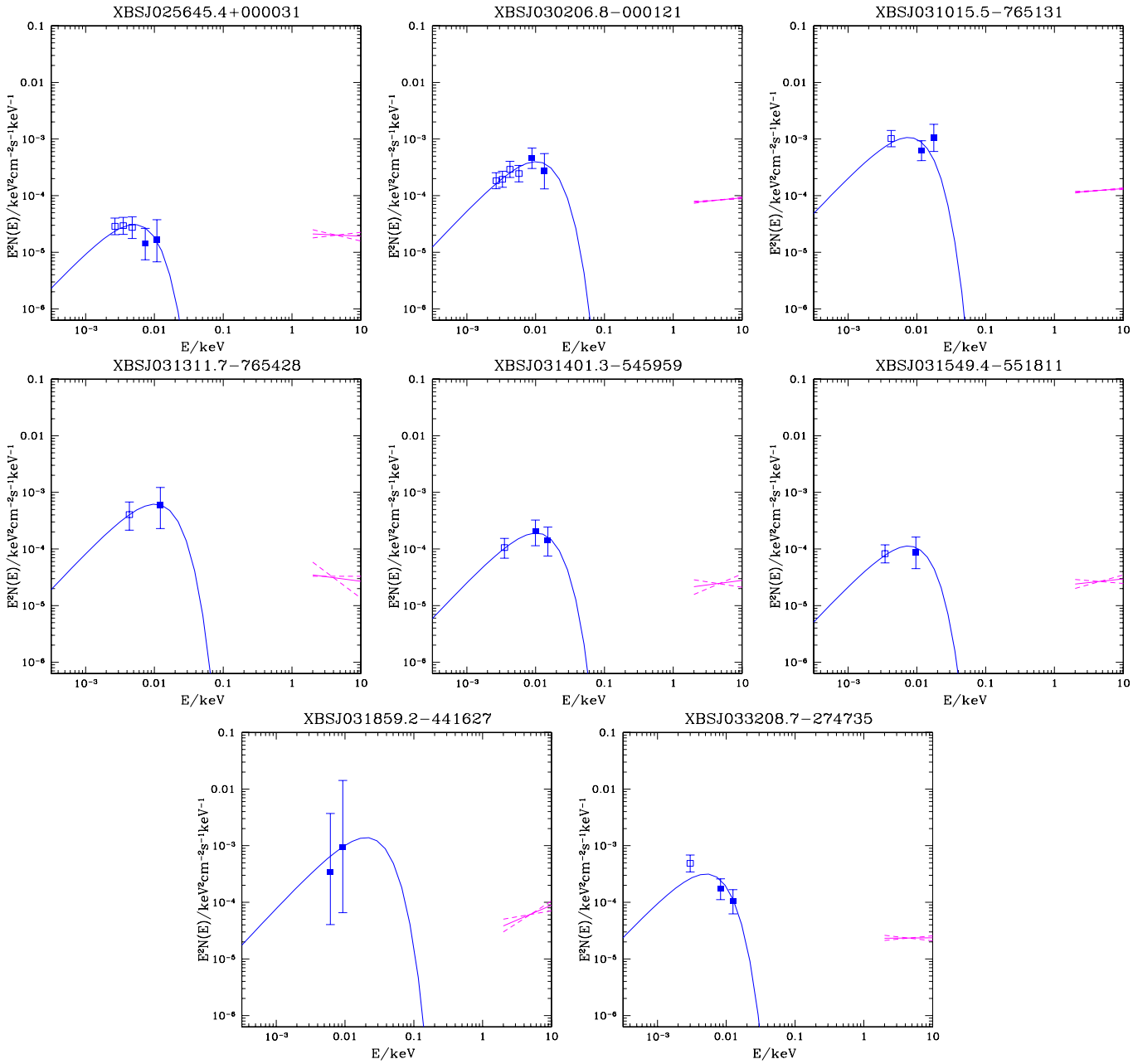
XBSJ025645.4+000031
XBSJ030206.8−000121
XBSJ031015.5−765131
XBSJ031311.7−765428
XBSJ031401.3−545959
XBSJ031549.4−551811
XBSJ031859.2−441627
XBSJ033208.7−274735
E²N(E)/keV²cm⁻²s⁻¹keV⁻¹
E/keV

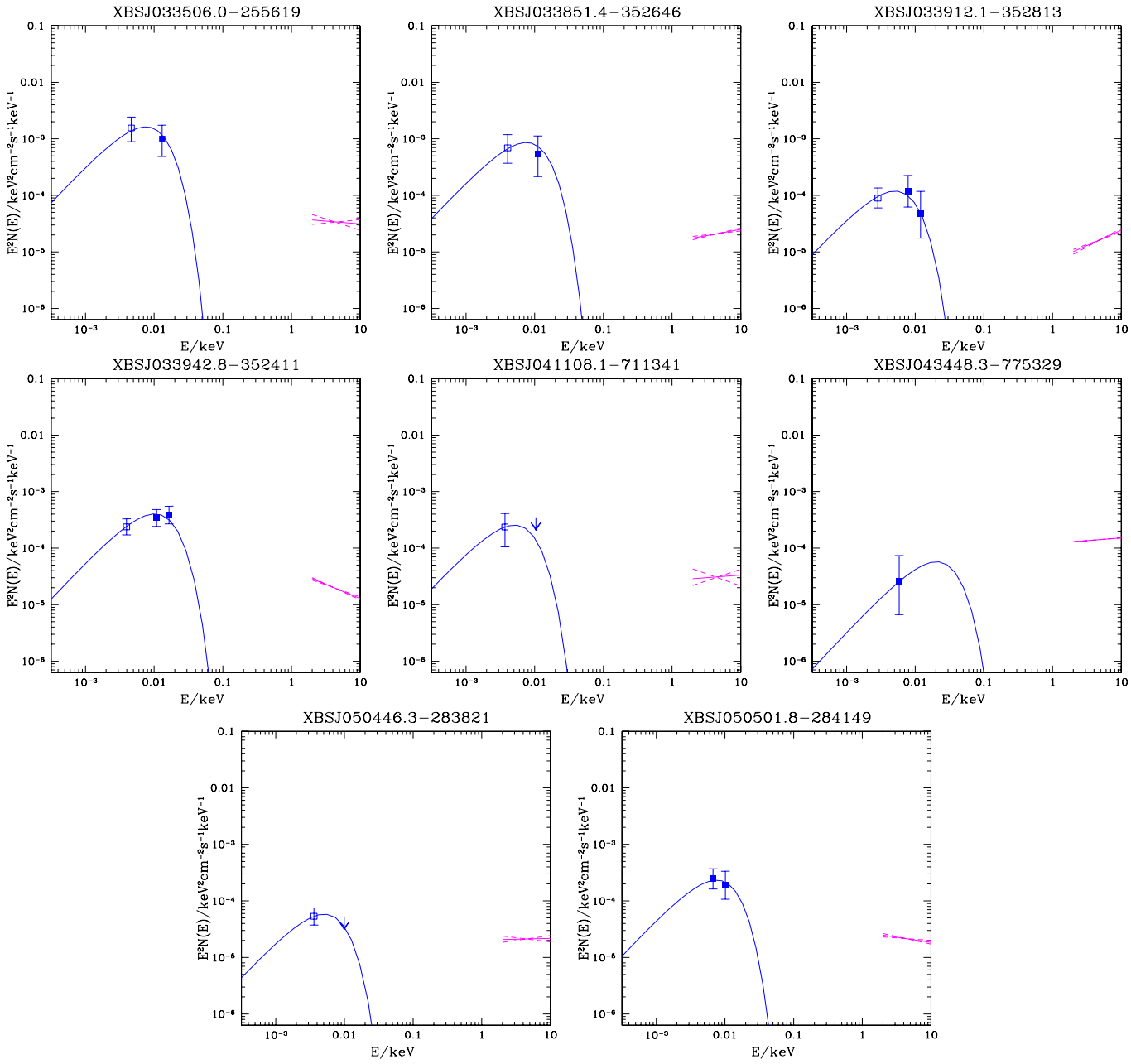
XBSJ033506.0−255619
XBSJ033851.4−352646
XBSJ033912.1−352813
XBSJ033942.8−352411
XBSJ041108.1−711341
XBSJ043448.3−775329
XBSJ050446.3−283821
XBSJ050501.8−284149
E²N(E)/keV²cm⁻²s⁻¹keV⁻¹
E/keV

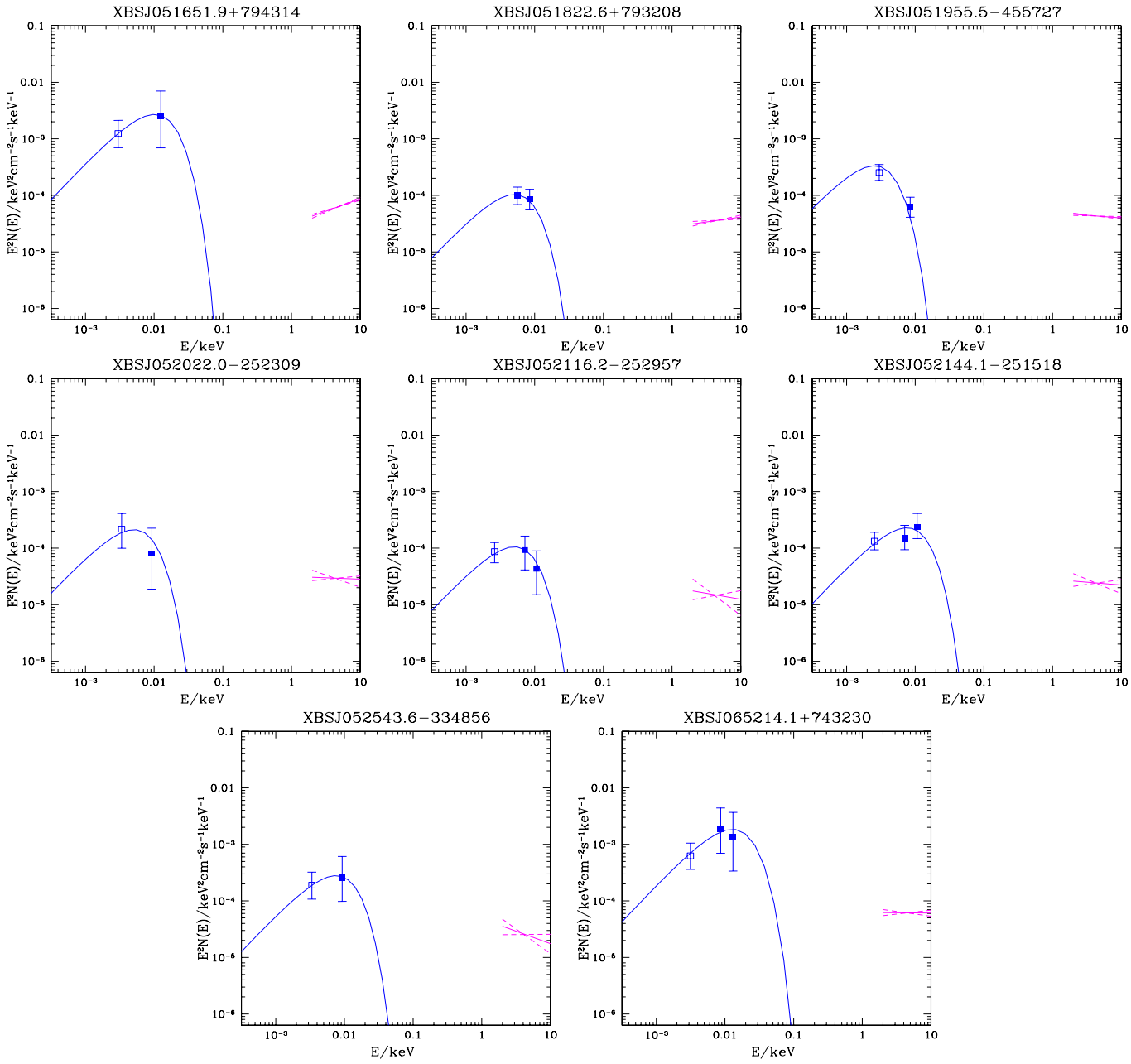
XBSJ051651.9+794314
XBSJ051822.6+793208
XBSJ051955.5−455727
XBSJ052022.0−252309
XBSJ052116.2−252957
XBSJ052144.1−251518
XBSJ052543.6−334856
XBSJ065214.1+743230
E²N(E)/keV²cm⁻²s⁻¹keV⁻¹
E/keV

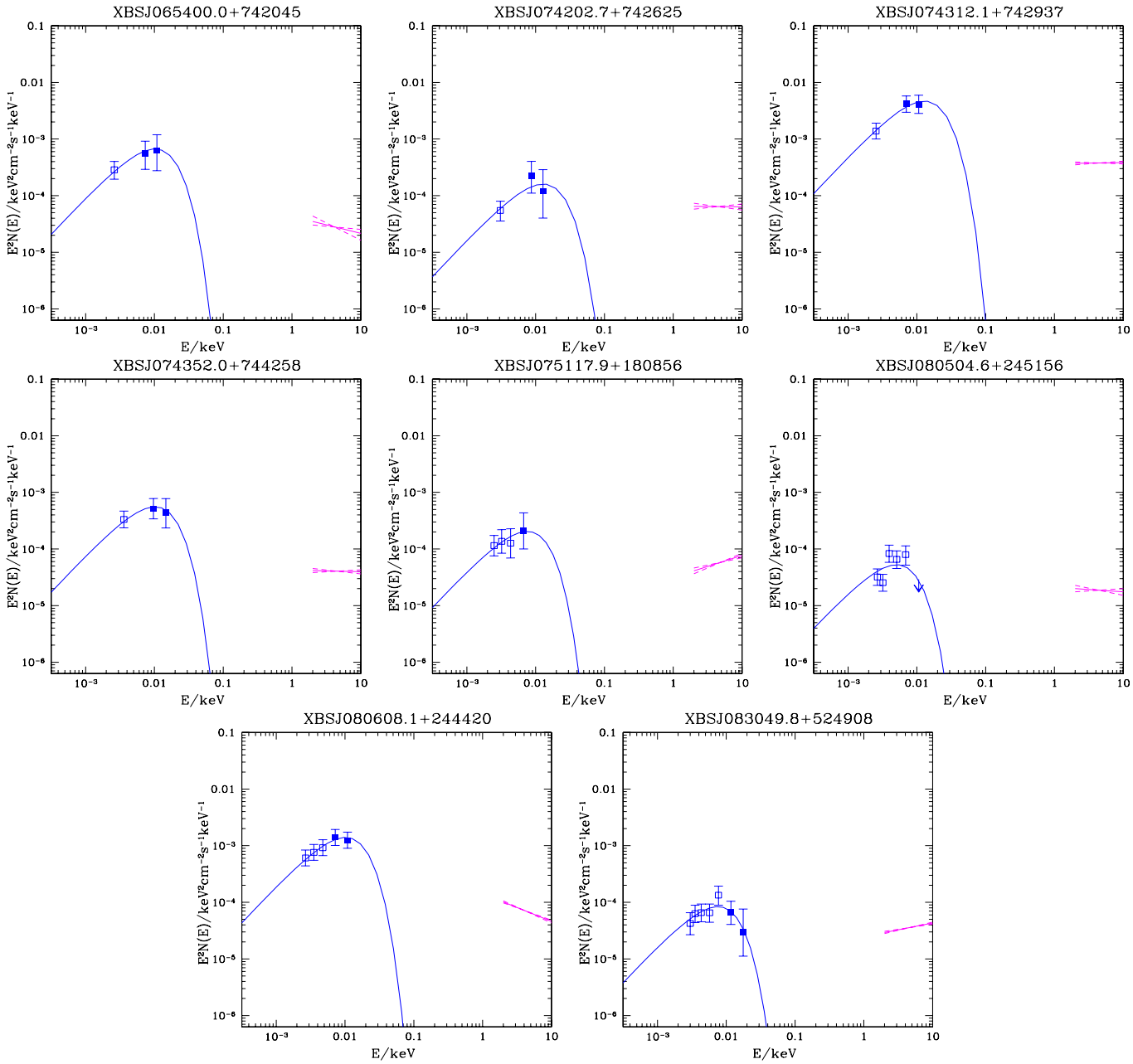
XBSJ065400.0+742045
XBSJ074202.7+742625
XBSJ074312.1+742937
XBSJ074352.0+744258
XBSJ075117.9+180856
XBSJ080504.6+245156
XBSJ080608.1+244420
XBSJ083049.8+524908
E²N(E)/keV²cm⁻²s⁻¹keV⁻¹
E/keV

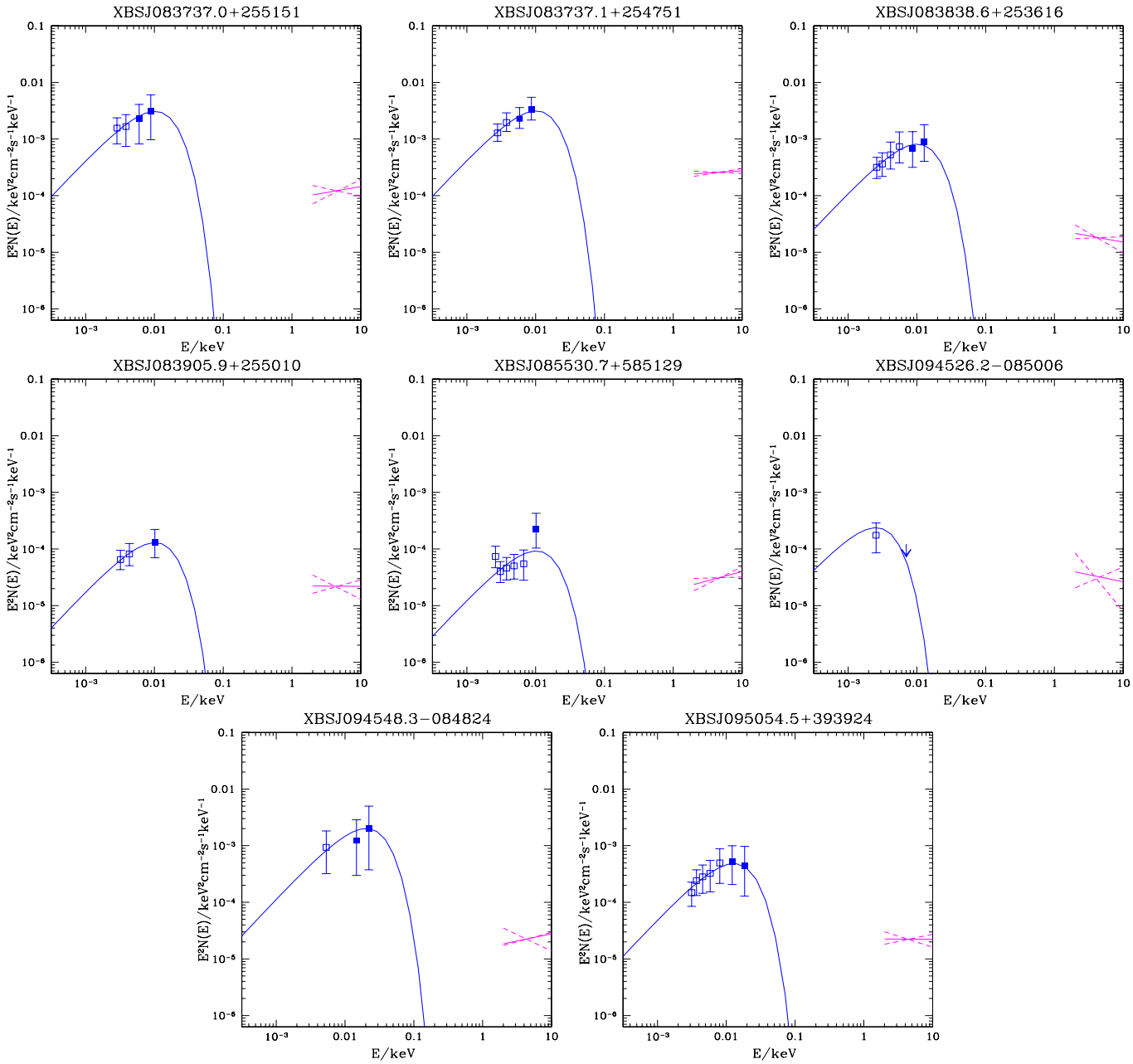
XBSJ083737.0+255151
XBSJ083737.1+254751
XBSJ083838.6+253616
XBSJ083905.9+255010
XBSJ085530.7+585129
XBSJ094526.2−085006
XBSJ094548.3−084824
XBSJ095054.5+393924
E²N(E)/keV²cm⁻²s⁻¹keV⁻¹
E/keV

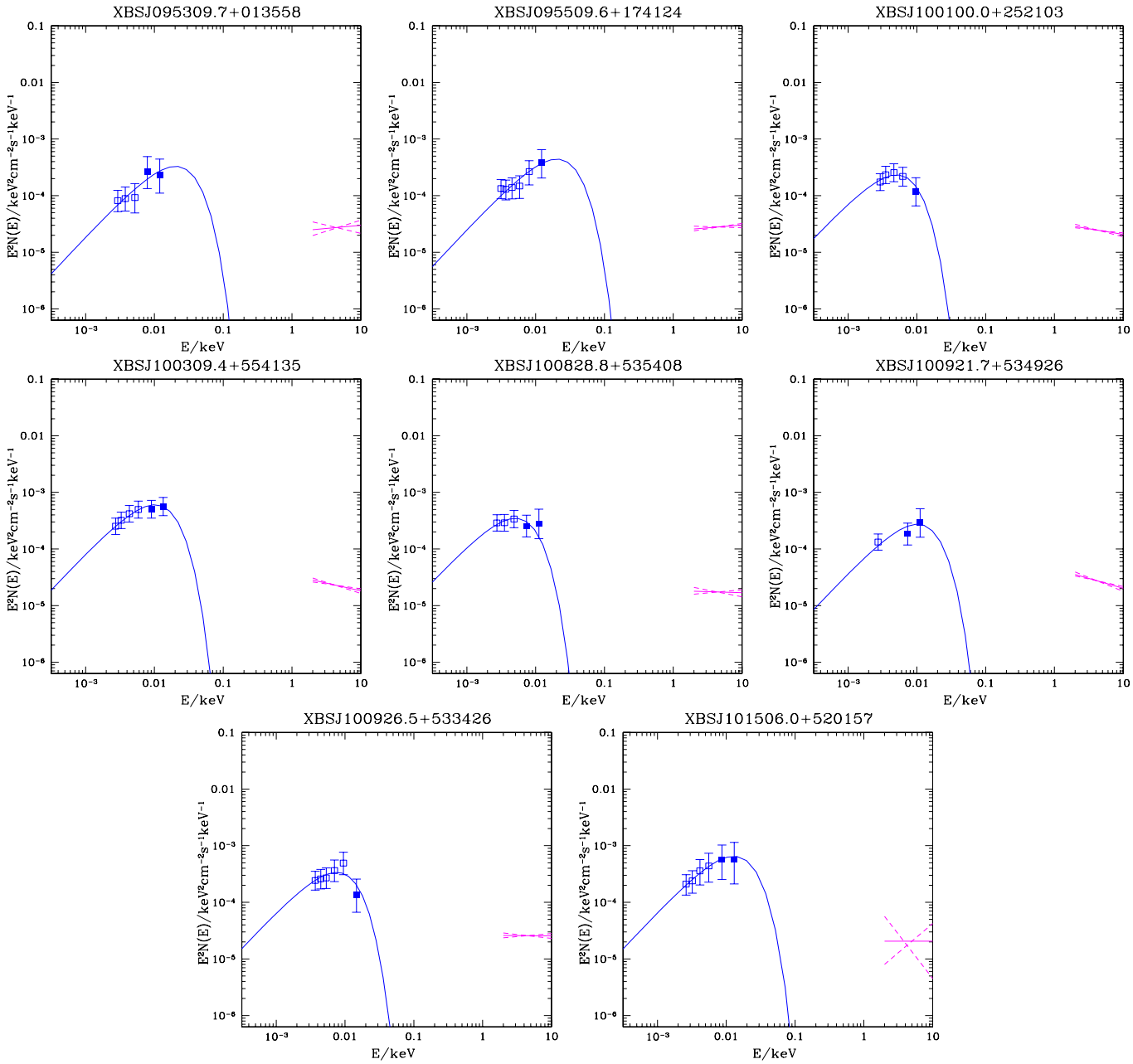
XBSJ095309.7+013558
XBSJ095509.6+174124
XBSJ100100.0+252103
XBSJ100309.4+554135
XBSJ100828.8+535408
XBSJ100921.7+534926
XBSJ100926.5+533426
XBSJ101506.0+520157
E²N(E)/keV²cm⁻²s⁻¹keV⁻¹
E/keV

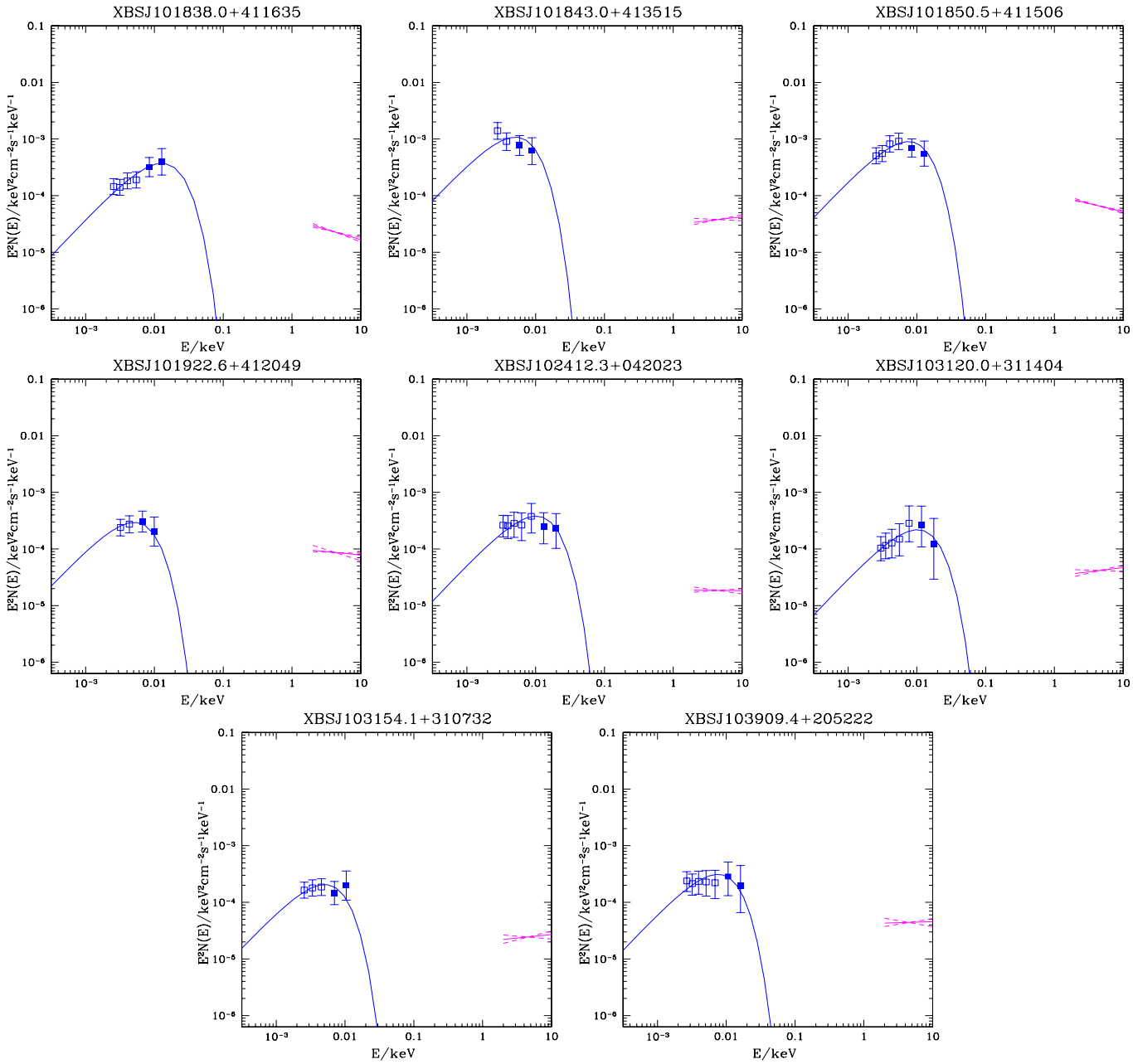
XBSJ101838.0+411635
XBSJ101843.0+413515
XBSJ101850.5+411506
XBSJ101922.6+412049
XBSJ102412.3+042023
XBSJ103120.0+311404
XBSJ103154.1+310732
XBSJ103909.4+205222
E²N(E)/keV²cm⁻²s⁻¹keV⁻¹
E/keV

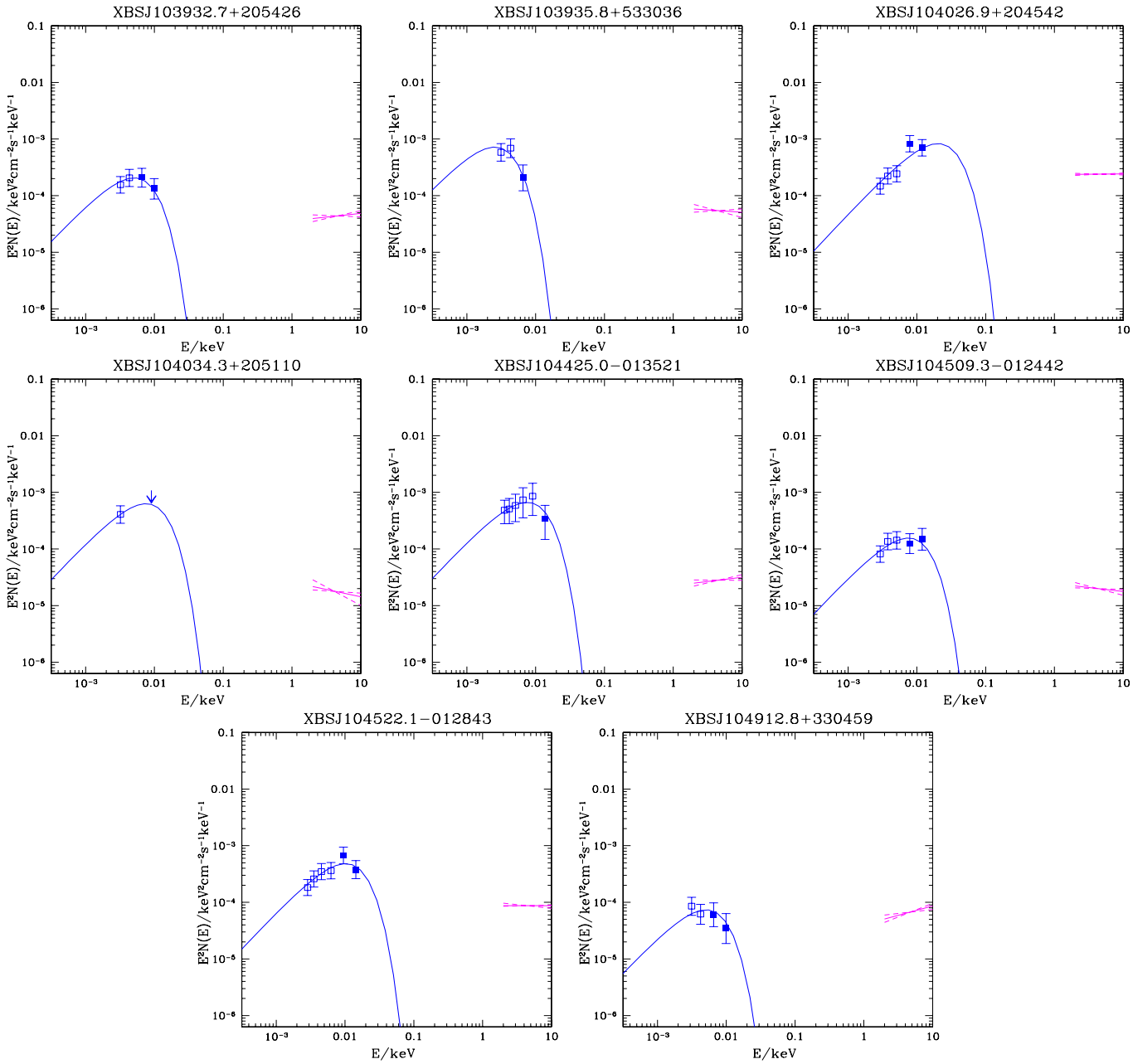
XBSJ103932.7+205426
XBSJ103935.8+533036
XBSJ104026.9+204542
XBSJ104034.3+205110
XBSJ104425.0−013521
XBSJ104509.3−012442
XBSJ104522.1−012843
XBSJ104912.8+330459
E²N(E)/keV²cm⁻²s⁻¹keV⁻¹
E/keV

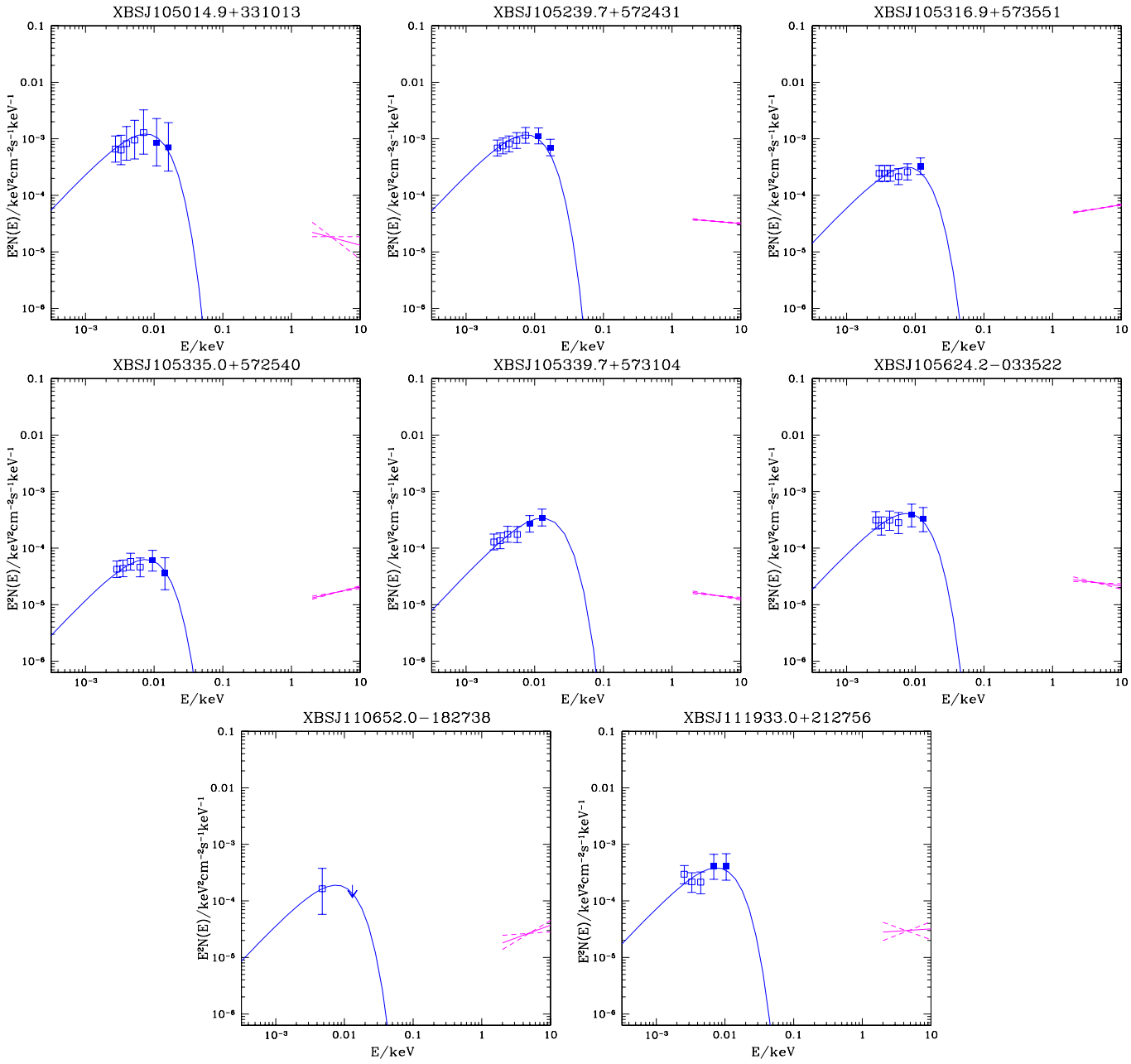
XBSJ105014.9+331013
XBSJ105239.7+572431
XBSJ105316.9+573551
XBSJ105335.0+572540
XBSJ105339.7+573104
XBSJ105624.2−033522
XBSJ110652.0−182738
XBSJ111933.0+212756
E²N(E)/keV²cm⁻²s⁻¹keV⁻¹
E/keV

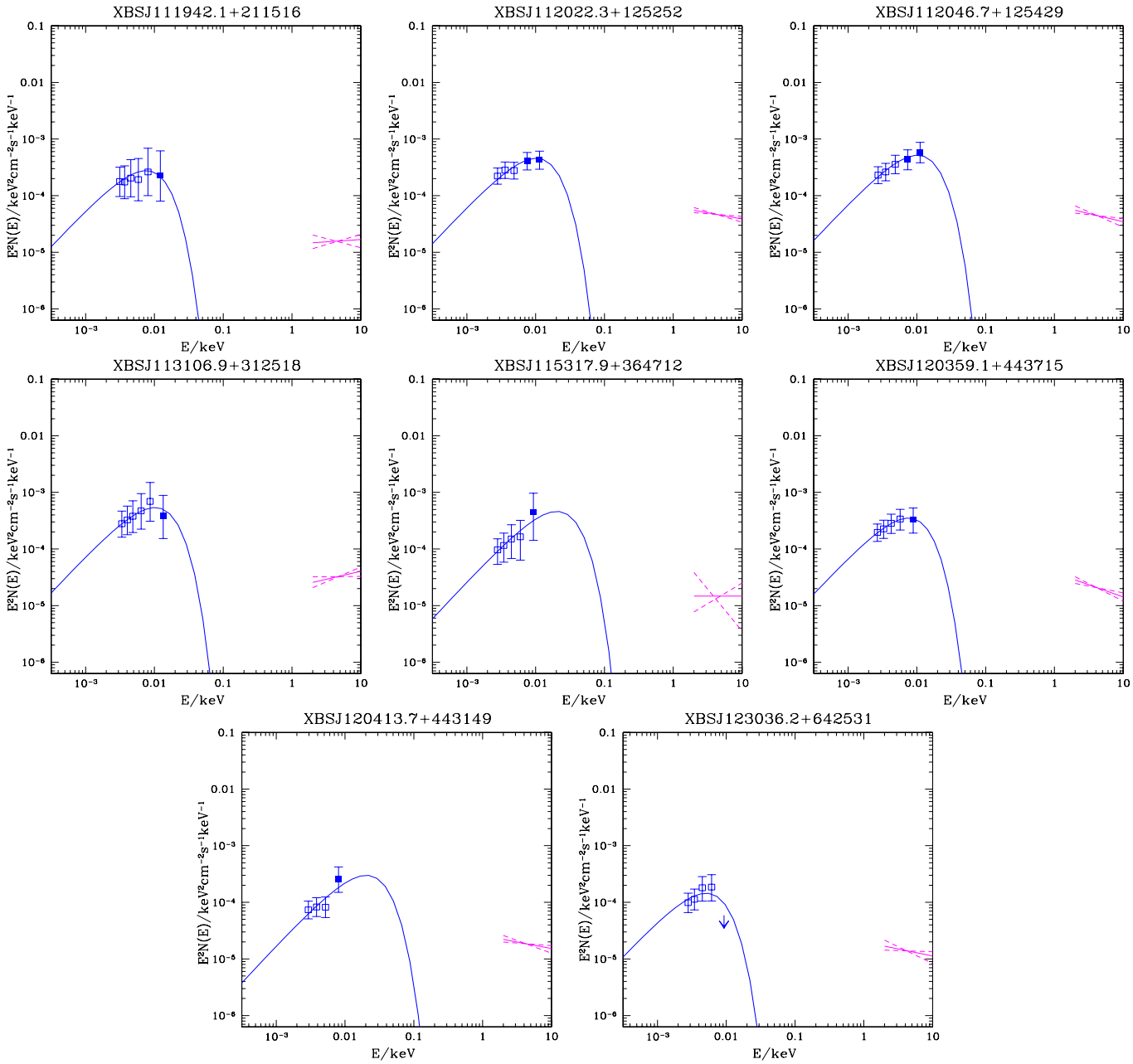
XBSJ111942.1+211516
XBSJ112022.3+125252
XBSJ112046.7+125429
XBSJ113106.9+312518
XBSJ115317.9+364712
XBSJ120359.1+443715
XBSJ120413.7+443149
XBSJ123036.2+642531
E²N(E)/keV²cm⁻²s⁻¹keV⁻¹
E/keV

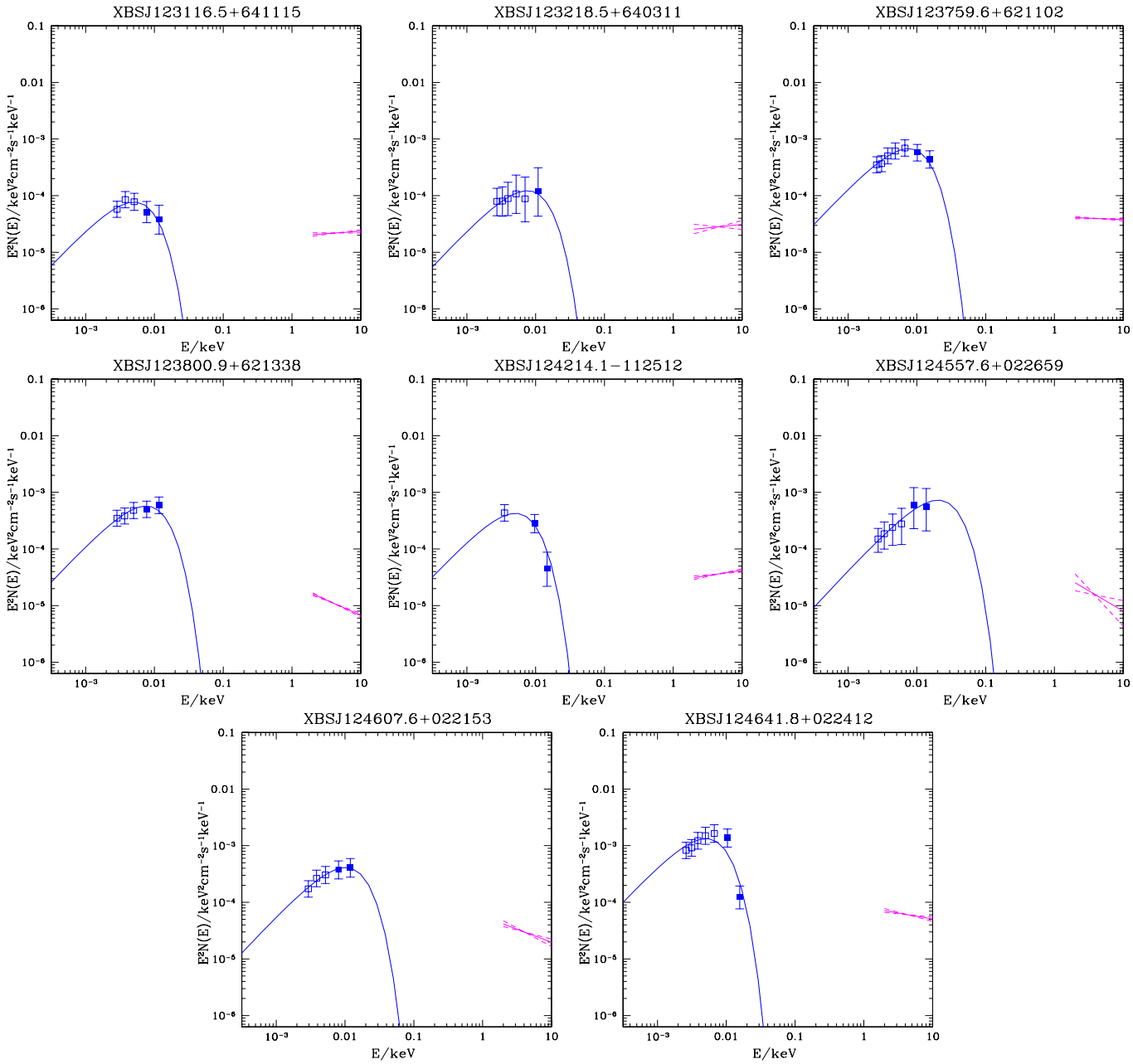
XBSJ123116.5+641115
XBSJ123218.5+640311
XBSJ123759.6+621102
XBSJ123800.9+621338
XBSJ124214.1−112512
XBSJ124557.6+022659
XBSJ124607.6+022153
XBSJ124641.8+022412
E²N(E)/keV²cm⁻²s⁻¹keV⁻¹
E/keV

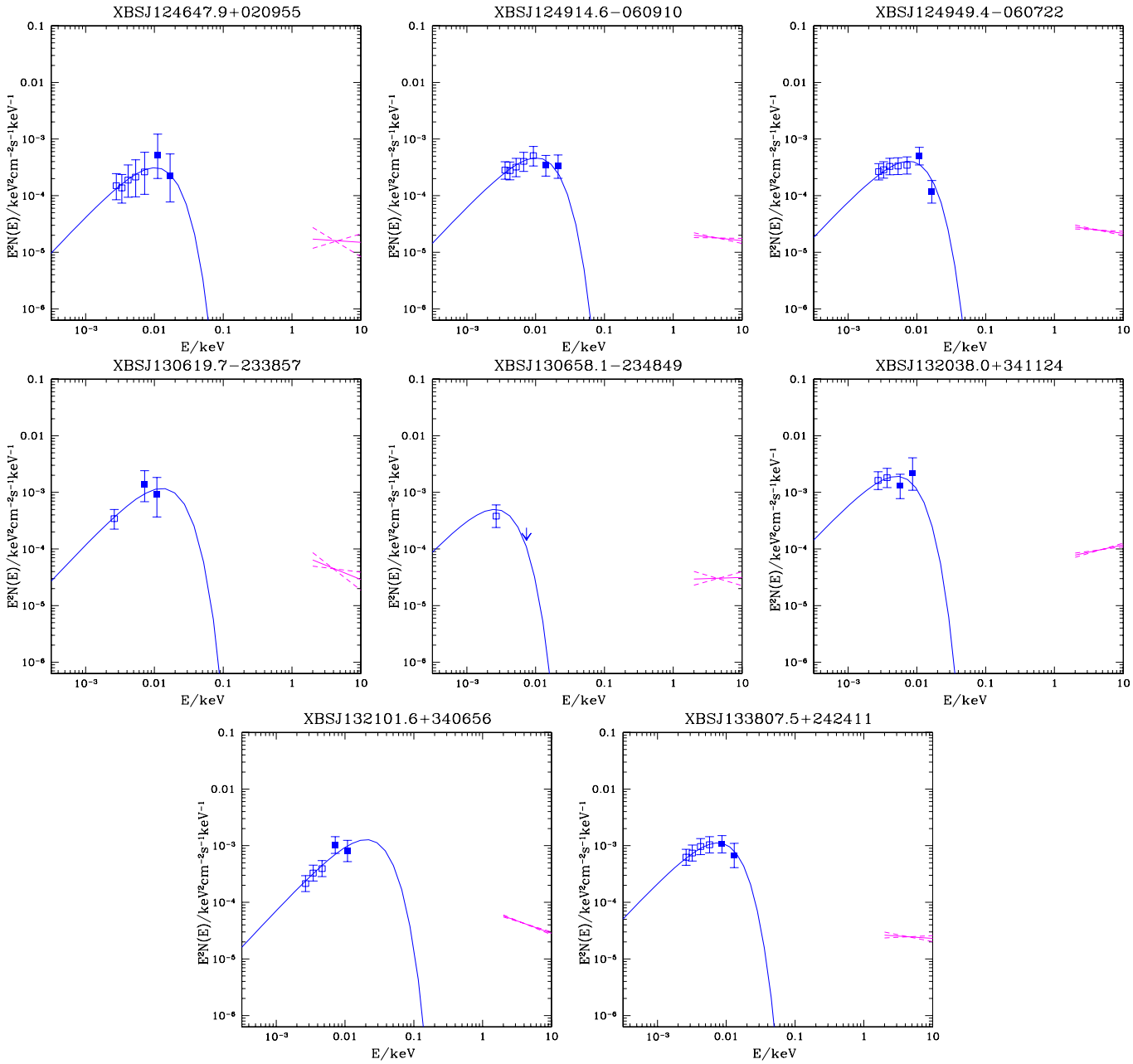
XBSJ124647.9+020955
XBSJ124914.6−060910
XBSJ124949.4−060722
XBSJ130619.7−233857
XBSJ130658.1−234849
XBSJ132038.0+341124
XBSJ132101.6+340656
XBSJ133807.5+242411
E²N(E)/keV²cm⁻²s⁻¹keV⁻¹
E/keV

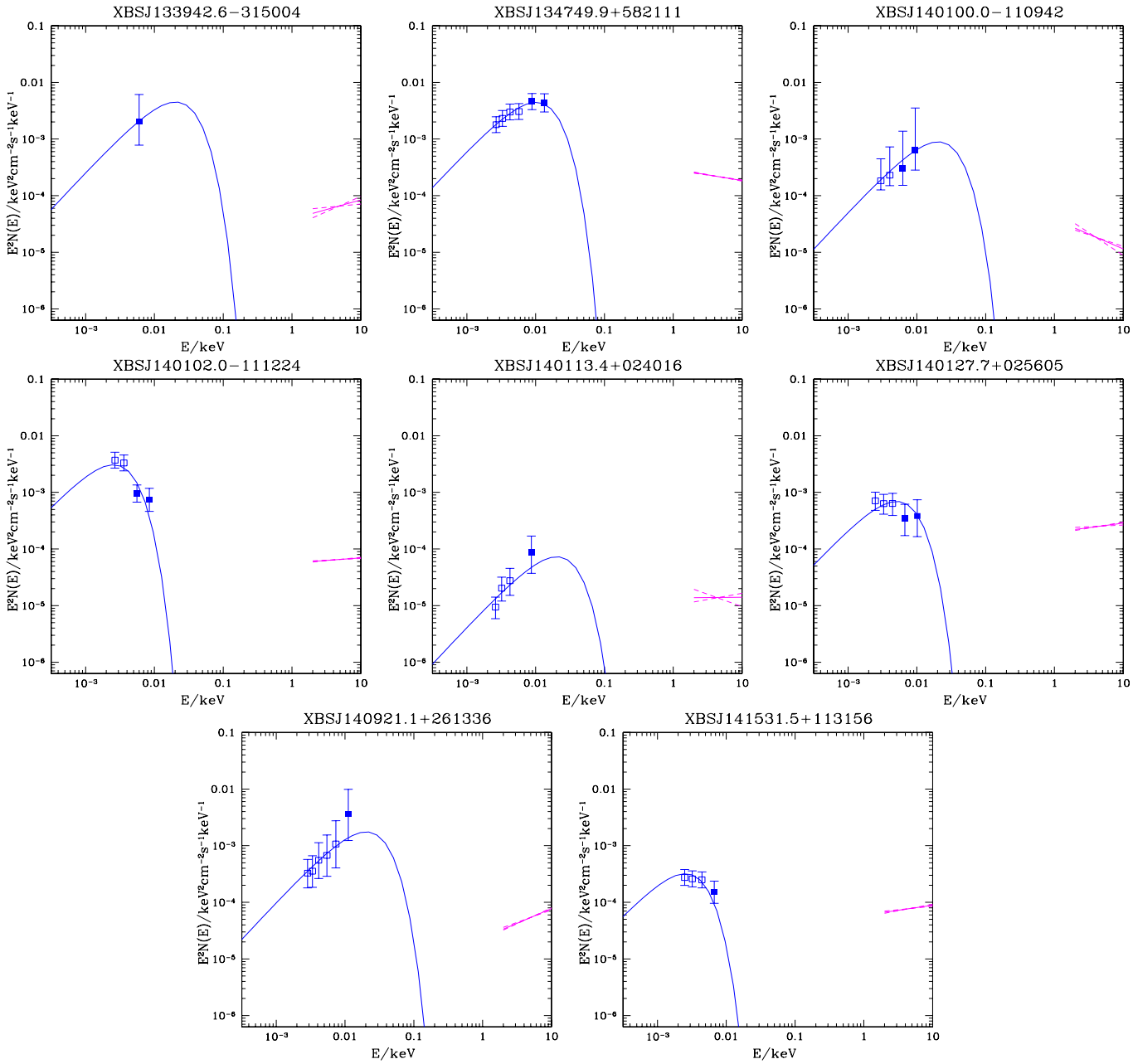
XBSJ133942.6−315004
XBSJ134749.9+582111
XBSJ140100.0−110942
XBSJ140102.0−111224
XBSJ140113.4+024016
XBSJ140127.7+025605
XBSJ140921.1+261336
XBSJ141531.5+113156
E²N(E)/keV²cm⁻²s⁻¹keV⁻¹
E/keV

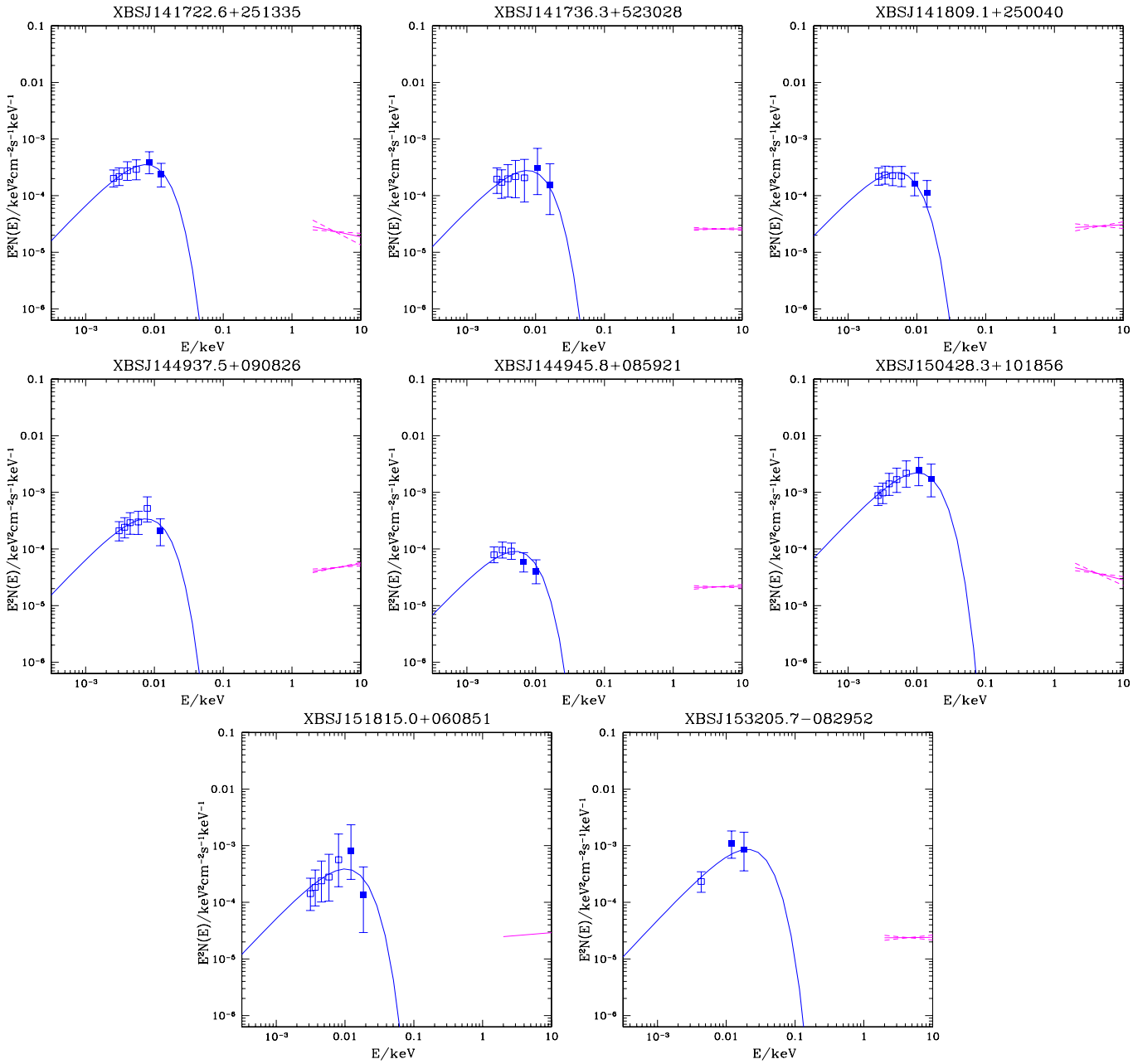
XBSJ141722.6+251335
XBSJ141736.3+523028
XBSJ141809.1+250040
XBSJ144937.5+090826
XBSJ144945.8+085921
XBSJ150428.3+101856
XBSJ151815.0+060851
XBSJ153205.7−082952
E²N(E)/keV²cm⁻²s⁻¹keV⁻¹
E/keV

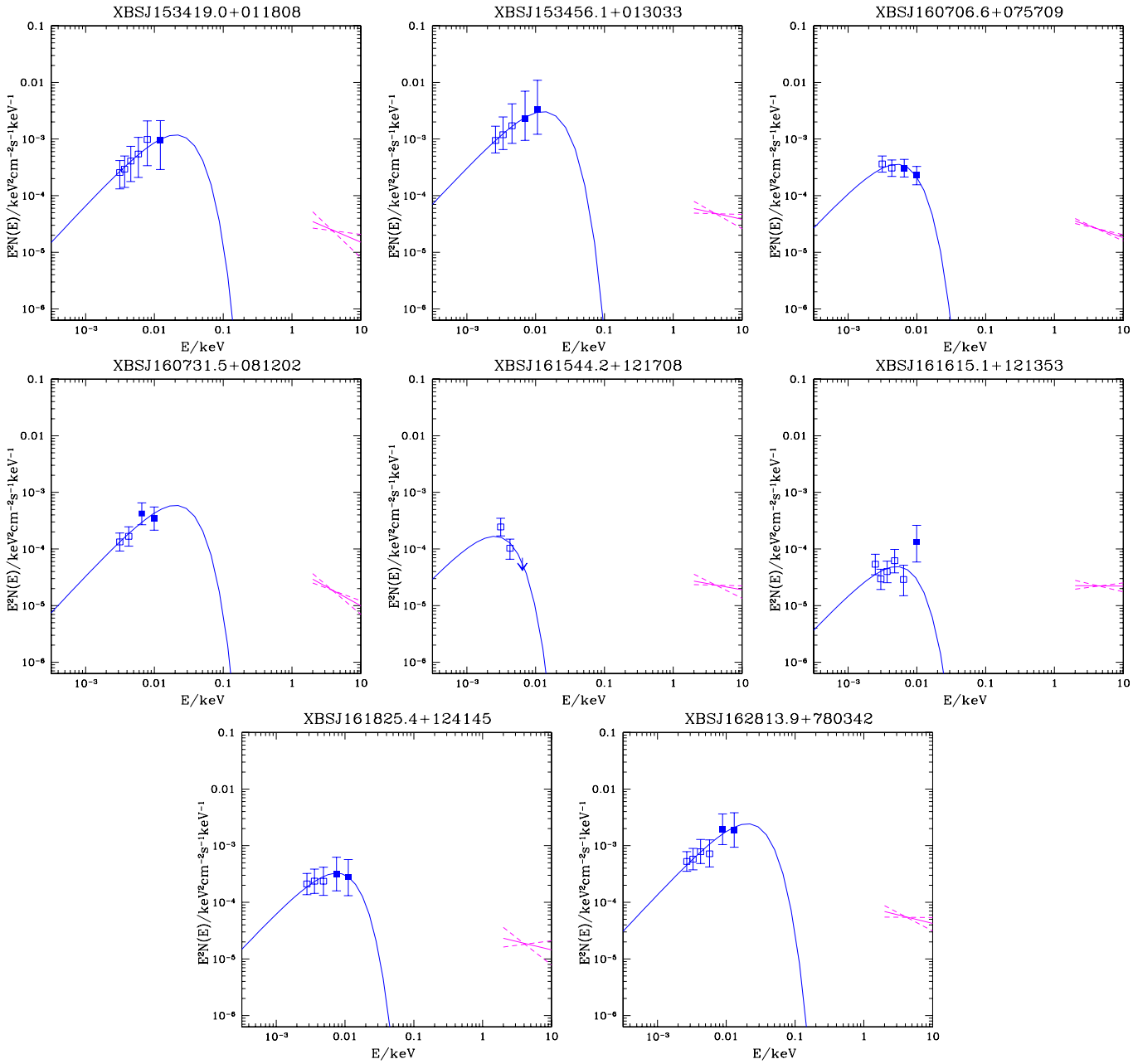
XBSJ153419.0+011808
XBSJ153456.1+013033
XBSJ160706.6+075709
XBSJ160731.5+081202
XBSJ161544.2+121708
XBSJ161615.1+121353
XBSJ161825.4+124145
XBSJ162813.9+780342
E²N(E)/keV²cm⁻²s⁻¹keV⁻¹
E/keV

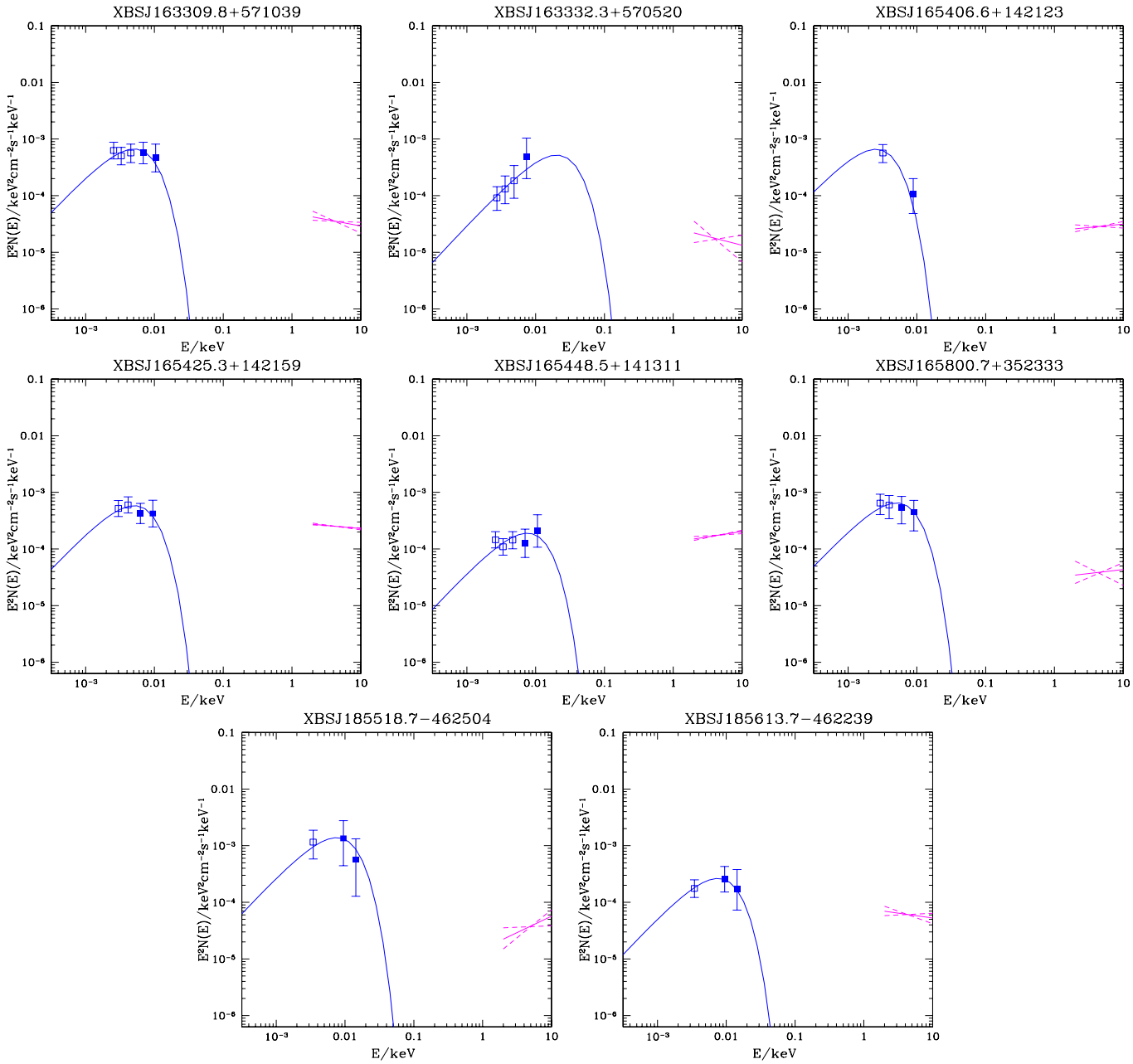
XBSJ163309.8+571039
XBSJ163332.3+570520
XBSJ165406.6+142123
XBSJ165425.3+142159
XBSJ165448.5+141311
XBSJ165800.7+352333
XBSJ185518.7−462504
XBSJ185613.7−462239
E²N(E)/keV²cm⁻²s⁻¹keV⁻¹
E/keV

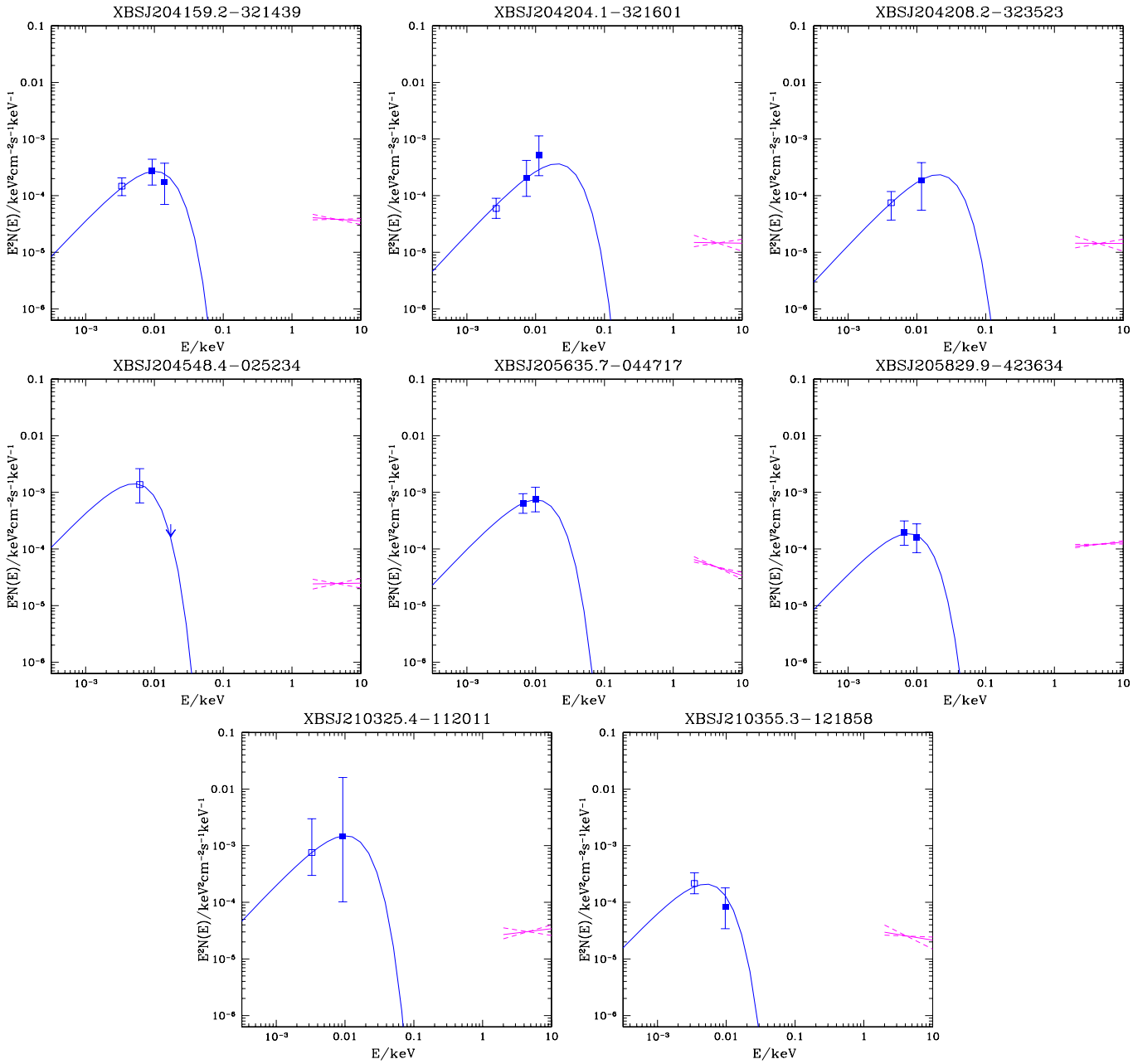
XBSJ204159.2−321439
XBSJ204204.1−321601
XBSJ204208.2−323523
XBSJ204548.4−025234
XBSJ205635.7−044717
XBSJ205829.9−423634
XBSJ210325.4−112011
XBSJ210355.3−121858
E²N(E)/keV²cm⁻²s⁻¹keV⁻¹
E/keV

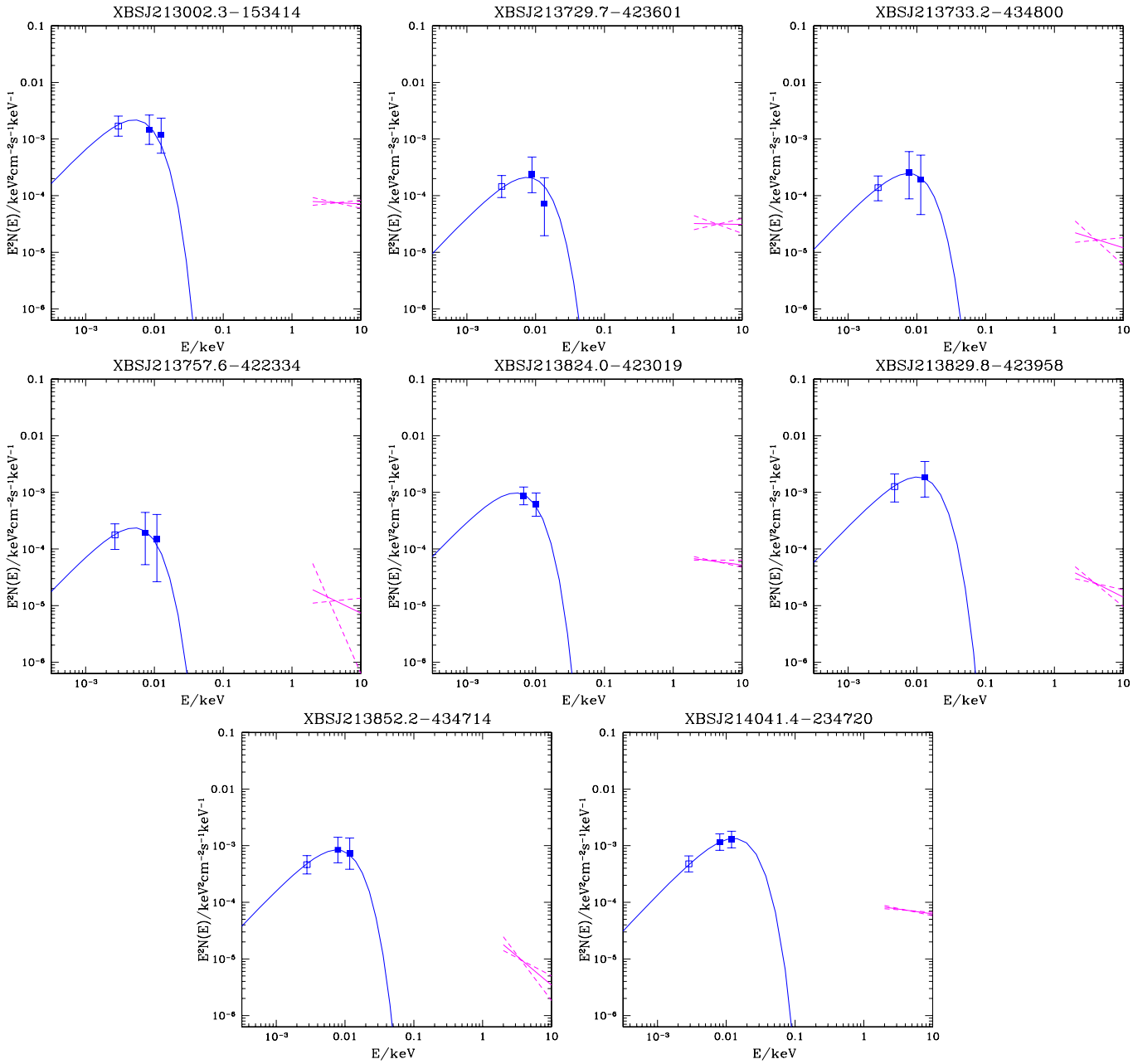
XBSJ213002.3−153414
XBSJ213729.7−423601
XBSJ213733.2−434800
XBSJ213757.6−422334
XBSJ213824.0−423019
XBSJ213829.8−423958
XBSJ213852.2−434714
XBSJ214041.4−234720
E²N(E)/keV²cm⁻²s⁻¹keV⁻¹
E/keV

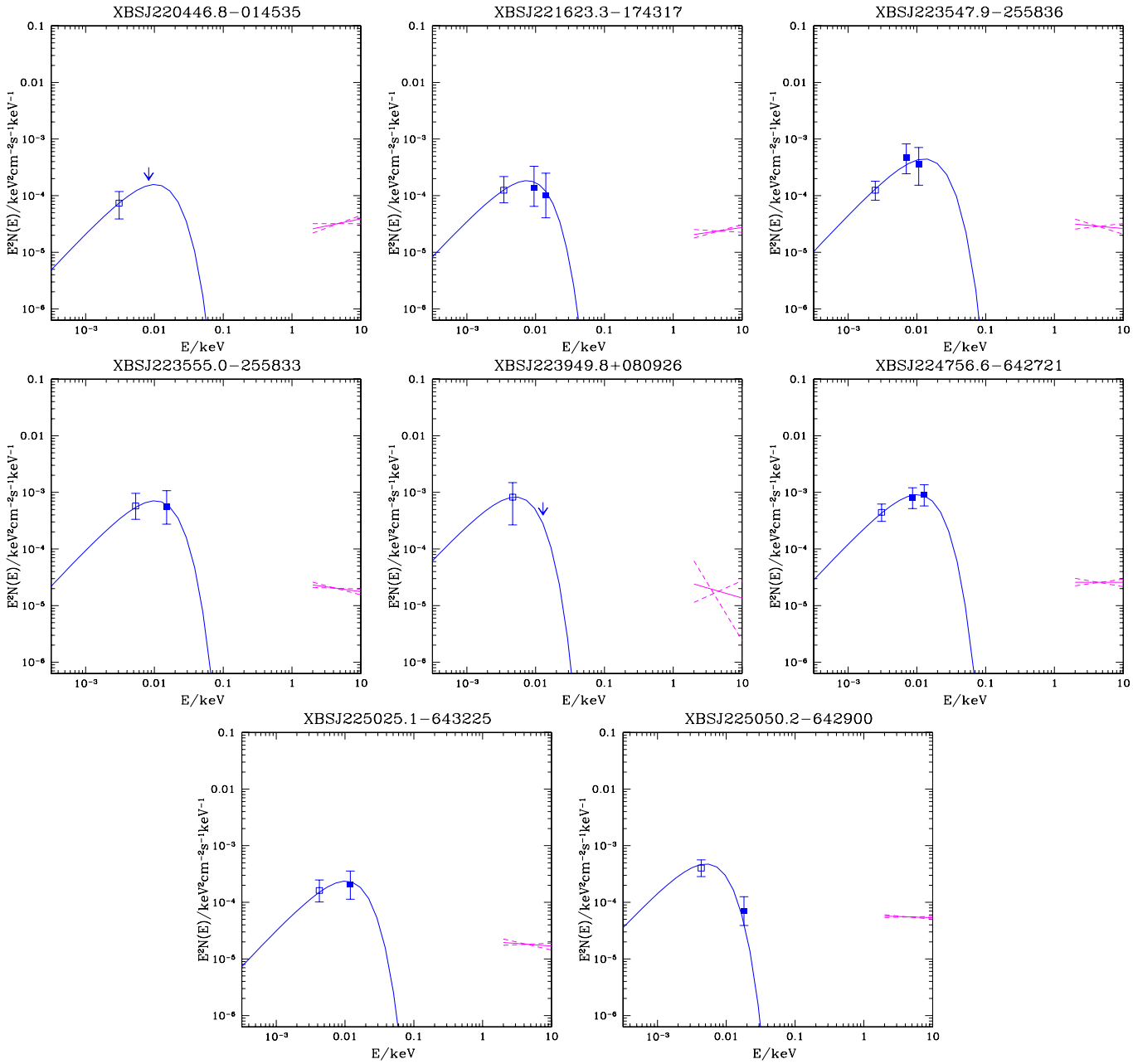
XBSJ220446.8−014535
XBSJ221623.3−174317
XBSJ223547.9−255836
XBSJ223555.0−255833
XBSJ223949.8+080926
XBSJ224756.6−642721
XBSJ225025.1−643225
XBSJ225050.2−642900
E²N(E)/keV²cm⁻²s⁻¹keV⁻¹
E/keV

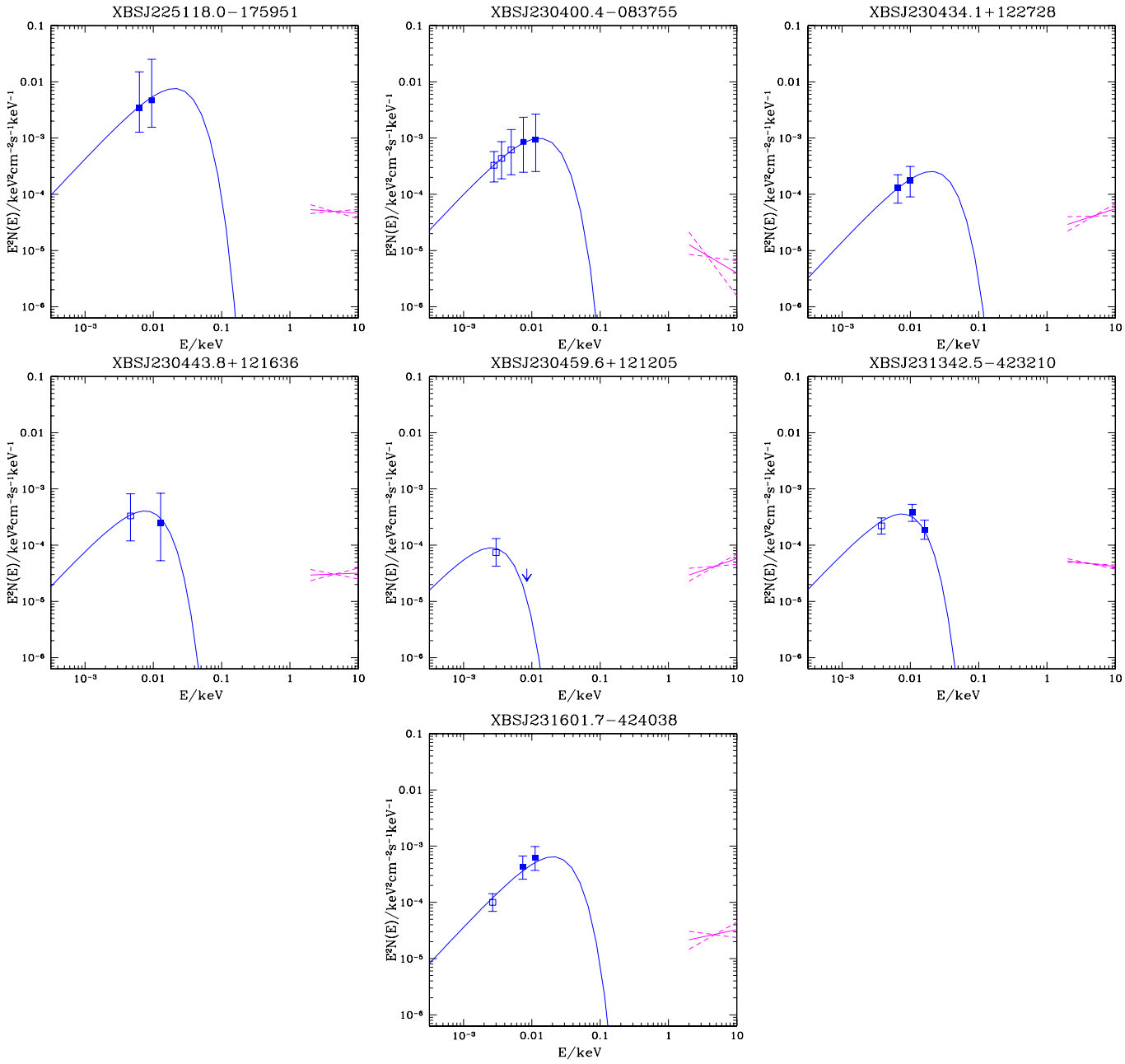
XBSJ225118.0−175951
XBSJ230400.4−083755
XBSJ230434.1+122728
XBSJ230443.8+121636
XBSJ230459.6+121205
XBSJ231342.5−423210
XBSJ231601.7−424038
E²N(E)/keV²cm⁻²s⁻¹keV⁻¹
E/keV